

**NANOPARTICLE CONTRAST AGENTS
FOR OPTICAL COHERENCE TOMOGRAPHY**

by

Michelle Lynn Gabriele

Bachelor of Science in Biomedical Engineering, University of Rochester, 2004

Submitted to the Graduate Faculty of
Swanson School of Engineering in partial fulfillment
of the requirements for the degree of
Doctor of Philosophy in Bioengineering

University of Pittsburgh

2010

UNIVERSITY OF PITTSBURGH
SWANSON SCHOOL OF ENGINEERING

This dissertation was presented

by

Michelle Lynn Gabriele

It was defended on

November 10, 2010

and approved by

Gadi Wollstein, MD, Associate Professor, Department of Ophthalmology

Hiroshi Ishikawa, MD, Assistant Professor, Departments of Ophthalmology and Engineering

Kyle C. McKenna, PhD, Assistant Professor, Department of Ophthalmology

George Stetten, MD, PhD, Professor, Department of Bioengineering

Dissertation Director: Joel S. Schuman, MD, Eye and Ear Foundation Professor and
Chairman of Ophthalmology, Departments of Ophthalmology and Bioengineering

Copyright © by Michelle Lynn Gabriele

2010

NANOPARTICLE CONTRAST AGENTS FOR OPTICAL COHERENCE TOMOGRAPHY

Michelle Lynn Gabriele, PhD

University of Pittsburgh, 2010

Optical coherence tomography (OCT) provides real-time, objective, *in-vivo*, optical cross-sectional representations of the retina and optic nerve. Recent innovations in image acquisition, including the incorporation of Fourier/spectral-domain detection, have improved imaging speed, sensitivity and resolution. Still, there remain specific structures within ocular OCT images, such as retinal ganglion cells (RGCs), which are of clinical interest but consistently have low contrast. This makes it difficult to differentiate between surrounding layers and structures.

The objectives of this project were: 1. To establish a reliable method for OCT imaging of the healthy and diseased mouse eye in order to provide a platform for testing the utility of OCT contrast agents for ocular imaging, 2. To develop antibody-conjugated gold nanoparticles suitable for targeting specific structures and enhancing OCT image contrast in the mouse eye, and 3. To examine the localized contrast-enhancing ability and biocompatibility of gold nanoparticle contrast agents *in-vivo*. Our organizing hypotheses were that nanoparticles could improve contrast by modulating the intensity of backscattered light detected by OCT and that they could be directed to ocular structures of interest using antibodies specific to cellular markers.

A reproducible method for imaging the mouse retina and quantifying retinal thickness was developed and this technique was then applied to a mouse model for retinal ganglion cell loss, optic nerve crush. Gold nanorods were designed specifically to augment the backscattering OCT signal at the same wavelengths of light used in current ophthalmic OCT imaging schemes

(resonant wavelength $\lambda = 840$ nm). Anti-CD90.1 (Thy1.1) antibodies were conjugated to the gold nanorods and a protocol for characterization of the success of antibody conjugation was developed. Upon injection, the gold nanorods were found to remain in the vitreous post-injection, with many consumed by an early inflammatory response and only very few reaching the internal limiting membrane and passing into the retina. Our findings suggest that, while gold nanorods are able to locally increase OCT signal intensity in the vitreous, their utility in the retina may be limited.

TABLE OF CONTENTS

LIST OF TABLES	IX
LIST OF FIGURES	X
PREFACE.....	XIV
ABBREVIATIONS.....	XVI
1.0 INTRODUCTION.....	1
1.1 OPTICAL COHERENCE TOMOGRAPHY.....	2
1.2 GLAUCOMA IMAGING WITH OCT	6
1.3 NANOPARTICLES.....	8
1.4 GOLD NANORODS AS OPTICAL IMAGING CONTRAST AGENTS.....	10
1.5 PROJECT OBJECTIVES.....	13
1.5.1 Objective 1	14
1.5.2 Objective 2	14
1.5.3 Objective 3	14
2.0 MOUSE IMAGING WITH OPTICAL COHERENCE TOMOGRAPHY... 	15
2.1 REPRODUCIBILITY OF MEASUREMENTS IN HEALTHY MICE	15
2.1.1 Methodology	16
2.1.2 Statistical Analysis	21
2.1.3 Results	22
2.1.4 Summary and Discussion	24

2.2	QUANTIFYING RETINAL THICKNESS CHANGES AFTER INJURY...	27
2.2.1	Methodology	28
2.2.2	Statistical Analysis	31
2.2.3	Results	31
2.2.4	Summary and Discussion	34
2.3	SUMMARY AND DISCUSSION: MOUSE IMAGING WITH OCT	37
3.0	GOLD NANOROD PREPARATION.....	38
3.1	PREPARATION OF GOLD NANORODS	38
3.1.1	Seed-mediated, Surfactant Directed Synthesis.....	39
3.2	CHARACTERIZATION OF GOLD NANORODS	42
3.2.1	Methods.....	44
3.2.2	Results	47
3.2.3	Discussion.....	50
3.3	SUMMARY AND DISCUSSION: GOLD NANORODS	51
4.0	PRE-CLINICAL STUDIES	52
4.1	GOLD NANOROD INJECTIONS.....	52
4.1.1	Animals and Methodology.....	52
4.1.2	Results	54
4.1.3	Injection Summary and Discussion	59
4.2	BIOCOMPATIBILITY EXPERIMENTS.....	60
4.2.1	Methodology	62
4.2.2	Results	65
4.2.3	Summary and Discussion	71
4.3	SUMMARY AND DISCUSSION: PRE-CLINICAL EXPERIMENTS	73
5.0	DISSERTATION SYNOPSIS.....	74

5.1	LIMITATIONS	75
5.2	FUTURE WORK	78
5.3	CONCLUSIONS	80
	APPENDIX A	81
	APPENDIX B	84
	BIBLIOGRAPHY	86

LIST OF TABLES

Table 1. Estimates of mixed effect model parameters and coefficient of variation (CV) for global and sectoral total retinal thickness. All estimates are in microns (μm) except for CV, which is unitless.....	24
Table 2. Experimental groups.....	63
Table 3. Fluorescent antibodies used for flow cytometric staining	65
Table 4. Expected cell counts and 95% confidence intervals from generalized estimation equation models of cell counts for (A) CD45+ leukocytes that expressed Thy1.2 (B), or CD11b (C), and CD11b+ cells that expressed F4/80 (D) and GR-1 (E). P-values for pairwise comparison of groups for a given cell type are indicated at right, with statistically significant differences indicated by *	70

LIST OF FIGURES

- Figure 1. Schematic diagram of our spectral-domain OCT system. Light from a broadband superluminescent diode is split, with 80% going to the eye and 20% to a stationary reference mirror. The light recombines and an interference pattern is detected using a spectrometer and charge-coupled device (CCD) camera, and Fourier-transformed to obtain a reflectivity profile. Red arrows indicate the optical path. $\Delta\lambda_{FWHM}$ - full width at half-maximum of the applied light; λ - center wavelength. 4
- Figure 2. Two-dimensional SD-OCT cross-sectional scan (B-scan) through the macula of a human subject. The vertical white line denotes the location of the single A-scan intensity profile shown on the right. This macular cross-section scan consisted of 1000 A-scans, 1024 pixels in depth (6 mm x 2 mm). 5
- Figure 3. SD-OCT fundus image of the optic nerve head region of a human subject (left) created by summing a 3D data cube in depth (6.0 x 6.0 x 2.0 mm; 200 x 200 x 1024 pixels). A single cross-section through the optic nerve, at the level of the red line in the SD-OCT fundus image (right). 6
- Figure 4. Number of PubMed publications using nanoparticles from 1978 (first publication) through 2009 (PubMed search: (nanoparticles) AND "Year"[Publication Date] : "Year"[Publication Date]). 9
- Figure 5. Demonstration of surface plasmon resonance (SPR). An electromagnetic wave interacts with spherical particles and resonance occurs along one axis; when the same wave interacts with nanorod, resonance occurs along the long and short dimensions and causes SPR along the length and width of the particle..... 10
- Figure 6. Theoretical tuning of longitudinal resonance wavelength in GNRs, which is dependent upon GNR aspect ratio. Given the same width, longer rods will have a longer resonant wavelength..... 11
- Figure 7. Side (left) and top (right) views of custom stage used for alignment of the mouse for SD-OCT imaging of the optic nerve head. A cover slip was used to neutralize the power of the mouse cornea (green arrow). *Gabriele ML et al. Reproducibility of SD-OCT TRT Thickness Measurements in Mice. Invest Ophthalmol Vis Sci 2010 Jun 23 [Epub ahead of print]. Copyright held by the Association for Vision in Research and Ophthalmology.* 17
- Figure 8. Manual alignment of two SD-OCT *enface* images. (A) Reference SD-OCT *enface* image and (B) subsequent SD-OCT *enface* image. (C) Subsequent scan registered to reference. *Gabriele ML et al. Reproducibility of SD-OCT TRT Thickness*

- Figure 9. SD-OCT *enface* image (left) with the red line indicating the location of the OCT B-scan (right). The B-scan demonstrates automated segmentation of the internal limiting membrane (ILM, white line) and retinal pigment epithelium (RPE, blue line) to obtain total retinal thickness measurements. The vertical gray lines represent the disc margin. 20
- Figure 10. Total retinal thickness maps aligned to a single reference scan. (A, C, F): SD-OCT *enface* images; (B, D, G): Total retinal (TR) thickness map with sampling region indicated as the region between red concentric circles (E, H): Total retinal thickness maps, registered to reference. *Gabriele ML et al. Reproducibility of SD-OCT TRT Thickness Measurements in Mice. Invest Ophthalmol Vis Sci 2010 Jun 23 [Epub ahead of print]. Copyright held by the Association for Vision in Research and Ophthalmology. 23*
- Figure 11. Optic nerve exposed for nerve crush surgery. *Photo courtesy of C. Leung. 29*
- Figure 12. (Top) Individual total retinal thickness (TRT) measurements, each eye represented by a different color and (Bottom) mean global TRT over time for control and nerve-crushed eyes; the solid line represents mean thickness and dashed lines represent the standard deviation..... 33
- Figure 13. (a) Seed-mediated, surfactant directed synthesis preparation of gold nanorods (GNR). (b) Top: Photograph of GNR solution after concentrating and removing excess CTAB; Bottom: electron micrograph of PAA-coated GNRs (c) Absorbance spectrum of PAA-coated GNRs, with resonance peaks at $\lambda = 530\text{nm}$ and $\lambda = 835\text{nm}$ 40
- Figure 14. GNRs were prepared in a solution with a potentially cytotoxic, positively-charged surfactant (CTAB), so a negatively-charged PAA coating is used to neutralize and shield 41
- Figure 15. OCT image of phosphate buffered saline (PBS; sham) and gold nanorod (GNR) solution. Enhanced scattering can be observed in the GNR solution (250 A-scans; 2.5 mm). 41
- Figure 16. Schematic representation of flow cytometer. Incident laser light is scattered upon reaching an individual cell; forward and side scattered light is collected via filters and photodetectors. 43
- Figure 17. Summary of methodology for flow cytometry assay of EL-4 tumor cells (Thy1.2+), using antibody-coated ($\alpha\text{CD90.2}/\alpha\text{Thy1.2}$) GNRs solutions washed up to two times and their corresponding supernatants. The secondary antibody (2°) was APC-conjugated. 46

Figure 18. TEM showing labeling of Ab-GNRs with 2° Ab-conjugated 12 nm gold colloidal spheres. Most Ab-GNRs had a single 2° label, and some free 12 nm colloidal spheres indicate the presence of free antibodies. PSS-GNRs were not labeled.	47
Figure 19. TEM showing a single Ab-GNR labeled with three colloidal gold 2° Ab. Each Ab-GNR is coated with PSS to shield from any CTAB layer leftover from production of the particles.....	48
Figure 20. Results of flow cytometry assay. Top panel: stock Ab-GNRs and supernatant; Middle panel: Ab-GNR solution and supernatant after a single wash; Bottom panel: Ab-GNR solution and supernatant after two washes. The subset gate indicates the percentage APC-positive cells; more densely-packed cell populations are indicated by hotter colors.	49
Figure 21. Baseline and follow-up (1 day after injection) images from mice injected with sham and gold nanorods (GNR). Marked signal enhancement is observed in the GNR injected vitreous as compared to both pre-injection and the sham injection images. The retinal signal is attenuated in the GNR-injected eye due to a shadowing effect caused by the strong backscattering signal from the vitreous. Abbreviations: L – Lens, V – Vitreous, R – Retina, ON – Optic Nerve, HC – Hyaloid Canal.....	56
Figure 22. Baseline and follow-up (up to 30 days after injection) images from mice injected with gold nanorods (GNR).	57
Figure 23. Transmission electron micrograph showing GNR in vitreous and lining the lens capsule after injection.....	57
Figure 24. Transmission electron micrographs showing GNRs in microglia in the retina after injection. RPE – retinal pigment epithelium, PR IS – photoreceptor inner segment, ONL – outer nuclear layer, OPL – outer plexiform layer, INL – inner nuclear layer..	58
Figure 25. TEM images from two mice (top and bottom panels) 24 hours post GNR injection. (Top left) Arrowheads show a line of extracellular particles near inflammatory cells and (Top right) arrows show some free particles as well as some that have been internalized. (Bottom left) Extracellular and intracellular GNRs are evident when looking at magnified section (Bottom right). The rectangles indicate the location of higher magnification images.	67
Figure 26. Flow cytometric analysis of collagenase-digested eyes after indicated treatments to determine the number of infiltrating CD45+ leukocytes (A.) that expressed Thy1.2 (B.), T cells, or CD11b (C.) myeloid cells. CD11b+ cells were further characterized for expression of F4/80 (D.) and GR-1 (E.) to identify F4/80+ GR-1- macrophages and F4/80- GR-1+ neutrophils.	69
Figure 27. Summary of steps taken to optimize GNR longitudinal resonant wavelength. A protocol by Nikoobakht and El-Sayed ¹²² was modified by altering the [AgNO ₃] in the growth solution and adding acid according to the protocol by Prasad. ¹⁶⁷	81

Figure 28. Changing the molar concentration of AgNO_3 that was added to the growth solution only allowed for a maximum longitudinal resonance wavelength of ~ 785 nm. 82

Figure 29. The addition of acid to the growth solution allows for growth of GNRs resonant at ~ 850 nm..... 83

Figure 30. UV-VIS-NIR spectrum of GNRs with longitudinal resonant wavelengths 820-850 nm, with ultrapurified MilliQ water shown for reference. OD – optical density..... 83

PREFACE

When I joined the Glaucoma Imaging Group (GIG) in 2004, I had no idea what to expect from an ophthalmic research lab. But from the moment I started, the GIG has been an extraordinarily fun, talented and productive group of researchers. I could not have found a better place to train or a better team to be on. Dr. Schuman, thank you for the mentoring and support throughout this process. You have been an excellent coach. Dr. Wollstein, I am grateful for your near-daily guidance and for help overcoming the many hurdles associated with designing and carrying out experiments. Dr. Ishikawa, your programming skills never cease to amaze me – can't wait to see what your next 'app' will be. Dr. Bilonick, I am grateful for all of the mixed effects modeling and for your insistence that the only 3D pies out there should be the kind you eat (I second that opinion). A special thank you to the rest of the GIG members, too - past and present, local and abroad. I am excited to see what comes next.

Dr. McKenna, thanks for introducing me to nanotechnology and immunology. None of the in-vitro projects in this dissertation would have been possible without the guidance of the McKenna lab, the Ophthalmology Core Facilities, or the Center for Biological Imaging.

A special thanks to my mother, Kathy, for passing along her creativity, and my father, John, for suggesting engineering so many years ago and for always setting an example of how to succeed. Chris and Nick, you made me tough and pushed me to be my best.

I am grateful for the friends I have made in Pittsburgh, many of whom have joined me on early morning runs or workouts in blizzard-like conditions (or both), and who made running 26.2

miles (4.216×10^{13} nm) bearable. Thanks to Jenny for inspiring me to excel and for always lending an ear, and for co-authoring the best blog out there.

Last but certainly not least, thanks to my new husband Peter for your endless love and support, positive attitude and fantastic meals throughout graduate school. I am looking forward to our future adventures.

ABBREVIATIONS

3D – Three-dimensional

A-scan – Axial scan

Ab – Antibody

ASTM – American Society for Testing and Materials

BSA – Bovine serum albumin

CSLO – Confocal scanning laser ophthalmoscopy

CV – Coefficient of variation

ELISA – Enzyme-linked immunosorbent assay

FDA – Food and Drug Administration

GCL – Ganglion cell layer

GNR – Gold nanorod

HEPES - N-(2-hydroxyethyl)piperazine-N'-2-ethanesulfonic acid buffer

ILM – Internal limiting membrane

INL – Inner nuclear layer

IPR – Inner plexiform layer

IRC – Inner retinal complex

IS/OS – Inner-segment/outer-segment junction

MRI – Magnetic resonance imaging

NIR – Near infrared

OCT – Optical coherence tomography

ONH – Optic nerve head

PBS – Phosphate buffered saline

PSS – Polystyrene sulfate

PEG – Polyethylene glycol

RGC – Retinal ganglion cell

RNFL – Retinal nerve fiber layer

RPE – Retinal pigment epithelium

SD-OCT – Spectral-domain optical coherence tomography

SD – Standard deviation

SS-OCT – Swept-source optical coherence tomography

TRT – Total retinal thickness

1.0 INTRODUCTION

Optical coherence tomography (OCT) is a noncontact imaging modality that provides cross-sectional images of biological structures, *in-vivo* and non-invasively, by detecting light backscattered from tissue. In ophthalmology, OCT is primarily used to image the retina and optic nerve, in order to detect and monitor a variety of retinal diseases and optic neuropathies. The use of OCT has increased in recent years, due to software and hardware improvements¹⁻⁴ that allow rapid collection of high-resolution, three-dimensional (3D) datasets, and clinical studies confirming the reproducibility⁵⁻¹¹ and disease-discriminating capability¹²⁻¹⁷ of measurements. OCT is now becoming accepted as a reliable tool for clinicians assessing ocular structure.

Contrast agents are substances designed to alter the detected signal of a biological image in a way that allows the region containing the agent to be discernible. For example, in X-ray imaging, high atomic number elements such as iodine are routinely used to improve delineation of blood vessels and organs by the absorption of incident X-rays.¹⁸ Medical imaging techniques such as X-ray, magnetic resonance imaging (MRI), computed tomography and ultrasound each may be augmented by contrast agents approved by the Federal Drug Administration (FDA).^{18, 19}

To date, there are no FDA-approved contrast agents for imaging with OCT. The existence of such an agent would have the potential to improve delineation of ocular structures that normally exhibit minimal backscatter and thus have low contrast within optical cross-sections. Given the nature of OCT detection, the presence of scattering media at the level of

low-scattering regions of interest may provide the contrast needed to isolate those structures. Gold nanoparticles can be nanoengineered to be highly backscattering at the near infrared (NIR) wavelengths used in OCT imaging.^{20, 21} Moreover, their surfaces can be modified to allow antibody conjugation.^{22, 23} These properties make gold nanoparticles a natural choice for targeted contrast within OCT images.

The central hypotheses of this dissertation are that nanoparticles can improve contrast by modulating the intensity of backscattered light detected by OCT and that they could be directed to ocular structures of interest using antibodies specific to cellular markers.

1.1 OPTICAL COHERENCE TOMOGRAPHY

OCT is based on the principles of interferometric detection, in which light echoes backscattered from the retina interfere with light that has traveled to a reference mirror at a known time delay. Echoes from a single point on the retina represent an axial scan (A-scan), and optical cross-sections (B-scans) are obtained by scanning the OCT beam in the transverse direction.

The center wavelength of the light source used for OCT imaging dictates depth of penetration into the retina, and the bandwidth of the light source governs axial resolution (Δz) as follows:

$$\Delta z = l_c/2 = [(2\ln 2)/(\pi n)] * [(\lambda^2/\Delta\lambda_{\text{FWHM}})]$$

where l_c is the coherence length, λ is the center wavelength, and $\Delta\lambda_{\text{FWHM}}$ is the full width at half-maximum of the applied light, and n is the refractive index of the sample.²⁴ Traditionally, center wavelengths of ~840 nm and bandwidths of ~25 nm have been used for ocular imaging to provide structural details of the inner retina at a resolution of ~8-10 μm . Recently, light sources

with longer center wavelengths (1050 nm, 1310 nm) have been employed in addition to the 830 nm sources for enhanced depth penetration (e.g., lamina cribrosa and choroidal imaging) and improved signal quality in subjects with lens opacities.²⁵⁻²⁹ In addition, broader bandwidth light sources ($\Delta\lambda=100-200\text{nm}$) have been integrated into OCT systems to improve axial resolution to $1-3\mu\text{m}$,^{1,30,31} and high-speed scanning (60-100x faster than the first-generation OCT system) is now possible using Fourier/spectral domain (SD-) OCT detection.^{2,3,32-35}

Fourier-domain detection, which consists of both spectral-domain (SD-OCT; Figure 1) and swept-source (SS-OCT) methods, does not require a moving reference mirror to collect A-scan profiles. Instead, frequency information from all depths at a given point on the retina is acquired simultaneously by a CCD camera and spectrometer (SD-OCT), or by sweeping through a range of frequencies (SS-OCT); frequency data are subsequently translated into intensity information using a Fourier transform. Speeds of up to 312.5 kHz have been accomplished with SD-OCT³⁶ and 249 kHz with SS-OCT.²⁹

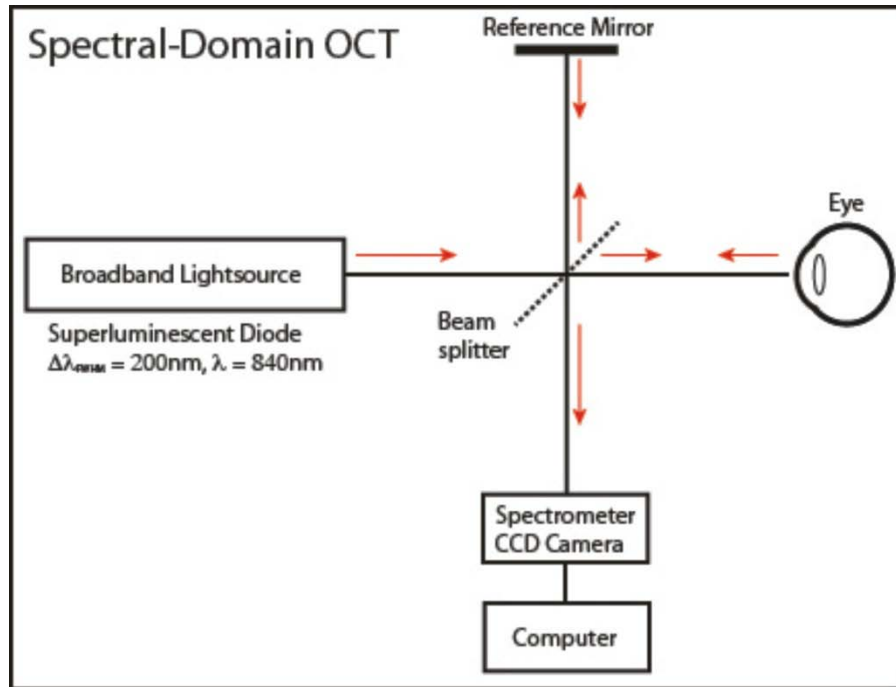


Figure 1. Schematic diagram of our spectral-domain OCT system. Light from a broadband superluminescent diode is split, with 80% going to the eye and 20% to a stationary reference mirror. The light recombines and an interference pattern is detected using a spectrometer and charge-coupled device (CCD) camera, and Fourier-transformed to obtain a reflectivity profile. Red arrows indicate the optical path. $\Delta\lambda_{FWHM}$ - full width at half-maximum of the applied light; λ - center wavelength.

Two-dimensional collection of intensity information involves transverse scanning across a retinal region of interest to gradually acquire a series of neighboring A-scans. Taken together, these A-scans comprise B-scans or optical cross-sections of tissue (Figure 2).

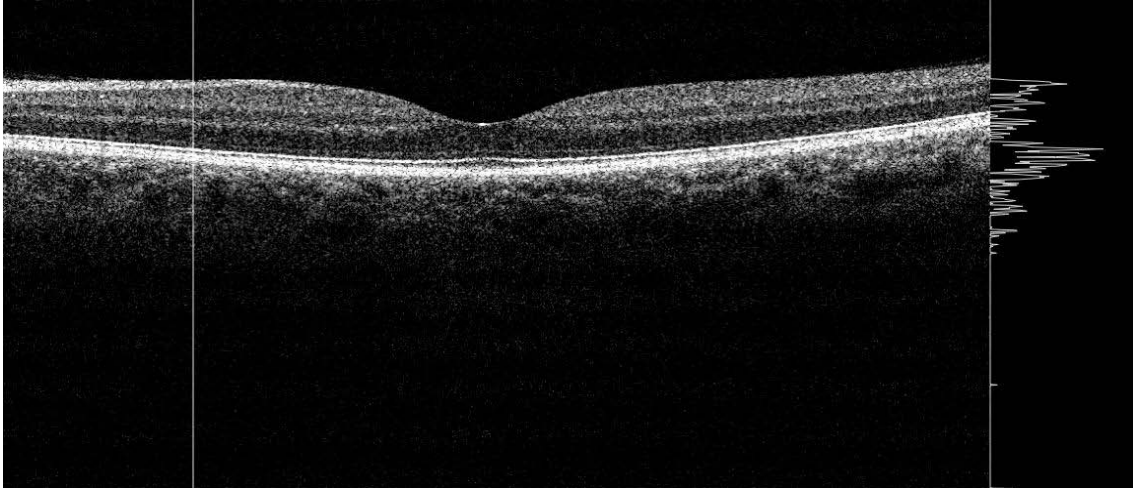


Figure 2. Two-dimensional SD-OCT cross-sectional scan (B-scan) through the macula of a human subject. The vertical white line denotes the location of the single A-scan intensity profile shown on the right. This macular cross-section scan consisted of 1000 A-scans, 1024 pixels in depth (6 mm x 2 mm).

In three-dimensional (3D) OCT, the collection of intensity information involves the acquisition of several neighboring B-scans. Volumes of data consist of multiple A-scans per B-scan and multiple B-scans per 3D volume. Once a 3D volume has been acquired, an OCT enface (OCT fundus) image can be created by integrating intensity information along the axial direction, such that one summed A-scan represents a single pixel in the OCT fundus image (Figure 3).

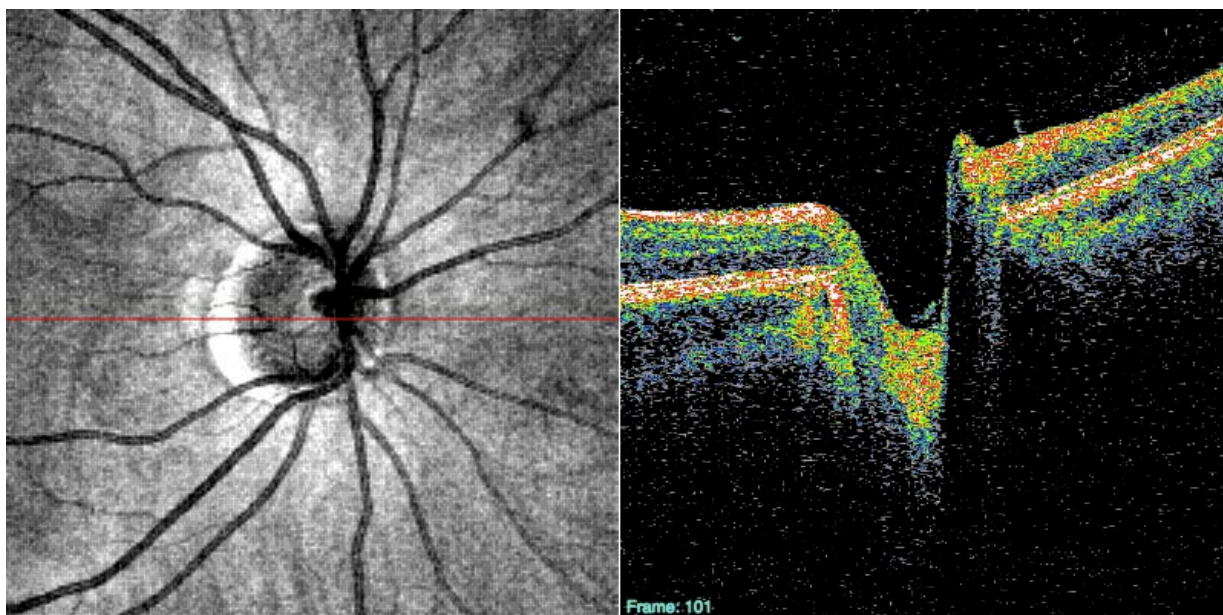


Figure 3. SD-OCT fundus image of the optic nerve head region of a human subject (left) created by summing a 3D data cube in depth (6.0 x 6.0 x 2.0 mm; 200 x 200 x 1024 pixels). A single cross-section through the optic nerve, at the level of the red line in the SD-OCT fundus image (right).

1.2 GLAUCOMA IMAGING WITH OPTICAL COHERENCE TOMOGRAPHY

Primary open angle glaucoma is the second leading cause of blindness in the United States, affecting approximately 2% of adults over the age of 40.^{37, 38} The gradual loss of retinal ganglion cell bodies and their axons results in a characteristic thinning of the retinal nerve fiber layer (RNFL) seen in glaucoma. However, at least 25-35% of retinal ganglion cells must be lost before changes in visual function can be detected using the most sensitive automated visual field testing methods.³⁹⁻⁴¹

OCT has grown to be a clinical standard of care for the assessment of ocular structure since becoming commercially available more than a decade and a half ago. Conventionally, the

most common scan patterns in glaucoma imaging were a 3.4 mm scan around the optic nerve head (ONH), and six equally spaced radial scans through the macula (6 mm) and optic nerve (4 mm). Retinal nerve fiber layer (RNFL) thickness is obtained via automated RNFL segmentation in the circumpapillary scan protocol, while macular thickness (internal limiting membrane, ILM, to the photoreceptor inner segment-outer segment junction (IS-OS)) is automatically segmented in the macular scan pattern. The optic nerve scan is used to obtain cup area, disc area, cup diameter, disc diameter and rim area. Parameters obtained using ONH and RNFL scanning protocols have been shown to be different in healthy and glaucomatous eyes,^{12, 13, 15-17, 42, 43} and have good glaucoma discriminating ability.⁴⁴ In addition, RNFL measurements obtained using information from a 3D volume of data have a higher reproducibility as compared to the conventional 3.4 mm scan protocol.¹¹

Different approaches have been introduced for quantifying 3D RNFL measurements. We developed a method for analyzing the measurements in terms of a thickness profile as distance from the ONH increased.⁴⁵ In healthy human eyes, the slope of RNFL thickness increased near the margin of the ONH, peaked, and then decreased with increasing distance from the ONH center in all but the nasal quadrant, which linearly decreased starting from the disc margin. Another approach (Ishikawa H, et al. IOVS 2009;50:ARVO E-Abstract 3328) exploits 3D macular data, which have been summarized using segmentation of the inner retinal complex (IRC: retinal ganglion cell layer (GCL), inner plexiform layer (IPL), inner nuclear layer (INL)). This approach reduces IRC data to superpixels (4x4 adjacent sampling points) and compares these superpixels to a normative thickness superpixel dataset. By condensing measurements into superpixels, it is less likely that small imaging artifacts or algorithm failure will have an effect.

Despite these novel approaches to analyzing 3D datasets, one critical piece is still missing: segmentation of every retinal layer. While it is possible to reliably segment – and therefore quantify – strongly reflecting layers such as the RNFL, highly transparent layers are nearly impossible to automatically segment. For example, the GCL is nearly impossible to reliably quantify using OCT technology in its current state. A method for selectively enhancing the contrast from this layer could permit objective quantification of the GCL. If detectable glaucomatous changes in the GCL precede changes that can be seen in the RNFL, it may be possible to identify the disease in the presence of a contrast agent and start treatment earlier in order to preserve vision. In addition, detecting changes in the GCL in a single patient over time may enhance longitudinal follow-up.

1.3 NANOPARTICLES

In 1959, Richard Phillips Feynman, a physicist at Caltech, gave a lecture at a meeting of the American Physical Society entitled, “There’s Plenty of Room at the Bottom.” Feynman speculated on the theoretical miniaturization of materials including the advent of a “mechanical surgeon” designed to target troubled areas in the body.⁴⁶ At the time, the term “nanotechnology” did not exist, and was not coined until 1974 by Norio Taniguchi. In 1986, K. Eric Drexler published the book, *Engines of Creation* in which he forecasted that nanotechnology would revolutionize medicine.

Since the publication of *Engines of Creation*, there have been considerable breakthroughs in nanomedicine, including the development of biodegradable polymeric nanoparticles for targeted drug delivery,⁴⁷ nanoparticle contrast agents for MRI,⁴⁸ optical nanosensors,⁴⁹

photothermal destruction of cells⁵⁰ and more. The American Society for Testing and Materials (ASTM) International now officially defines a nanoparticle as, “a sub-classification of ultrafine particle with lengths in two or three dimensions greater than 1 nm and smaller than about 100 nm”.⁵¹

Health-related publications using nanoparticles have grown substantially since early papers in 1978 (Figure 4). Given their increased popularity, and potential to aid in *in-vivo* diagnostics and drug delivery, there has been a parallel growth in concern over their effects on the human body.⁵²

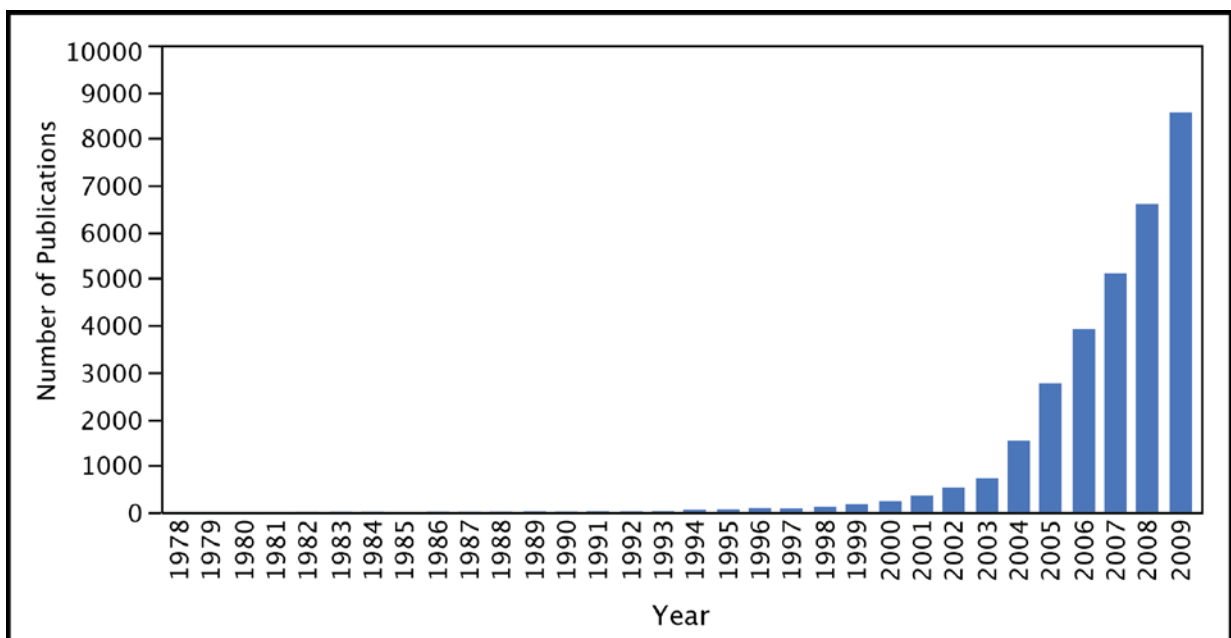


Figure 4. Number of PubMed publications using nanoparticles from 1978 (first publication) through 2009 (PubMed search: (nanoparticles) AND "Year"[Publication Date] : "Year"[Publication Date]).

Gold nanoparticles may offer a biocompatibility advantage over carbon and iron oxide nanoparticles used in medical imaging as contrast agents. Gold salts have been used to treat rheumatoid arthritis,^{53, 54} but the exact mechanism by which they suppress inflammation is unclear.⁵⁵ The literature on the utility and biocompatibility of gold nanoparticles is limited, however, as is the scope of their use as medical imaging contrast agents.

Nanoparticles in the form of colloidal solid gold spheres, nanorods (GNRs), nanoshells and nanocages have been fabricated to induce light scattering and absorbing changes at NIR wavelengths.^{21, 56-61} One of the most suitable biological applications for GNRs is optical imaging in the NIR spectral region as a result of their aspect ratio. Both GNRs and gold nanoshells have been used by researchers to alter scattering in OCT images.^{50, 58, 59, 61-65}

1.4 GOLD NANORODS AS OPTICAL IMAGING CONTRAST AGENTS

When an electromagnetic field is incident upon gold nanoparticles, mobile electrons (plasma) on the metal surface collectively oscillate in a phenomenon known as surface plasmon resonance (SPR; Figure 5). Particles have a specific resonant frequency that depends on their size and shape.⁶⁶

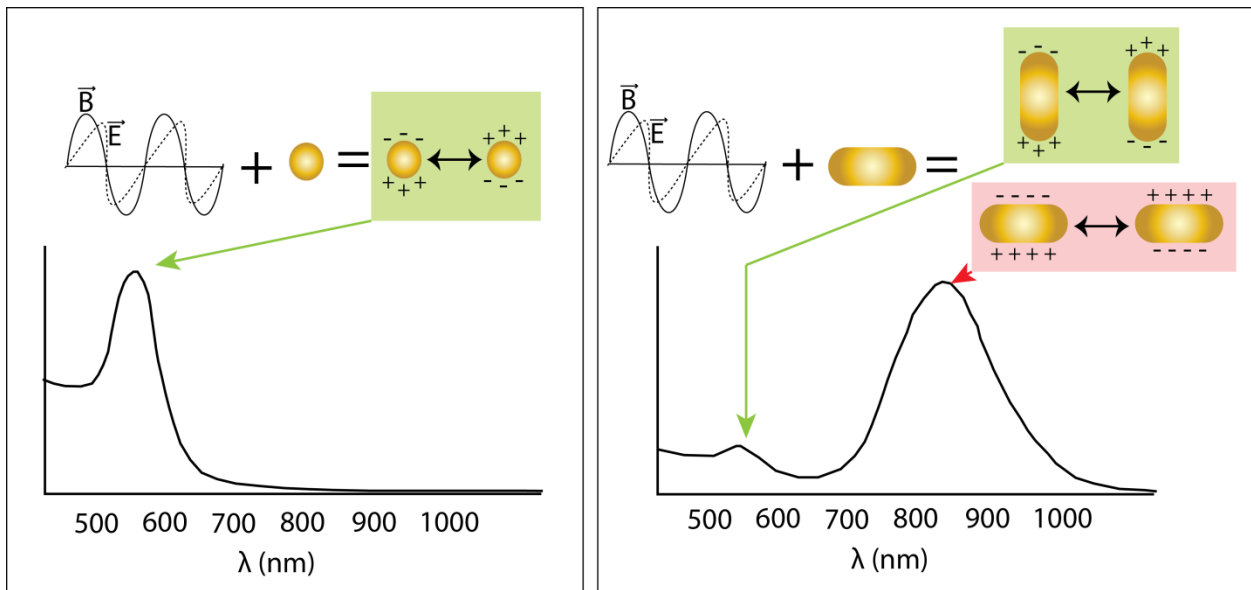


Figure 5. Demonstration of surface plasmon resonance (SPR). An electromagnetic wave interacts with spherical particles and resonance occurs along one axis; when the same wave interacts with nanorod, resonance occurs along the long and short dimensions and causes SPR along the length and width of the particle.

Spherical (colloidal) gold nanoparticles resonate in one direction because of their symmetry, and typically have a resonant wavelength around 520-550 nm (Figure 5, left).⁶⁶ GNRs are defined as solid rod-like particles characterized by their aspect ratio (length divided by width). Unlike symmetric gold nanospheres, SPR occurs along the longitudinal and transverse dimensions of the rod. When light is incident upon the transverse dimension of the GNRs, the result is a resonant wavelength similar to colloidal gold, while the longitudinal dimension results in scattering at longer wavelengths (Figure 5, right). Thus, it is possible to tune the resonance wavelength of GNRs by changing their dimensions. Longer GNRs exhibit SPR in longer wavelengths, and can be tuned to resonate at NIR wavelengths (Figure 6).^{20, 67} This makes GNRs attractive for optical imaging with OCT, where light sources around with a center wavelength of 850 nm are common.

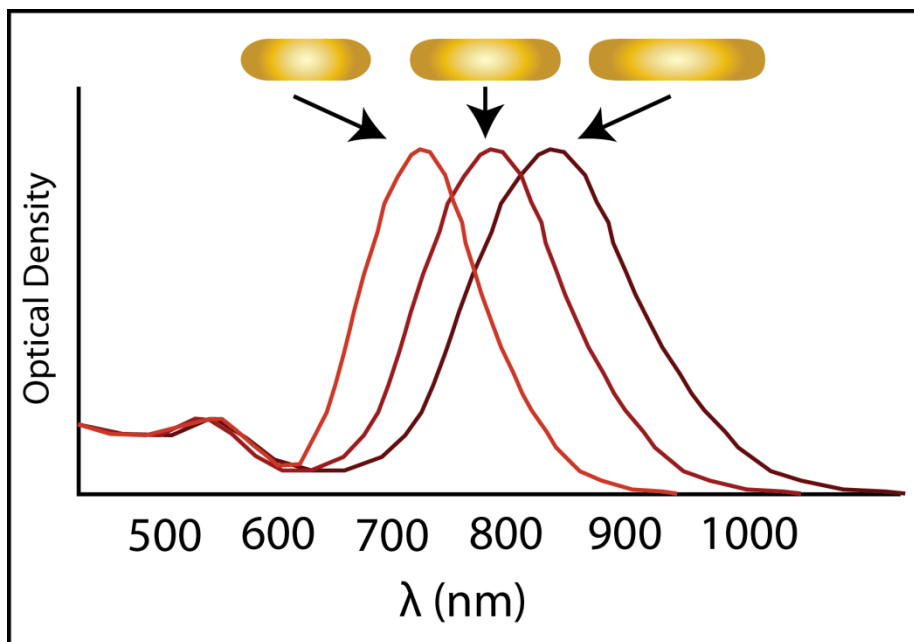


Figure 6. Theoretical tuning of longitudinal resonance wavelength in GNRs, which is dependent upon GNR aspect ratio. Given the same width, longer rods will have a longer resonant wavelength.

Investigation into the use of exogenous contrast agents with OCT has been growing in recent years. Yang et al used spectral triangulation techniques to map the distribution of indocyanine green in the *Xenopus laevis* using OCT.⁶⁸ Lee et al used colloidal gold nanoparticle-coated oil-filled microspheres and OCT to image a mouse liver⁵⁶ in one of the first studies to demonstrate that exogenous OCT contrast agents showed more structural detail as compared to a control animal *in-vivo*.

Magnetic nanoparticles have been used to enhance contrast in magnetically labeled cells *in-vitro* and *in-vivo* in *Xenopus laevis* imaged by OCT in the presence of a magnetic field.^{69, 70} While the technique of magnetomotive OCT may be promising, it requires a hardware modification of the OCT system to induce magnetic flux. In addition, the potential for thermal tissue damage resulting from the oscillation of the magnetic particles in the presence of a magnetic field has yet to be determined.

Several studies have shown the potential for gold nanoparticles to be used as scattering contrast agents for detection by OCT.^{50, 56-59, 61, 63} Gold is potentially a realistic candidate for contrast agent material because of its biocompatibility.⁷¹ As previously discussed, gold nanoparticles also have a strong SPR in the visible and NIR region of the electromagnetic spectrum.^{20, 67} Because they have tunable optical resonances that can be varied over several nanometers and OCT imaging takes place at NIR wavelengths, nanoparticles can be designed to resonate at or near the center wavelength of an OCT light source.

Agrawal et al reported successful OCT imaging of gold nanoshells in solution and gold nanoshells in a turbid tissue phantom model consisting of polystyrene microspheres in water and showed an intensity gain compared to control solution and phantom.⁵⁹ Different concentrations and geometries of the nanoparticles were investigated and resulted in varying intensity changes.

Gold nanorods with SPR wavelengths that overlap the OCT source wavelengths were fabricated by Troutman et al, who demonstrated an increase in signal of 4.5 dB relative to a polyacrylamide tissue phantom using time-domain (conventional) OCT.⁶¹

The ability to functionalize nanoparticles with antibodies that can lead them to molecular targets also makes them appealing candidates for optical imaging contrast agents. Such a technique has been employed by cancer researchers to target and ablate malignant cells. El-Sayed et al used colloidal gold nanoparticles conjugated to monoclonal anti-epidermal growth factor receptor (anti-EGFR) antibodies and incubated these functionalized particles with a nonmalignant epithelial cell line and malignant cell lines.²² The anti-EGFR antibody conjugated nanoparticles were bound to the surface of the malignant cells with 600% greater affinity as compared to nonmalignant cells as determined by microabsorption spectra and light scattering images. Similarly, Sokolov et al describe enhanced scattering from gold colloid nanoparticles conjugated to anti-EGFR for targeted optical imaging of cervical cancer cells.²³

To our knowledge, there have not been any studies using antibody-coated nanoparticles as contrast agents for ocular OCT imaging. Because the use of OCT in ophthalmology is widespread and rapidly growing, the field could benefit tremendously from the development of a contrast agent that can target specific ocular components.

1.5 PROJECT OBJECTIVES

Our goal is to alter local optical scattering properties of tissue so they can be detected by OCT. It is imperative to first determine how these particles interact with ocular tissue and whether they will specifically bind to structures of interest. The distribution and behavior of gold nanoparticles

after introduction into the eye is not documented. The organizing hypotheses of this dissertation were that nanoparticles could improve contrast by modulating the intensity of backscattered light detected by OCT and that they could be directed to ocular structures of interest using antibodies specific to cellular markers. To examine these hypotheses, the following objectives were realized:

1.5.1 Objective 1

To establish a reliable method for OCT imaging of the healthy and diseased mouse eye in order to provide a platform for testing the utility of OCT contrast agents for ocular imaging.

1.5.2 Objective 2

To develop antibody-conjugated gold nanoparticles suitable for targeting specific structures and enhancing OCT image contrast in the mouse eye.

1.5.3 Objective 3

To examine the localized contrast-enhancing ability and biocompatibility of gold nanoparticle contrast agents *in-vivo*.

2.0 MOUSE IMAGING WITH OPTICAL COHERENCE TOMOGRAPHY

Murine imaging with OCT is becoming increasingly popular given their relatively low cost and short lifespan – and therefore shorter time for disease progression. In addition, many transgenic models are easy for researchers to access. OCT has been used to study ocular dimensions⁷² and characterize normal eye growth⁷³ as well as growth of eyes in mouse models of myopia.⁷⁴ Mouse models of retinal degeneration have been imaged using time-domain OCT,^{75, 76} and healthy and degenerative mice with SD-OCT.⁷⁷⁻⁸⁴ While these studies provided qualitative structural evidence of change associated with retinal degeneration, automated measurements were not available. The ability to automatically obtain measurements from 3D scans of the mouse retina may provide the objective, quantitative analysis necessary for disease monitoring.

2.1 REPRODUCIBILITY OF MEASUREMENTS IN HEALTHY MICE

In human eyes, retinal thickness and retinal nerve fiber layer thickness measurements obtained with OCT have been shown to be reproducible,^{5, 7, 8, 11, 85-90} and this has made OCT valuable for cross-sectional and longitudinal studies.⁹¹⁻⁹³

In mice, time-domain OCT has been used to obtain cross-sectional images of the retina *in-vivo*.^{75, 76, 78} SD-OCT, which has faster scanning rates and higher axial resolution, allows the acquisition of 3D volumetric scans in mice.^{77, 79-82, 84, 94-96} Despite acquiring volumetric

information in mice, thickness measurements obtained post-hoc were often based on single cross-sections.^{79, 81}

In considering the use of SD-OCT for the longitudinal follow-up of mouse models of retinal diseases, however, a method for consistently acquiring 3D data must be developed. The goal of this study was to evaluate the reproducibility of a method for measuring total retinal thickness (TRT) in mice using SD-OCT.

2.1.1 Methodology: Animals, Imaging, Alignment Considerations and Image Registration

This experiment was approved by the University of Pittsburgh's Institutional Animal Care and Use Committee and adhered to the Association for Vision Research in Ophthalmology (ARVO) Statement for the Use of Animals in Ophthalmic and Vision Research.

Healthy adult male C57Bl/6 mice (Jackson Laboratory, Bar Harbor, ME) were used in this study. Mice were maintained in the University of Pittsburgh Animal Facility with a 12-hour light/dark cycle and free access to water and standard laboratory feed.

Mice were anesthetized with an intraperitoneal injection of ketamine (Ketaject, Phoenix Pharmaceuticals, St. Joseph, MI; 80 mg/kg) and xylazine (Xyla-ject, Phoenix Pharmaceuticals, St. Joseph, MI; 5 mg/kg) in order to prevent large movements during SD-OCT image acquisition. Both pupils were dilated using a topically applied drop of Tropicamide (1%; Falcon Pharmaceuticals, Fort Worth, TX). In order to neutralize corneal optical power and focus the SD-OCT beam onto the retina, a thin glass cover slip was applied to the cornea and hydroxymethylcellulose ophthalmic demulcent solution (Goniosol 2.5%; Akon, Buffalo Grove, IL) was used to preserve corneal hydration and couple the cover slip to the cornea. Mice were

secured on a custom stage (Figure 7), which allowed for free rotation in order to align the eye for imaging of the optic nerve head (ONH).

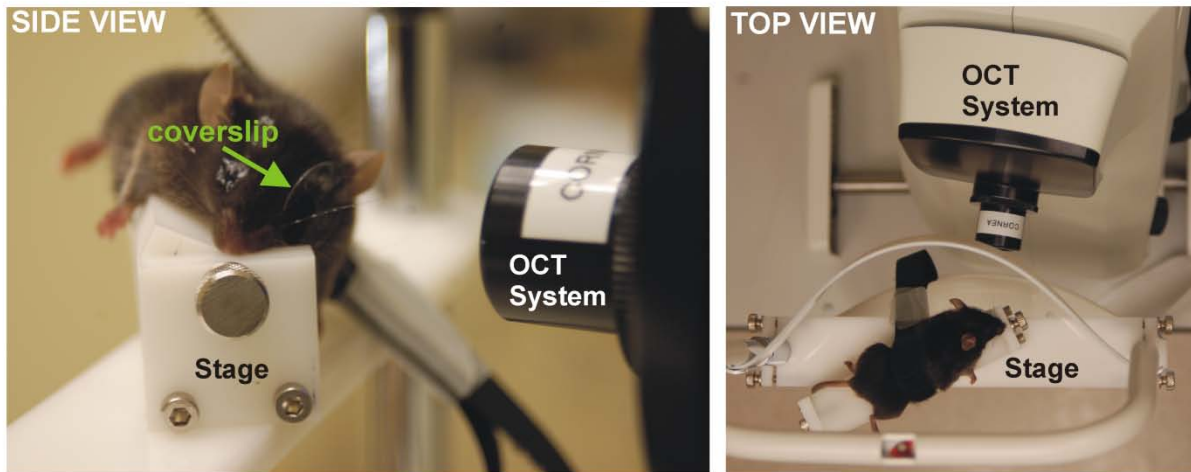


Figure 7. Side (left) and top (right) views of custom stage used for alignment of the mouse for SD-OCT imaging of the optic nerve head. A cover slip was used to neutralize the power of the mouse cornea (green arrow). *Gabriele ML et al. Reproducibility of SD-OCT TRT Thickness Measurements in Mice. Invest Ophthalmol Vis Sci 2010 Jun 23 [Epub ahead of print]. Copyright held by the Association for Vision in Research and Ophthalmology.*

Three repeated volumetric images, centered on the ONH, were acquired in both eyes (Bioptigen, Inc, Research Triangle Park, NC). All SD-OCT images consisted of 250 averaged A-scans (each A-scan was an average of 4 consecutive repeated A-scans), 250 frames, and 1024 samplings in depth. This corresponds to a volume of approximately 1.5 x 1.5 x 2.0 mm at the surface of the cover slip. Mice were repositioned in between each scan by rotating the stage (when switching between left and right eyes), or removing the mouse from the stage and completely repositioning (when returning to the same eye). Care was taken to ensure all three scans were acquired before mice developed reversible cataract;⁹⁷ all images were acquired within 20 minutes after receiving anesthesia.

Since repositioning the mouse between scans resulted in variability in the location and orientation of the ONH, we manually aligned the SD-OCT *enface* images after acquisition (Figure 8) to compensate for orientation variability. The first SD-OCT *enface* image acquired in a given eye was used as an alignment reference for subsequent images, and the coordinates of rotation and translation for each scan relative to reference were used to align thickness measurements as described below. We did not correct for magnification.

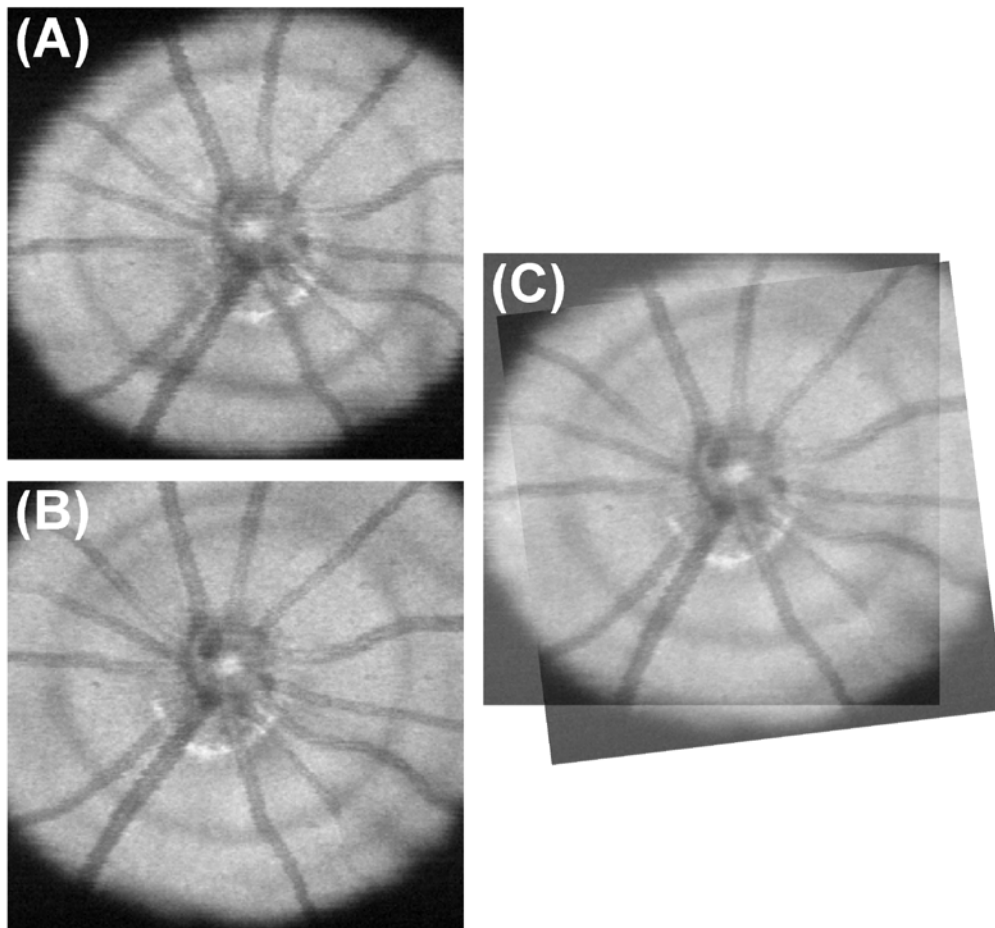


Figure 8. Manual alignment of two SD-OCT *enface* images. (A) Reference SD-OCT *enface* image and (B) subsequent SD-OCT *enface* image. (C) Subsequent scan registered to reference. *Gabriele ML et al. Reproducibility of SD-OCT TRT Thickness Measurements in Mice. Invest Ophthalmol Vis Sci 2010 Jun 23 [Epub ahead of print].*

Copyright held by the Association for Vision in Research and Ophthalmology.

The ONH margin for each eye was manually located by one experienced operator (MG) on each OCT *enface* image. The geometric center of the ONH margin was then used as a center point for subsequent analysis. TRT was automatically measured within a sampling band of retinal thickness with an inner radius of 55 pixels and an outer radius of 70 pixels (330-420 μm at the surface of the coverslip), centered on the ONH, using custom segmentation software to detect the internal limiting membrane (ILM) and retinal pigment epithelium (RPE; Figure 9). This sampling band was chosen to avoid regions within the optic nerve and areas of vignetting, as automated segmentation is not possible in those regions. After sampling band thickness information was obtained, scans were rotated and translated based on the coordinates obtained from manual image alignment. These aligned thickness measurements were used to assess reproducibility. It should be noted that alignment was completely independent of thickness measurements. In addition, there was often a motion artifact that occurred during acquisition as the result of respiration, as evident by the high frequency motion artifact seen in Figure 9. This was not corrected for when aligning fundus images.

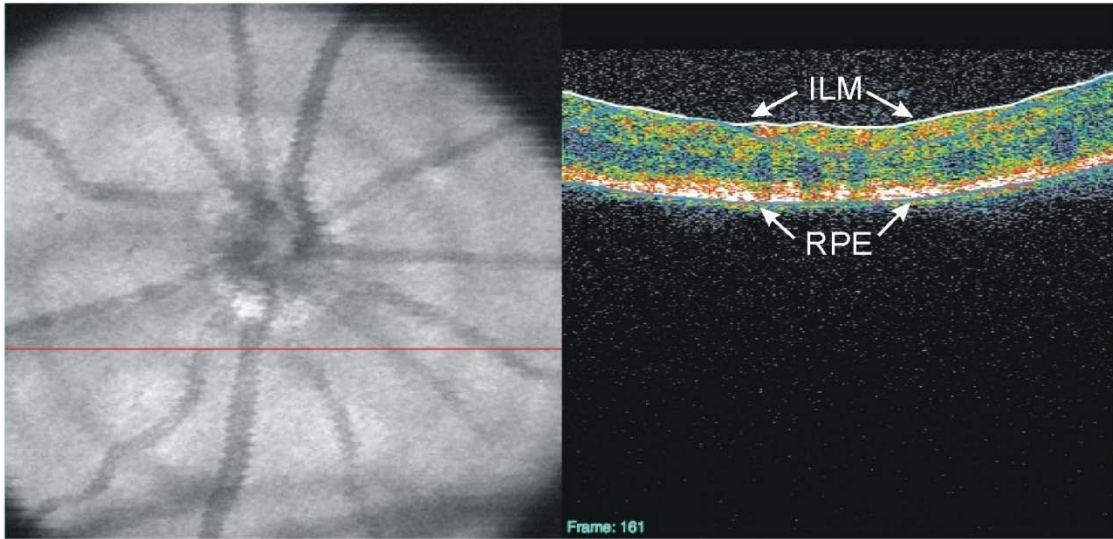


Figure 9. SD-OCT *enface* image (left) with the red line indicating the location of the OCT B-scan (right). The B-scan demonstrates automated segmentation of the internal limiting membrane (ILM, white line) and retinal pigment epithelium (RPE, blue line) to obtain total retinal thickness measurements. The vertical gray lines represent the disc margin.

SD-OCT *enface* images were checked to ensure that there was consistent image quality across the scan and that there were no areas of shadowing from media opacities within the TRT sampling band, as this could affect thickness measurements. Eyes were excluded if the TRT segmentation algorithm failed at any location inside the sampling band.

Algorithm failure was defined as a clear disruption of the border, either ILM or RPE, for greater than 5 consecutive A-scans within the sampling band. If any one of the three scans per eye had to be excluded, the mouse (both eyes) was excluded from the analysis.

2.1.2 Statistical Analysis

Linear mixed effects models were fitted to global and quadrant TRTs, taking into account the clustering between eyes, in order to assess measurement reproducibility. Imprecision (as measured by the residual standard deviation (SD)) and corresponding 95% confidence intervals were computed. All analysis was conducted using *R* Language and Environment for Statistical Computing program (<http://www.R-project.org>; date accessed: February 1, 2010). An α level of 0.05 was used as a cutoff for statistical significance.

The mixed effects model for TRT (y_{ijk}) for mouse i , eye k nested within mouse i , and replicate k is:

$$y_{ijk} = \alpha + a_i + b_{ij} + \varepsilon_{ijk},$$

where α represents the cohort mean TRT, a_i is the random intercept for mouse i (assumed to be Normally distributed with mean 0 and standard deviation σ_m ($a_i \sim N(0, \sigma_m^2)$)), b_{ij} is a random intercept for eye j nested within mouse i ($b_{ij} \sim N(0, \sigma_e^2)$), and ε_{ijk} is a Normally distributed random error ($\varepsilon_{ijk} \sim N(0, \sigma^2)$). The standard deviations σ_m and σ_e represent the variability of the thickness measurements coming from the cohort of mice (heterogeneity across mice and eyes, respectively), while the error standard deviation represents the imprecision coming from the device. This device-related imprecision includes error coming from segmentation algorithm performance as well as the manual alignment of SD-OCT *enface* images.

2.1.3 Results

Thirty eyes from 15 healthy adult male mice, age 13 weeks, were imaged in this study. Two eyes were excluded due to segmentation algorithm failure, one at the level of the RPE and one at the ILM. The contralateral eyes from those two mice were also excluded. In total, 26 eyes from 13 healthy adult male mice were included in this study. Figure 10 shows one example of alignment of TRT maps relative to reference.

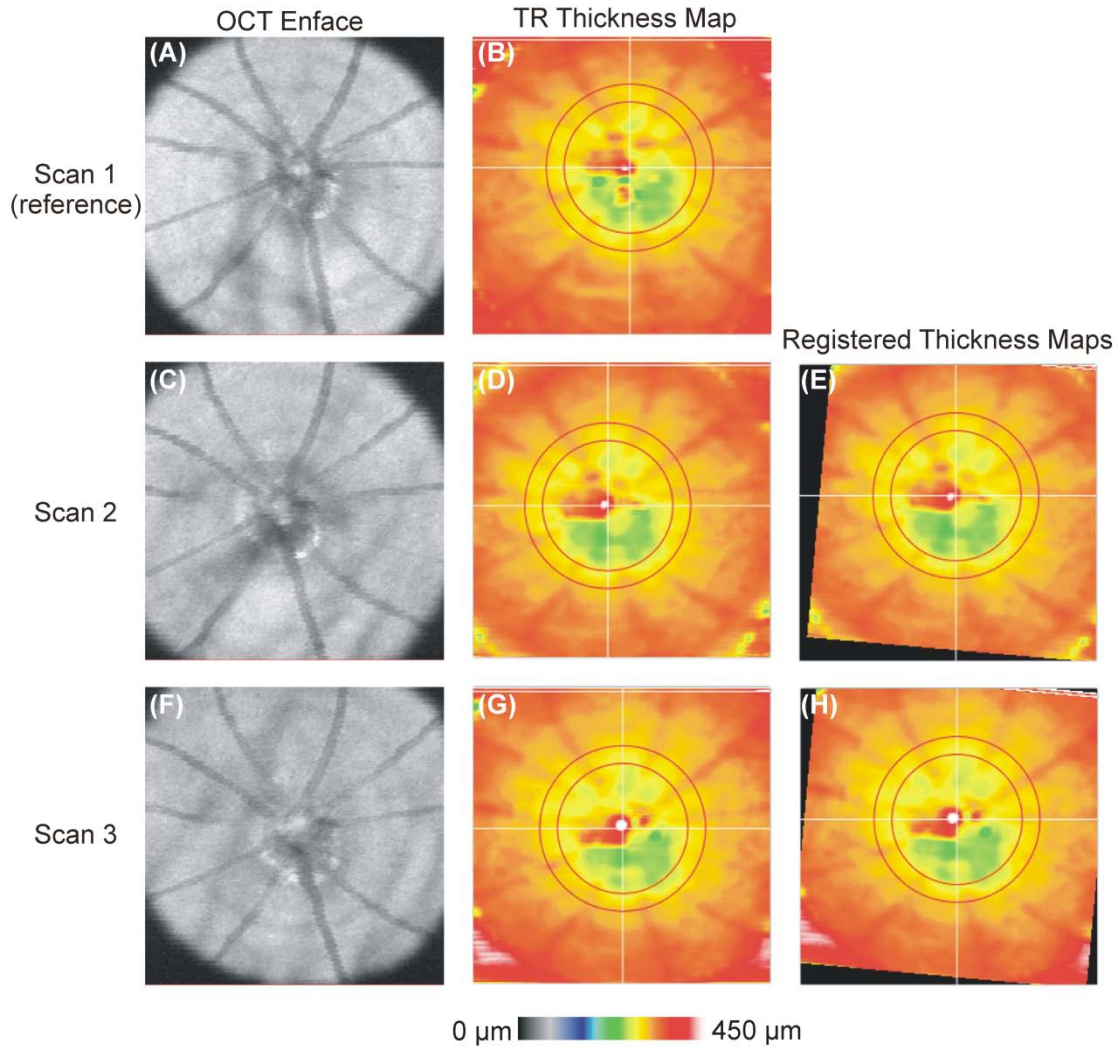


Figure 10. Total retinal thickness maps aligned to a single reference scan. (A, C, F): SD-OCT *enface* images; (B, D, G): Total retinal (TR) thickness map with sampling region indicated as the region between red concentric circles (E, H): Total retinal thickness maps, registered to reference. *Gabriele ML et al. Reproducibility of SD-OCT TRT Thickness Measurements in Mice. Invest Ophthalmol Vis Sci 2010 Jun 23 [Epub ahead of print]. Copyright held by the Association for Vision in Research and Ophthalmology.*

Mean global TRT across all eyes was 298.21 μm (Table 1), with a mouse heterogeneity SD of 4.88 μm (coefficient of variation (CV) = 0.016) and an eye SD of 3.32 μm (CV= 0.011). The device-related global imprecision SD was 2.33 μm (CV = 0.008). The superior quadrant

showed the thickest TRT measurements (310.38 μm , mouse heterogeneity SD 6.09 μm (CV = 0.020), eye SD 6.98 μm (CV = 0.022)) while the inferior quadrant was the thinnest (291.55 μm , mouse heterogeneity SD 6.02 μm (CV = 0.021), eye heterogeneity SD 8.13 μm (CV = 0.028)). The highest (worst) quadrant imprecision SD was in the superior quadrant (3.13 μm ; CV = 0.010) and lowest (best) in nasal quadrant (2.06 μm ; CV = 0.007).

Table 1. Estimates of mixed effect model parameters and coefficient of variation (CV) for global and sectoral total retinal thickness. All estimates are in microns (μm) except for CV, which is unitless.

Sector	Estimated Mean (α)	Estimated SD				Imprecision SD	
		Mouse		Eye		SD* (σ)	CV
		σ_m	CV	σ_e	CV		
Global	298.21	4.88	0.016	3.32	0.011	2.33	0.008
Temporal	294.37	6.17	0.021	4.80	0.016	3.05	0.010
Superior	310.38	6.09	0.020	6.98	0.022	3.13	0.010
Nasal	296.52	4.61	0.016	6.08	0.021	2.06	0.007
Inferior	291.55	6.02	0.021	8.13	0.028	3.09	0.011

* Device reproducibility measurement

2.1.4 Summary and Discussion

In this study, we were able to demonstrate good intravisit reproducibility of SD-OCT TRT measurements in mice that were obtained using automated retinal segmentation software. This lays the foundation for future studies monitoring retinal changes in mice over time. We showed global imprecision estimates were 2.33 μm . Hence, a TRT difference between two observations from the same eye of the same mouse of at least 6.46 μm ($2.33\mu\text{m} * 1.96 * \sqrt{2}$; 2.17% of the mean TRT; 3.31 pixels) would be necessary to conclude, with 95% confidence, that the difference was due to an actual structural change as opposed to variability inherent to the device.

While the superior quadrant showed the worst quadrant imprecision SD (3.13 μm), the superior CV (0.010) was actually slightly better than that of the inferior quadrant (CV = 0.011). This discrepancy is attributed to the differences in thickness within those quadrants: the superior quadrant had the thickest measurements, while the inferior quadrant measurements were thinnest (310.38 μm versus 291.55 μm , respectively). Overall, the CV was similar for the superior, inferior and temporal quadrants, but was lower in the nasal quadrant (CV = 0.007). Our study was designed to evaluate intravisit reproducibility, as mice were only anesthetized once and repeatedly scanned in one session. This was observed in multiple studies to be the main source of variability with OCT imaging.^{98, 99} Intervisit variability has been shown to add minimal variability and was therefore not the focus of this study.⁹⁹

While our TRT measurements are thicker than those reported by Horio et al,⁷⁵ they only reported temporal retinal thickness from a single A-scan at a distance of 1-2 disc diameters from the temporal margin of the optic disc. This was further from the disc center than we measured and can therefore be expected to show a lower retinal thickness.⁴⁵ In addition, since their measurement was based on a single A-scan, there may have been large variability in their measurements. They also used a lower resolution OCT system as well as a different strain of mice (Balb/c), which was older (16 weeks), all of which may explain the observed differences. Li et al⁷⁶ showed retinal thickness measurements of approximately 200-250 μm in C57Bl/6 mice. Their measurements were based on single cross-sections and used a lower resolution OCT system. Ruggeri et al⁹⁴ measured retinal thickness using SD-OCT and reported an average retinal thickness of 202 μm . This average was based on all points outside of a 0.5 mm-diameter region covering the ONH, while our sampling location was within a band with a diameter of 55-70 pixels. We chose this sampling region to ensure that we were sampling outside the ONH region

and not extending into a region where there could be vignetting of the image from the pupil. Compared to our sampling region, their average included thinner regions of the retina, which may explain the difference in global measurements. In addition, differences in measurements due to different devices with different segmentation algorithms may partially explain this discrepancy. This may also explain the slight differences in our measurements as compared to those reported by Kim et al,⁷⁹ Huber et al,⁸¹ Fischer et al,⁸⁴ and Cebulla et al.⁹⁶

We observed slightly thinner TRT measurements inferiorly, which was unexpected. One reason for this finding may be that the orientation of the eye during scanning is not the true orientation of the mouse, since mice were rotated on a stage during acquisition to allow for focusing on the optic nerve head. This might have lead to variability of the exact quadrant boundary locations across eyes. This is a limitation inherent to our method for obtaining images centered on the ONH by rotating the mouse on a stage.

Another limitation of this study is that it requires manual labeling of the optic disc margin to obtain the geometric center of the disc. It is possible, however, that automated detection of the ONH (and ONH center) may be available in the future, similar to how it is currently detected in human eyes.¹⁰⁰ In addition, we used manual registration of *enface* images to account for rotational and translational eye position differences from scan to scan. This was necessary to account for shifts that occurred between scans because our stage allowed for rotation and translation of the eye in order to center the image on the ONH and account for x- and y- scan location differences. A stage that allows for more consistent alignment of mice between scans may alleviate this. It may also be possible to use automated registration based on blood vessel segmentation in *enface* images to eliminate the manual component of the analysis. Future studies investigating this are necessary.

We have shown that SD-OCT allows reproducible minimally-invasive 3D scanning of tissue structure *in-vivo*. Because of this, SD-OCT has the potential to reduce the number of mice needed in studies of diseases that affect retinal structure by allowing the same mice to be consistently followed from visit to visit. This means that longitudinal studies monitoring one population of mice are possible, as opposed to the current approach of cross-sectional analysis with a subset of mice at multiple time points. This will allow researchers to better observe the structural manifestations of disease over time, as demonstrated in the next section.

2.2 QUANTIFYING RETINAL THICKNESS CHANGES IN RESPONSE TO INJURY

Retinal ganglion cell (RGC) death induced by optic nerve crush injury has been used as a model to investigate axonal degeneration of the central nervous system in mice.¹⁰¹⁻¹⁰⁴ In adult mice, approximately 60% of RGCs are lost within three weeks after optic nerve crush injury, as determined by histology.^{101, 104}

Ophthalmic imaging techniques such as confocal scanning laser ophthalmoscopy (CSLO) and OCT can provide quantitative and detailed structural information from the retina and optic nerve head (ONH) region. *In-vivo* images of RGCs in mice and rats after optic nerve crush have been acquired using retrograde labeling and CSLO.¹⁰⁵⁻¹⁰⁷ Recently, Leung et al demonstrated the use of CSLO with Thy-1 cyan fluorescent protein expressing transgenic mice, to monitor RGCs *in-vivo* after nerve crush.¹⁰⁸ The authors in these studies were able to observe the loss of RGCs in the same eyes over time, contrary to previous experiments using histology that required several different animals at each time point.

OCT allows for non-invasive, *in-vivo* imaging of ocular structures, and has been used to obtain optical cross-sections of the mouse retina.⁷⁵⁻⁷⁸ Time-domain OCT^{75, 76} and spectral-domain (SD)-OCT^{79, 81, 83, 94, 109} imaging have been used to observe retinal thinning in mouse models of retinal degeneration. One study used SD-OCT to image axotomized rats, and manually obtained measurements of retinal layers in six cross-sectional images.¹¹⁰ This approach, however, is prone to subjective bias both in the selection of individual cross-sections and the manual segmentation of retinal layers. In order to fully benefit from the high resolution and rapid scanning provided by SD-OCT imaging, it would be desirable to obtain automated measurements from the area of interest. The goal of this study, therefore, was to investigate the longitudinal effect of optic nerve crush injury on total retinal thickness (TRT) in adult mice using automated segmentation analysis of SD-OCT images.

2.2.1 Methodology

This experiment was approved by the University of Pittsburgh's Institutional Animal Care and Use Committee and adhered to the ARVO Statement for the Use of Animals in Ophthalmic and Vision Research.

Healthy adult male C57Bl/6 mice (Jackson Laboratory, Bar Harbor, ME) were used in this study. Mice were maintained in the University of Pittsburgh Animal Facility with a 12-hour light/dark cycle and had free access to water and standard laboratory feed. Control animals were not exposed to any surgical procedure, while nerve crush animals had one optic nerve that was crushed.

Nerve Crush Procedure

Animals were anesthetized with an intraperitoneal injection of ketamine (Ketaject, Phoenix Pharmaceuticals, St. Joseph, MI; 80 mg/kg) and xylazine (Xyla-ject, Phoenix Pharmaceuticals, St. Joseph, MI; 5 mg/kg). An incision was made in the conjunctiva at the limbus and then the sub-Tenon's space was bluntly dissected posteriorly. The muscle cone was entered and the optic nerve exposed. The optic nerve was crushed with fine forceps for 3 seconds, approximately 1 mm posterior to the globe, under direct visualization (Figure 11). Care was taken not to damage surrounding blood vessels.

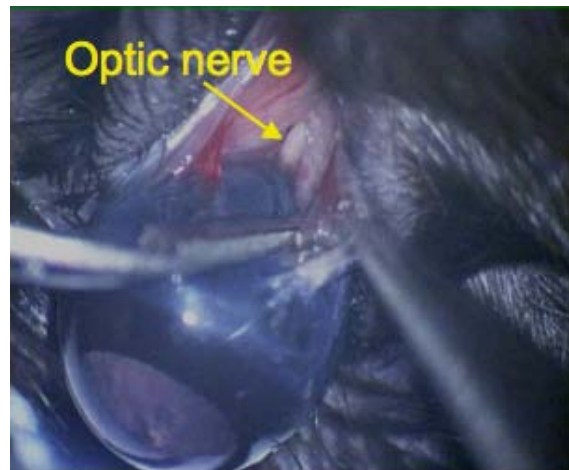


Figure 11. Optic nerve exposed for nerve crush surgery. *Photo courtesy of C. Leung.*

SD-OCT Imaging

Prior to each session, mice were anesthetized with an intraperitoneal injection of ketamine and xylazine in order to prevent large movements during SD-OCT image acquisition. Pupils were dilated using a topically applied drop of Tropicamide (1%; Falcon Pharmaceuticals, Fort Worth, TX). To neutralize corneal optical power and focus the SD-OCT beam onto the retina, a thin glass cover slip was applied to the cornea. Hydroxymethylcellulose ophthalmic demulcent solution (Goniosol 2.5%; Akon, Buffalo Grove, IL) was used to preserve corneal

hydration and couple the cover slip to the cornea. Mice were secured on a custom stage that allowed for free rotation in order to acquire images centered on the ONH.¹¹¹ All images were acquired within 20 minutes of the onset of anesthesia to avoid a reduction in signal intensity that can be caused by the occurrence of reversible cataract.⁹⁷

Volumetric images centered on the ONH (250 x 250 A-scans, 1024 samplings in depth per A-scan; 1.5 x 1.5 x 2.0 mm at the surface of the cover slip) were acquired using SD-OCT. Four consecutively repeated A-scans were collected and averaged at each location to improve signal-to-noise ratio. A SD-OCT scan obtained in each eye prior to nerve crush served as baseline in each nerve-crushed eye while the first imaging session was used as baseline in the control eyes. Follow-up scans were obtained at multiple days, up to 32 days post nerve-crush in both groups.

SD-OCT Image Analysis and Automated Segmentation

Since mice were rotated freely on our stage, and eyes could be oriented differently from scan to scan, we manually aligned SD-OCT *enface* images and performed automated segmentation from the ILM to the RPE as described in Section 2.1.1 and shown in Figures 8-10.¹¹¹ As in Section 2.1.1, TRT measurements within a sampling band with radii of 55-70 pixels (330-420 μm at the surface of the coverslip), centered on the ONH, were used. Scans were subsequently rotated and translated based on the coordinates obtained from manual image alignment, and global and sectoral average TRTs were computed. These aligned TRT measurements were used to assess retinal thickness changes over time.

SD-OCT Image Quality Analysis

SD-OCT *enface* images were subjectively checked to ensure that there was consistent image quality across the scan, and that there were no areas of shadowing from media opacities

within the TRT sampling band. In addition, we measured the quality index, as previously described,¹¹² along every A-scan in the data volume.

2.2.2 Statistical Analysis

Linear mixed effects models with polynomial (quadratic) terms were fitted to describe global and sectoral (temporal, superior, nasal, inferior quadrants) TRT of nerve crush and control eyes over time, with scan quality index included as a covariate in the analysis. This mixed effects analysis accounted for the repeated measurements over time and the use of both eyes from some animals. All analysis was conducted using R Language and Environment for Statistical Computing program (<http://www.R-project.org>; date accessed: March 22, 2010). An alpha level of 0.05 was used as a cutoff for statistical significance.

2.2.3 Results

Eight eyes from four healthy control mice (baseline age 64 ± 0 days) and eleven eyes from eleven nerve crush mice (baseline age 76 ± 11.8 days) were included in this study. All control eyes were scanned at baseline and eight consecutive sessions over the course of 31 days, while nerve-crushed eyes were followed for up to 32 days (average time of follow-up: 29.2 ± 4.0 days, average number of sessions 9.9 ± 0.7). In the control eyes, 4% (3/72) of global and 2% (7/288) of quadrant TRT measurements were excluded based on our quality criteria. These segments were excluded due to algorithm failure caused by low signal. In the nerve-crushed eyes, a total of 39% (43/109) of global and 29% (126/436) of quadrant TRT measurements were excluded. There was

a higher incidence of poor signal quality caused by shadowing from media opacities in nerve-crushed eyes, which caused algorithm failure.

Mean TRT across all eyes at baseline was $299.7 \pm 8.3 \mu\text{m}$. TRT showed an initial period of thickening, followed by a steep decrease and slight increase after day 21 in the nerve-crushed eyes (Figure 12). There was a statistically significant positive quadratic term in nerve-crushed eyes ($p < 0.05$ for global and sectoral measurements), but not in control eyes, which can be attributed to the initial phase of thickening. Control eyes showed a slight but statistically significant increase in slope over time ($p < 0.05$ for global and sectoral measurements). The fitted models for the nerve crush group showed a statistically significant difference from control for both linear and quadratic components ($p < 0.05$) for global and sectoral measurements. Image quality did not significantly affect TRT measurements for control or nerve-crushed eyes, except for the superior quadrant in nerve-crushed eyes ($p < 0.05$).

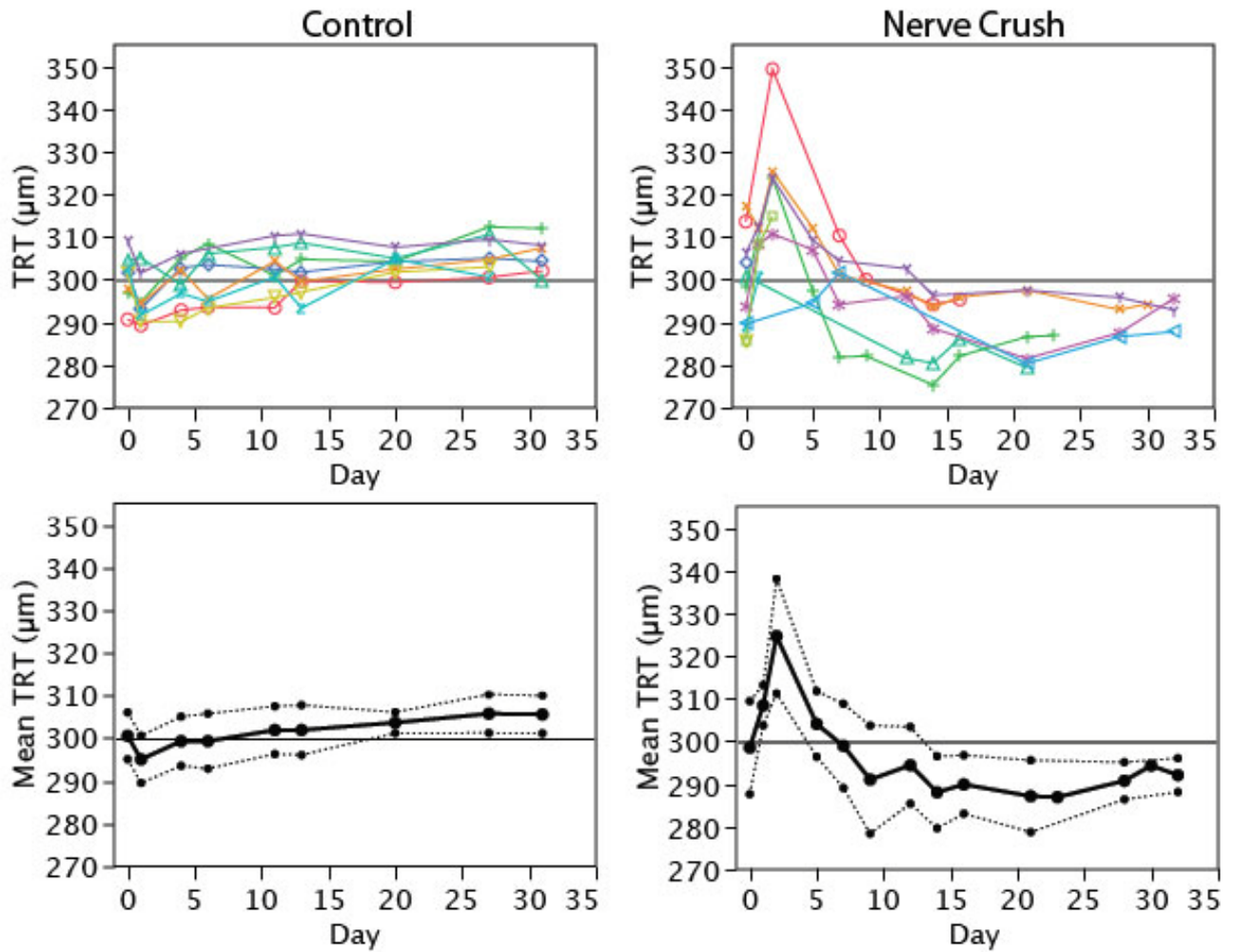


Figure 12. (Top) Individual total retinal thickness (TRT) measurements, each eye represented by a different color and (Bottom) mean global TRT over time for control and nerve-crushed eyes; the solid line represents mean thickness and dashed lines represent the standard deviation.

In order to eliminate the potential confounding effect of the initial TRT increase on the analysis, we performed a post hoc analysis using mixed effects modeling with TRT measurements acquired on or after day six, once the transient thickness increase resolved. Global and all sectoral measurements from nerve-crushed eyes had a statistically significant negative slope ($p < 0.05$). There was a statistically significant positive quadratic term for global

measurements as well as temporal, nasal and inferior quadrants ($p < 0.05$), and quality index was not a statistically significant covariate in any sector. There was no statistically significant quadratic term in the control eyes, but there was a statistically significant slight linear increase in thickness over time in global measurements as well as superior and inferior quadrants ($p < 0.05$).

2.2.4 Summary and Discussion

In this study, we demonstrated that quantification of longitudinal TRT changes is possible in untreated mice and following optic nerve crush using OCT with automated segmentation. We were able to follow a cohort of mice over time and therefore did not have to sacrifice mice at each time point to obtain structural information. This enables a true longitudinal assessment as opposed to attempting to extract a longitudinal effect from multiple cross-sectional data as in the case of histological sectioning. In addition, this can substantially reduce the number of animals to be used in such experiments.

The initial phase of retinal thickening that was seen in the nerve-crushed mice may be due to an inflammatory reaction causing transient edema. It is possible that this finding has not been reported previously because the increase of $\sim 25\mu\text{m}$ in TRT is difficult to detect clinically. Histological studies investigating retinal response to nerve crush observed mice at later time points and therefore missed early inflammation. In addition, dehydration and tissue shrinkage that occurs while processing tissue for histology may prevent edematous changes from being readily apparent. This highlights the advantages of non-invasive cross-sectional *in-vivo* tissue assessment.

While our crush procedure consisted of a single 3-second crush, the duration of the crush may affect the severity of damage and the persistence of early retinal thickening. It is possible

that exposure to a longer crush may induce a larger response, but we chose to limit the length of the crush in order to assess the utility of this imaging approach and to avoid complete axotomy or blood vessel damage.

Previous reports have shown a decrease in retinal ganglion cell count of ~60% by three weeks post-lesion.^{101, 104} While our results showed a decrease in thickness over time, our method is currently limited to measurements of the entire thickness of the retina. Hence, the exact axial location of changes within the retina is not known. It is possible that segmenting the RGC or retinal nerve fiber layer may show an even more noticeable decrease in thickness. However, at this stage, automated retinal nerve fiber layer thickness measurements are unreliable in mice because the retinal nerve fiber layer is especially thin.

Another limitation of this study is that it is possible that exact sectoral boundary locations could vary from mouse to mouse due to the rotation of mice on the stage. We could correct for rotation in follow-up images for a given mouse using the method described above, but this adjustment is less reliable across mice. For this reason, we chose not to assess clock hour measurements and to include only global and quadrant thicknesses in the analysis. Global measurements would not be affected by this limitation since all measurements within the band are compared.

We observed that more sectors from nerve-crushed eyes had to be excluded due to poor image quality than from control eyes. The media opacities leading to poor image quality were often due to corneal opacities, suggesting that eyes that received the nerve crush injury were more sensitive to damage from the cover slip used to focus on the retina. This may be due to corneal dehydration caused by the extended time of recovery from anesthesia after surgery, or

because the optic nerve crush surgery affects the conjunctiva, inhibiting proper hydration and tear film coverage.

We observed a slight linear increase in retinal thickness in control eyes over the course of this experiment. The significant positive quadratic term in the nerve crush eyes indicates that there was a rebound in thickness in those eyes as well. Previous studies have shown that the mouse eye^{113, 114} and retina¹¹⁵ are still growing through at least 15 weeks after birth. The follow-up period in our study lasted to an age of 15 weeks, which may explain the increase in retinal thickness in control eyes and the rebound in thickness in nerve-crushed eyes. The rebound in TRT in nerve-crushed eyes may also be due to retinal response to inflammation, such as gliosis. Another potential explanation for the gradual thickening might be related to scan quality. OCT studies in humans demonstrated that an increase in signal quality leads to an increase in thickness measurements.¹¹⁶⁻¹¹⁸ However, image quality was included as a covariate in our mixed effects model and did not have a statistically significant effect. Nevertheless, it should be noted that our quality criteria excluded images that were of poor quality, which might explain the discrepancy between our findings and those reported previously.

We did not include the contralateral eyes of the nerve-crushed mice as a control in this experiment, as there is evidence that there may be change occurring in those eyes.¹¹⁹⁻¹²¹ Future studies measuring retinal thickness in the contralateral eyes are required in order to determine whether they undergo structural changes that are detectable with OCT.

In summary, we demonstrated the ability of OCT to detect retinal thinning *in-vivo* following nerve crush. Using OCT to monitor retinal thickness in the mouse optic nerve crush model may be valuable for evaluating the pathophysiology of disease as well as testing the efficacy of treatment, since the same animals can be followed over time.

2.3 SUMMARY AND DISCUSSION: MOUSE IMAGING WITH OCT

The noninvasive nature of image acquisition together with the commercialization of systems optimized for laboratory use has resulted in a recent increase in the number of animal studies using OCT. Two- and three-dimensional scanning with OCT is appealing because the same animals can be followed over time, *in-vivo*, making longitudinal studies of ocular structures possible without the need to sacrifice animals at various time points and obtain histological sections. Not only does this reduce the number of animals required for experiments, but is superior to cross-sectional experiments which require different animals for different time points.

Ultimately, longitudinal OCT animal studies may help evaluate the efficacy of pharmacological agents, stem cell therapies, surgical intervention, and retinal prosthetics while reducing the required number of animals. OCT has the potential to provide a better understanding of disease development and progression in transgenic and other models of disease, which may eventually translate to improved clinical assessment and understanding of disease.

3.0 GOLD NANOROD PREPARATION

There are several published approaches for GNR fabrication, including wet chemical,¹²² electrochemical,¹²³ or photochemical¹²⁴ synthesis. The wet chemical synthesis approach utilizes a surfactant as a scaffold for growing rods from spherical colloidal gold seed particles. A colloidal gold spherical seed solution is added to a surfactant-based growth solution, and growth of the colloidal particles occurs along a single axis, forming the longitudinal dimension of the rod. This approach is appealing because it is easy to monitor growth of the particles by observing the color and measuring the UV-Vis-NIR spectrum of the growth solution as it reacts with the seed solution.

3.1 PREPARATION OF GOLD NANORODS RESONANT AT ~850 NANOMETERS

As described in Section 1.4, gold nanoparticles are an appealing candidate for optical imaging contrast enhancement not only because gold is mostly an inert immunologic compound, but also because gold exhibits the SPR phenomenon, which may boost backscattered signal intensity. Since the physical size or aspect ratio can influence the resonant frequency of nanoparticles, changing these parameters allows for tuning of the SPR to wavelengths of interest. SPR is observed in gold at NIR wavelengths,^{20, 21, 58, 60, 125, 126} and gold nanoparticles are thus potentially applicable to ocular OCT imaging at 840-860 nm.

GNRs can be reliably synthesized with dimensions on the order of 20-80 nm, making them especially useful for biological applications. The goal of this study was to fabricate scattering GNRs that could enhance reflectivity within a spectral-domain ocular OCT system.

3.1.1 Seed-mediated, Surfactant Directed Synthesis

Gold nanorods with an aspect ratio of approximately 4 (~40 nm x 10 nm) were prepared using a well-established seed-mediated, surfactant directed wet chemical synthesis¹²² with a slight modification to facilitate the growth of longer GNRs that resonate at longer wavelengths (Figure 13). The modification steps taken to optimize this protocol are described in Appendix A.

A seed solution of spherical colloidal gold particles was prepared by mixing hexadecyltrimethylammoniumbromide (CTAB; 5ml, 0.20M) with HAuCl_4 (5ml, 0.00050M), followed by the addition of ice-cold NaBH_4 (600 μl , 0.010M). A separate growth solution was prepared by adding AgNO_3 (9ml, 0.0040M) to CTAB (150ml, 0.20M), followed by HAuCl_4 (150ml, 0.0010M). At this point, a small amount of HCl (225 μl , 12M) was added to lower the pH of the growth solution, followed by the addition of ascorbic acid (2.1ml, 0.0788M). After the seed and growth solutions were prepared, 360 μl of the brown seed solution was added to the colorless growth solution. The growth solution was allowed to sit at 25 °C for 45 min, until the color of the solution turned purple-red.

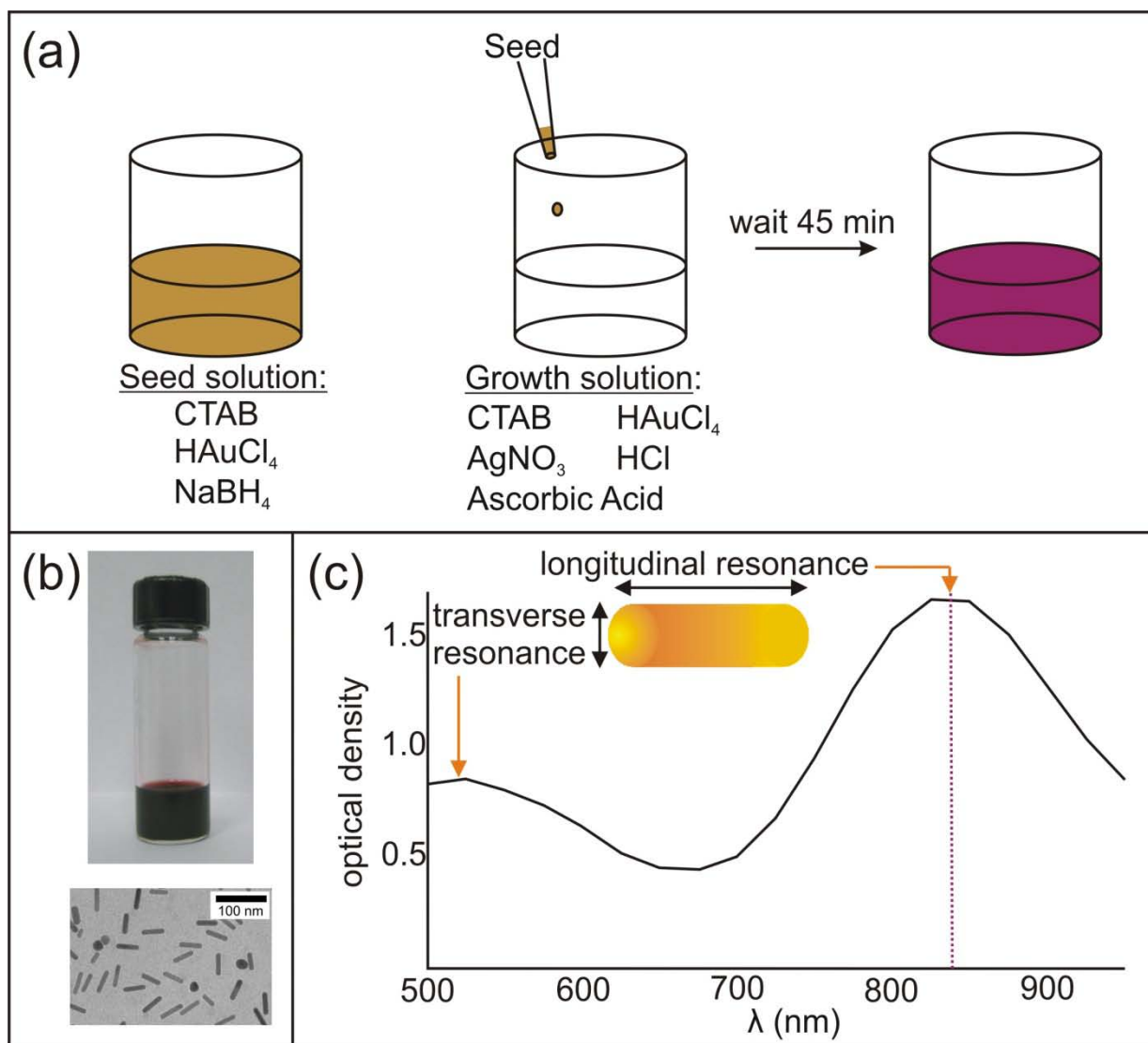


Figure 13. (a) Seed-mediated, surfactant directed synthesis preparation of gold nanorods (GNR). (b) Top: Photograph of GNR solution after concentrating and removing excess CTAB; Bottom: electron micrograph of PAA-coated GNRs (c) Absorbance spectrum of PAA-coated GNRs, with resonance peaks at $\lambda = 530$ nm and $\lambda = 835$ nm

After particle centrifugation (4100 RPM) to remove as much positively-charged CTAB as possible, a layer of negatively-charged polyacrylic acid (PAA) was adsorbed onto the surface of the GNRs according to the protocol described by Kim et al¹²⁷ to preclude clustering of particles in solution and to provide a shield from any CTAB that remained on the surface of the

particles after centrifugation, as CTAB is known to be cytotoxic. After the addition of PAA, the concentration of gold in the solution was approximately 51mg/ml. A schematic representation of the PAA-GNRs can be seen in Figure 14. Figure 15 shows OCT images of GNRs in solution. The GNR solution shows an increase in intensity as compared to PBS.

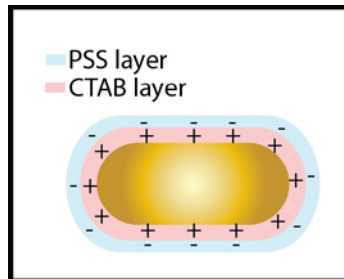


Figure 14. GNRs were prepared in a solution with a potentially cytotoxic, positively-charged surfactant (CTAB), so a negatively-charged PAA coating is used to neutralize and shield

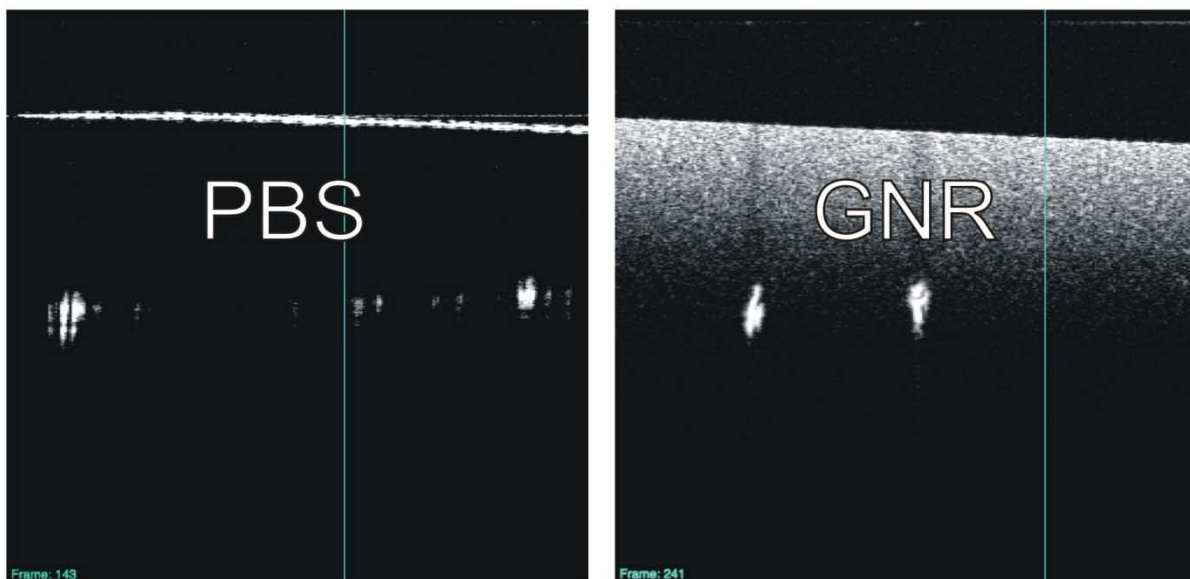


Figure 15. OCT image of phosphate buffered saline (PBS; sham) and gold nanorod (GNR) solution. Enhanced scattering can be observed in the GNR solution (250 A-scans; 2.5 mm).

3.2 CHARACTERIZATION OF ANTIBODY-CONJUGATED GOLD NANORODS

Antibody-conjugated gold nanorods (Ab-GNRs) have the potential to be used for specifically targeting or treating tissue using optical imaging techniques.^{22, 66} While methods for conjugation have been reported,¹²⁸ there is a need to characterize the bioconjugation for preclinical studies such that an optimal concentration – maximizing the number of particles that bind while minimizing the dosage of particles and excess antibody – can be established.

Typically, researchers have assessed the level of antibody conjugation by measuring surface charge (zeta-potential) of a solution of particles.¹²⁹ However, zeta-potential is based on all components of the gold surface, which also consists of positively and negatively charged polymers present to stabilize the particles. Moreover, zeta-potential does not indicate whether antibody-conjugated nanoparticles are sticking to structures of interest. Other methods, such as enzyme-linked immuno sorbant assays (ELISA) have been reported,¹³⁰ but can only indicate the presence or absence of the antibody and provide no information on whether the antibody-conjugated particles are functional. In addition, ELISA protocols do not indicate whether there are excess antibodies in the solution, so there is potential for false-positive results.

Immunogold staining is a technique developed for transmission electron microscopy (TEM) by Faulk and Taylor in 1971.¹³¹ In this technique, colloidal gold particles attached to secondary antibodies are used to indicate the presence of a primary antibody. Gold has a high density of electrons and thus shows up clearly in TEM images, and secondary antibodies are able to bind to primary antibodies. TEM has been used to directly visualize that nanoparticles were successfully bioconjugated.^{130, 132} A limitation of this approach, however, is that it only indicates whether the nanoparticles are functionalized and not whether they are capable of functionally binding.

Flow cytometry may offer a solution to this problem. This technique allows for the analysis of cell populations with respect to their size and granularity (Figure 16). Individual cells pass through a laser beam in a hydrodynamically focused stream of fluid. The amount of light that is projected in line with the beam is proportional to the size of the cell, while the light scattered perpendicularly to the beam indicates the relative granularity, internal complexity and / or roughness of the cell membrane. In addition, cells can be labeled with fluorescent markers (eg, antibodies conjugated with fluorescent labels), to identify subpopulations of cells within a sample or to look for the presence of specific markers.

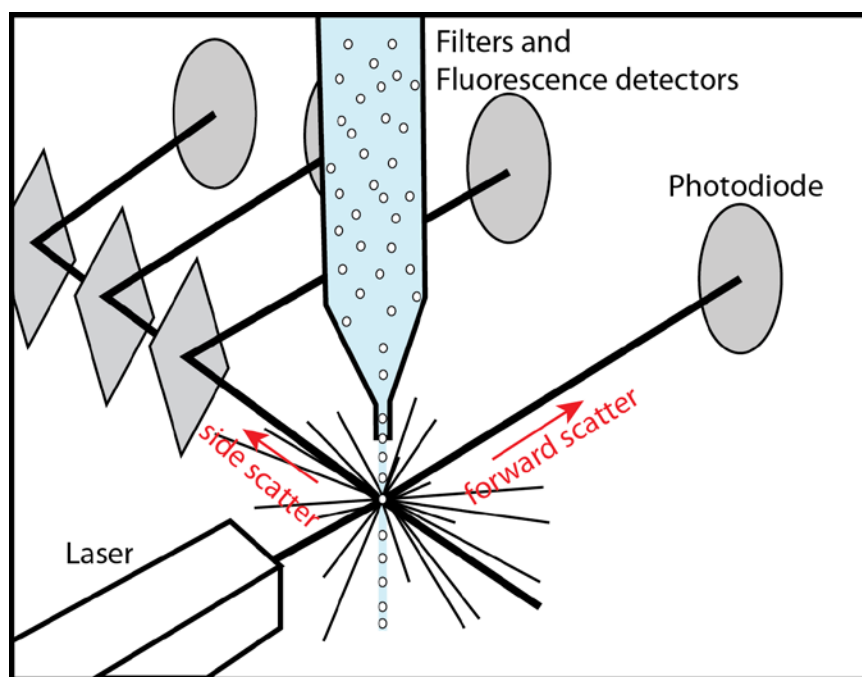


Figure 16. Schematic representation of flow cytometer. Incident laser light is scattered upon reaching an individual cell; forward and side scattered light is collected via filters and photodetectors.

The goal of this study was to develop a protocol for characterizing the success of antibody conjugation to GNRs using flow cytometry. CD90 (Thy1) is a protein expressed on the surface of retinal ganglion cells¹³³ and T-cells.¹³⁴ Anti-CD90.2 antibody-coated GNRs (Ab-GNRs),

therefore, may allow for specific targeting of retinal ganglion cells and T-cells. We hypothesized that antibody-coated (α -CD90.2) GNRs (primary antibody) would stick to CD90.2+ (Thy 1.2+) tumor cells, and that a fluorescently labeled secondary antibody could be used to detect the presence of the primary antibody bound to tumor cells using flow cytometry.

3.2.1 Methods

Gold Nanorods

The nanoparticles used in this experiment were obtained from Nanorods, Inc (Germantown, MD), and were coated with either α -CD90.2 (Thy1.2) antibodies (Ab-GNR) or polystyrene sulfate (PSS-GNR). The GNR solutions had an optical density (OD) of \sim 50. The GNRs were grown using a wet chemical, surfactant-directed synthesis similar to what is described above in Section 3.1.1. To conjugate the antibodies and form Ab-GNRs, Nanorods, Inc followed a protocol described by Huang et al.¹²⁸ Briefly, excess CTAB was removed from bare GNRs by centrifugation. Next, the positively charged GNRs were exposed to negatively charged poly(styrenesulfonate) (PSS, MW = 18,000, Polysciences, Inc) polyelectrolyte solutions. Excess PSS was removed by centrifuging and the GNR pellet was resuspended in N-(2-hydroxyethyl)piperazine-N'-2-ethanesulfonic acid (HEPES) buffer. PSS-GNRs were then incubated for 20 minutes with α -CD90.2 antibodies diluted in HEPES buffer, and centrifuged and resuspended in PBS.

Immunogold Transmission Electron Microscopy Assay

We used TEM to directly visualize Ab-GNRs with a secondary antibody (2^o Ab) label that was conjugated to 12 nm colloidal gold particles. This was done by incubating 5 μ l Ab-GNR

(or 5 μ l PSS-GNR) in 25 μ l bovine serum albumin (BSA) on a mesh formvar-coated copper grid for 4 min. Grids were then washed with BSA followed by 40 min incubation with 12 nm colloidal gold anti-Rat immunoglobulin 2^o Ab (AffiniPure Goat α RatIgG; Jackson Immuno Research). Next, a series of washes in BSA and PBS was performed to remove excess 2^o Ab, and the grid was fixed using 2.5 % glutaraldehyde and rinsed with PBS. After drying, Ab-GNRs and PSS-GNRs were examined directly using a JEOL JEM 1210 transmission electron microscope (Peabody, MA).

GNR Cell Staining Assay for Flow Cytometry

Mouse lymphoma cells (EL-4), which express CD90.2 (Thy1.2), were used in this experiment, which is summarized in Figure 17. Approximately 2×10^5 tumor cells were placed in each of seven wells in a 96 well plate and stained with either 10 μ l Ab-GNR solution or 10 μ l supernatant from the Ab-GNR solution. We assayed the supernatant from the Ab-GNR solution to observe whether there were free antibodies present in the Ab-GNR solution, and washed the Ab-GNRs twice, assaying both washes and supernatants, to look for a titration effect. The supernatant from the Ab-GNR solution and washes were obtained by centrifuging 50 μ l Ab-GNR solution (or washes) for 10-15 min at 10,000 RPM in a microcentrifuge. Washes consisted of 1.5 ml PBS (first wash) or 0.5 ml PBS (second wash); a smaller volume was used for the second wash to avoid removing too much of the PSS-coating, as this would induce clustering of GNRs.

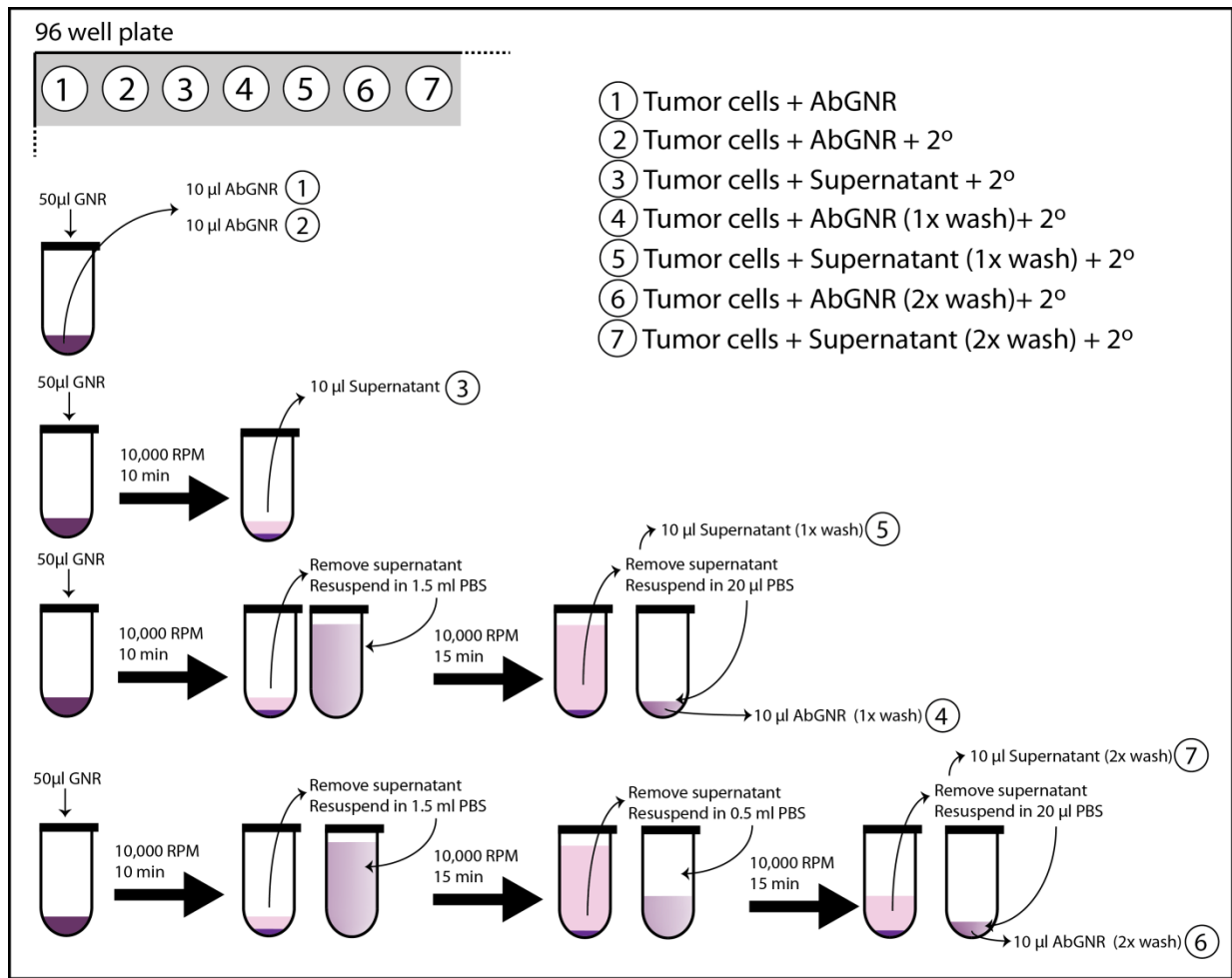


Figure 17. Summary of methodology for flow cytometry assay of EL-4 tumor cells (Thy1.2+), using antibody-coated (α CD90.2/ α Thy1.2) GNRs solutions washed up to two times and their corresponding supernatants.

The secondary antibody (2°) was APC-conjugated.

A fluorescently labeled secondary (2°) antibody (APC conjugated Goat α -Rat; BD Pharmingen) was used to indicate the presence of α -CD90.2. Our seven test conditions are summarized in Figure 17, upper right.

Each well was incubated with either Ab-GNR or the supernatant from Ab-GNR solution for 20 minutes and then washed twice with FACS buffer. For 2° Ab staining, solutions were stained for 15 minutes on ice in the dark and then washed twice with FACS buffer. Samples were

run on a FACSaria (BD Biosciences, San Jose, CA) flow cytometer and the percentage of cells emitting an APC signal was obtained using FlowJo software (Tree Star, Inc, Ashland, OR).

3.2.2 Results

TEM images show co-localization of Ab-GNRs with 2° Ab label that is not present in the PSS-GNR solution (Figure 18). Some background 12 nm 2° Ab labels were present, indicating there were excess antibodies in the solution that stuck to the TEM grid.

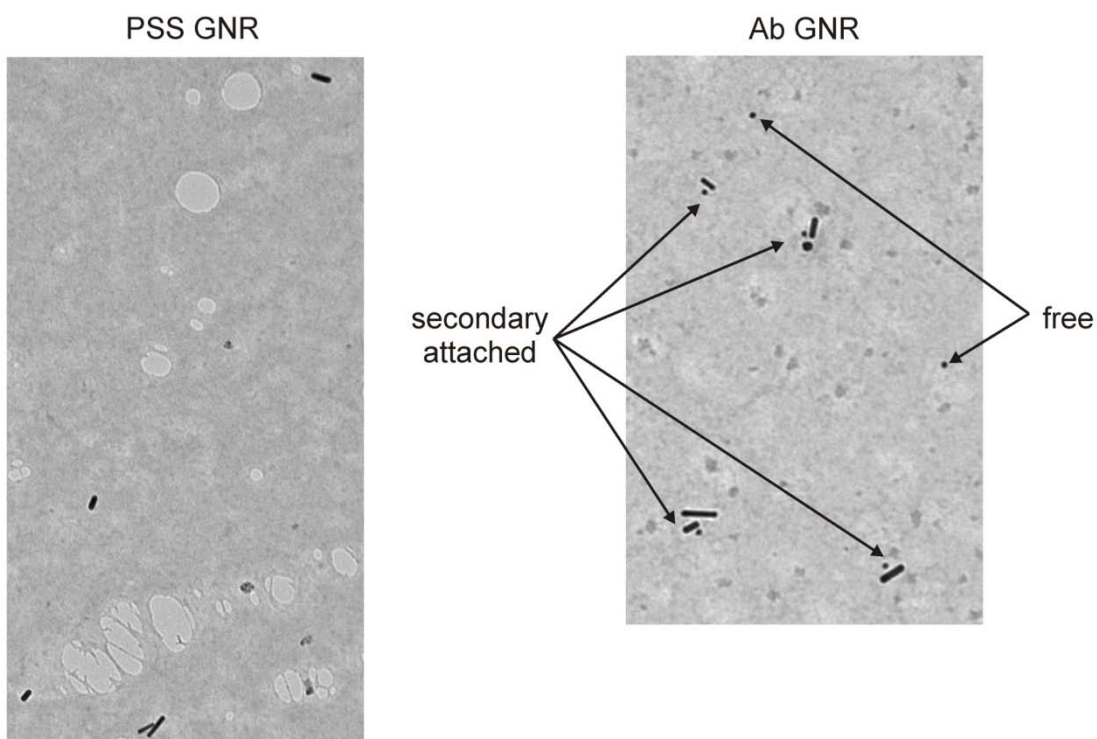


Figure 18. TEM showing labeling of Ab-GNRs with 2° Ab-conjugated 12 nm gold colloidal spheres. Most Ab-GNRs had a single 2° label, and some free 12 nm colloidal spheres indicate the presence of free antibodies. PSS-GNRs were not labeled.

While the majority of Ab-GNRs had one 2° Ab label per GNR, there were some particles that were not labeled, and some had up to three labels (Figure 19). A theoretical schematic representation of the gold nanorod, CTAB and PSS coatings, and antibodies is shown in Figure 19 for reference.

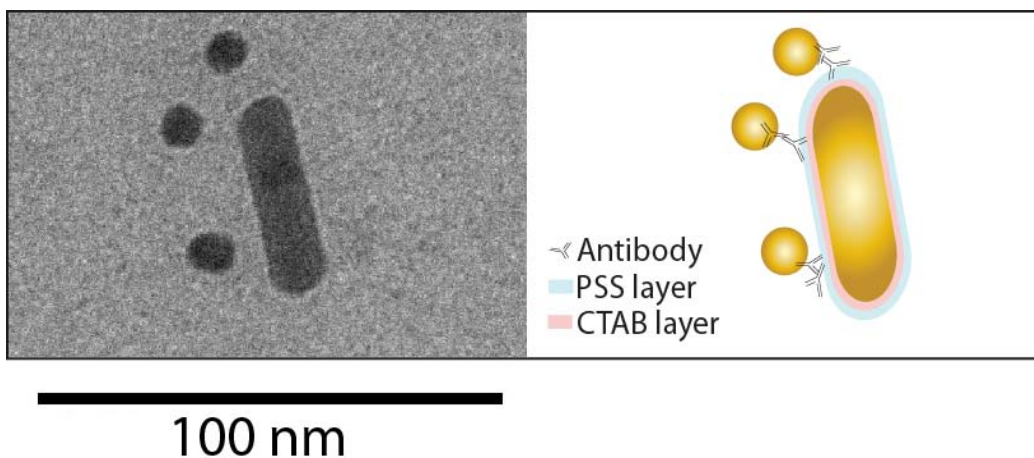


Figure 19. TEM showing a single Ab-GNR labeled with three colloidal gold 2° Ab. Each Ab-GNR is coated with PSS to shield from any CTAB layer leftover from production of the particles.

Results from the flow cytometry assay are seen in Figure 20. Ab-GNRs show a strong APC signal in the presence of the 2° Ab (92.70% of cells are labeled). However, there are excess antibodies in the solution, as indicated by the fluorescence signal in the supernatant (94.28% labeled). Washing the particles caused a substantial decrease in the amount of excess antibody in the supernatant (0.59%), bringing it back down to the level of the control solution (0.48%). However, many of the Ab-GNRs were lost in the process, and only 3.64% of cells were labeled after one wash. Washing a second time further reduced the fluorescence signal coming from the supernatant (0.22%) and caused even greater loss of Ab-GNRs (1.30%).

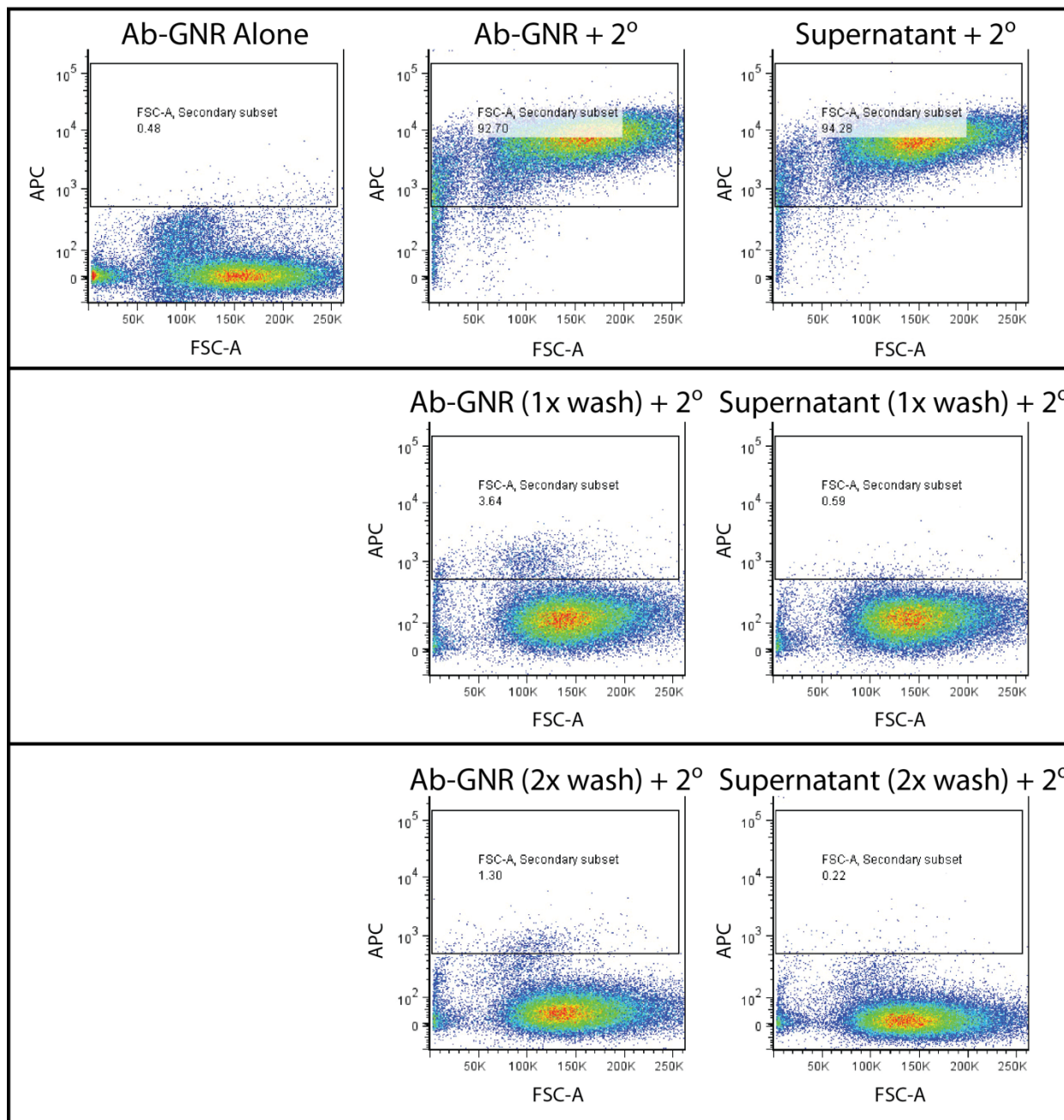


Figure 20. Results of flow cytometry assay. Top panel: stock Ab-GNRs and supernatant; Middle panel: Ab-GNR solution and supernatant after a single wash; Bottom panel: Ab-GNR solution and supernatant after two washes. The subset gate indicates the percentage APC-positive cells; more densely-packed cell populations are indicated by hotter colors.

3.2.3 Discussion

We developed a flow cytometry assay to determine whether Ab-GNRs are binding to cells of interest. This approach offers a novel way to evaluate antibody conjugation using isolated cell populations that express surface molecules of interest, and the assay is unique in its capacity to determine whether excess antibodies are present in GNR solutions.

We observed that excess antibodies were present in the supernatant of our Ab-GNR solutions, which were provided by a commercial vendor. This suggests that well-established antibody conjugation protocols may require the addition of fewer antibodies. It may also mean that antibodies are freed from GNRs during the centrifugation step, which could potentially make them less effective for tissue targeting.

Excess antibodies may pose a significant problem *in-vivo*, as they will compete for binding sites with Ab-GNRs. Hence, a larger dose of Ab-GNRs would be required to compete, and this could induce unwanted biological effects.

One limitation to this study is that Ab-GNRs are lost during centrifugation because they have a tendency to stick to containers they are centrifuged in. This is a common problem with Ab-GNRs, since washing to remove excess antibodies strips the GNRs of their polymer coatings allowing them to readily adhere to each other or to walls of the containers they are washed in.

Given that the number of wash cycles Ab-GNRs will survive is limited, our assay may be able to provide a method for checking Ab-GNR solutions prior to wash so that an optimal number of antibodies can be adsorbed to the surface while leaving few excess antibodies in solution.

3.3 SUMMARY AND DISCUSSION: GOLD NANORODS

The GNR synthesis approach together with the *in-vitro* flow cytometry-based Ab-GNR assay presented in this chapter provide fundamental resources for evaluating the success of cellular targeting using GNRs. The flow cytometry assay provides a readily accessible technique for identifying whether antibodies are conjugated to GNRs and are targeting structures of interest. This approach should be applicable to multiple combinations of Ab-GNRs and isolated cell populations of interest. It may assist with optimizing the administered dosage of GNRs such that the maximum number of nanoparticles can be applied with a minimum number of excess antibodies.

4.0 PRE-CLINICAL STUDIES: IN-VIVO AND BIOCOMPATIBILITY EXPERIMENTS

4.1 GOLD NANOROD INJECTIONS

Few studies evaluating gold nanoparticles in the eye have been conducted,¹³⁵⁻¹³⁷ and to our knowledge, none have observed the behavior of GNRs after introduction to the eye. As demonstrated in Figure 15, GNRs cause an increase in backscattered signal that can be detected by SD-OCT. Given their potential to target low-backscattering structures such as RGCs, the presence of GNRs at the level of RGCs may provide a way to distinguish them from surrounding tissue.

The goal of this study was to image GNRs in the eye *in-vivo* using a SD-OCT system, and to use SD-OCT and TEM imaging to document the distribution of particles in the posterior segment after injection.

4.1.1 Animals and Methodology

Healthy adult male C57Bl/6 mice (Jackson Laboratory, Bar Harbor, ME) were used in this study. Mice were maintained in the University of Pittsburgh Animal Facility with a 12-hour light/dark cycle and had free access to water and standard laboratory feed. This experiment met the approval of the University of Pittsburgh's Institutional Animal Care and Use Committee and adhered to the ARVO Statement for the Use of Animals in Ophthalmic and Vision Research.

Injection of GNRs

Animals were anesthetized with an intraperitoneal injection of ketamine (Ketaject, Phoenix Pharmaceuticals, St. Joseph, MI; 80 mg/kg) and xylazine (Xyla-ject, Phoenix Pharmaceuticals, St. Joseph, MI; 5 mg/kg) before the injection of GNR. The eye was proptosed with forceps and an incision was made at the limbus by the insertion of a 30-gauge needle. A 33-gauge hypodermic needle fitted on a Hamilton 700 series microsyringe (Hamilton Co, Reno, NV) was then inserted into the incision site. This was used to administer a 2 μ l intravitreal injection of either GNR (51mg/ml) or phosphate buffered saline (PBS; sham injection). The procedure was performed under a surgical microscope in one eye per animal.

OCT Imaging

Animals were anesthetized, as described above, in order to prevent large movements during OCT scanning. Tropicamide (1%; Falcon Pharmaceuticals, Fort Worth, TX) was applied topically to each eye for pupil dilation. Hydroxymethylcellulose ophthalmic demulcent solution (Goniosol 2.5%; Akon, Buffalo Grove, IL) was used to preserve corneal hydration and couple a thin glass cover slip to the cornea to neutralize corneal optical power and enable focusing of the OCT imaging beam on the retina. Mice were secured on a custom stage, which allowed for free rotation so images of specific landmarks, such as the optic nerve head, could be acquired. Scans of the retina, vitreous and posterior lens were acquired (1.5 x 1.5 x 2 mm scan at surface of cover slip, 250x250x1024 pixels, four consecutively-repeated axial scans at each sampling location; Bioptigen, Research Triangle Park, NC). Baseline images were acquired prior to intravitreal

injections. Follow-up images were acquired 24 hours after the injection using identical scan settings.

Transmission Electron Microscopy

At the end of this experiment, the mice were sacrificed by inhalation of CO₂ and eyes enucleated and immersion fixed in 2.5% glutaraldehyde overnight at 4°C for transmission electron microscopy (TEM). Following fixation, the posterior lens and vitreous were dissected out and this tissue was washed 3 times in PBS, then post-fixed in aqueous 1% OsO₄, 1% K₃Fe(CN)₆ for 1 hour. Following 3 PBS washes, the tissue was dehydrated through a graded series of 30-100% ethanol, 100% propylene oxide then infiltrated in 1:1 mixture of propylene oxide:Polybed 812 epoxy resin (Polysciences, Warrington, PA) for 1 hr. After several changes of 100% resin over 24 hrs, the pellet was embedded in molds, and cured at 37°C overnight. This was followed by an additional hardening at 65°C for two more days. Ultrathin (60 nm) sections of the vitreous and lens were collected on copper grids, stained with 2% uranyl acetate in 50% methanol for 10 minutes, followed by 1% lead citrate for 7 min. Sections were imaged using a JEOL JEM 1210 transmission electron microscope (Peabody, MA) at 80 kV fitted with a side-mount AMT 2k digital camera (Advanced Microscopy Techniques, Danvers, MA).

4.1.2 Results

A total of 12 mice, aged 19.4 ± 6.8 weeks, were used in this experiment: four eyes from four mice received a sham (PBS) injection and eight eyes from eight mice received a GNR injection. No systemic adverse effects were noted in any of the mice, however retinal edema was seen in

six eyes 1 day post-injection (1 sham, 5 GNR) and one eye showed a localized vitreous hemorrhage.

OCT imaging showed a slight change in intensity in sham-injected eyes, while the GNR-injected eyes showed a marked increase in OCT signal. Pre- and post-injection images from two mice are shown in Figure 21. The sham injection caused what appeared to be a mild inflammatory reaction as evident by the appearance of small, round focal areas of scattering in the vitreous. GNRs appear to be decorating the vitreous, anterior hyaloid membrane and posterior surface of the lens with marked enhancement of the OCT signal. Signal enhancement in the vitreous and near the posterior capsule of the lens was evident when compared to the pre-injection image and to the sham injection. The strong signal from the vitreous caused attenuation of the retinal signal. A similar vitreous signal enhancement was observed in all GNR-injected eyes. An additional mouse was imaged out to 30 days post-injection, and there remained a strong backscattering response from the vitreous (Figure 22). TEM confirmed the presence of GNRs in the vitreous and lining the posterior capsule of the lens (Figure 23). Very few GNRs were seen in the retina, and were concentrated in microglial cells (Figure 24).

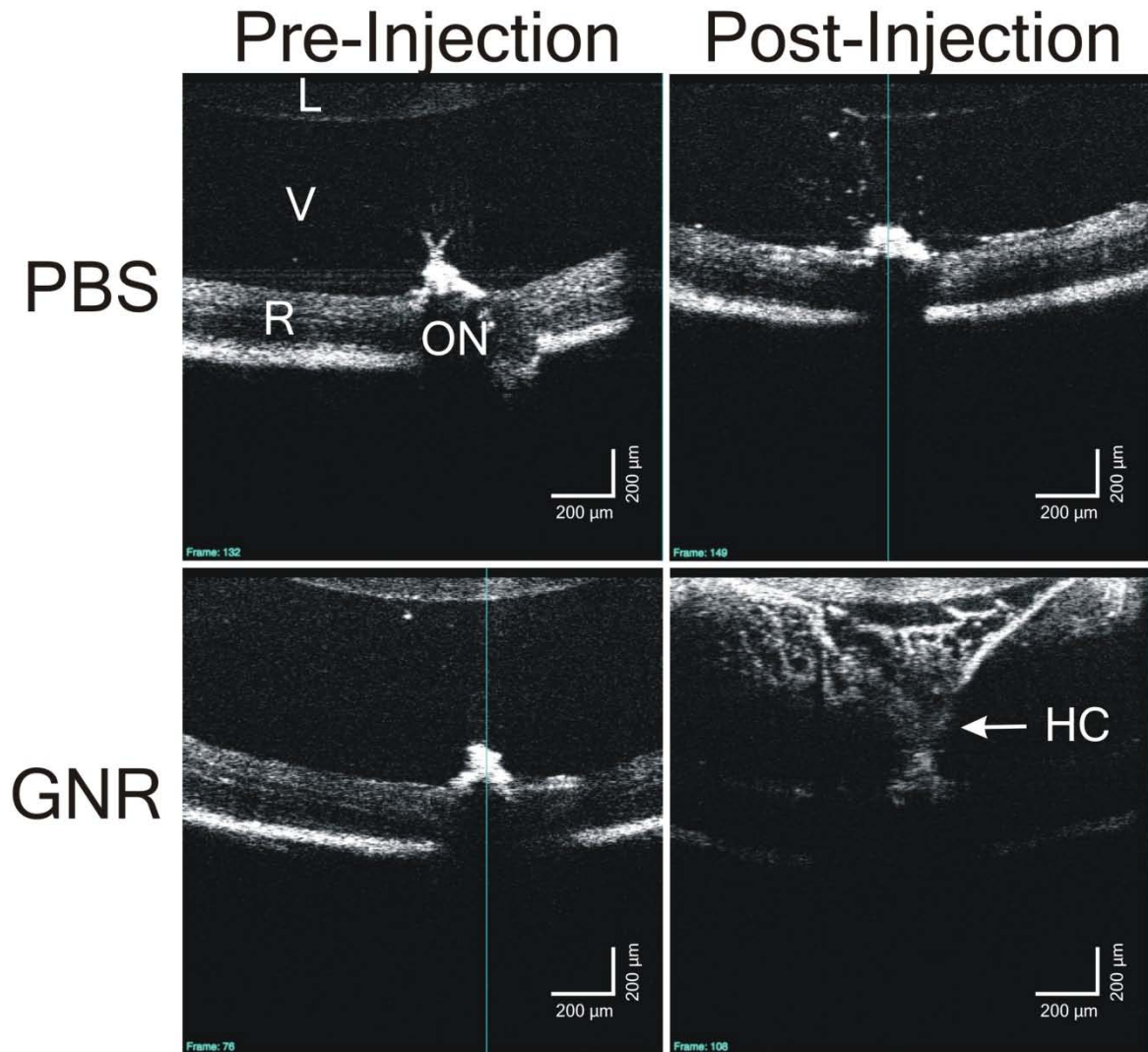


Figure 21. Baseline and follow-up (1 day after injection) images from mice injected with sham and gold nanorods (GNR). Marked signal enhancement is observed in the GNR injected vitreous as compared to both pre-injection and the sham injection images. The retinal signal is attenuated in the GNR-injected eye due to a shadowing effect caused by the strong backscattering signal from the vitreous. Abbreviations: L – Lens, V – Vitreous, R – Retina, ON – Optic Nerve, HC – Hyaloid Canal.

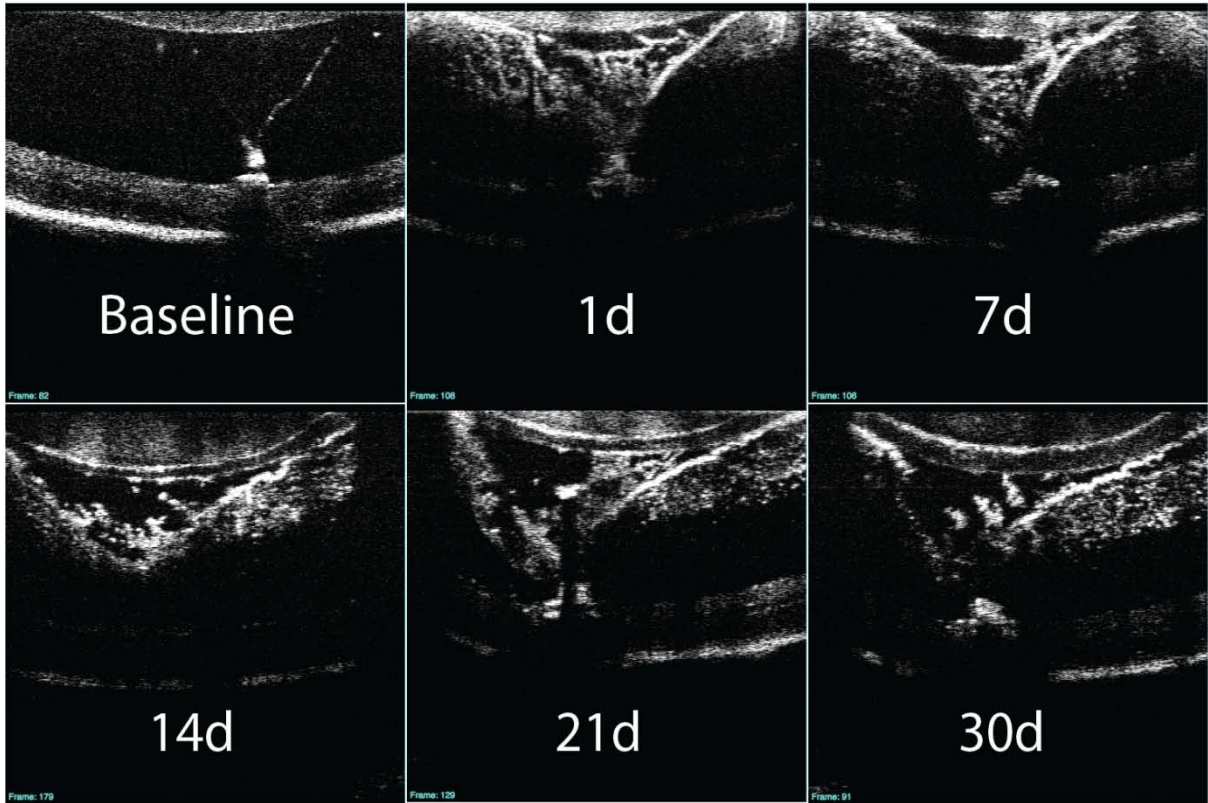


Figure 22. Baseline and follow-up (up to 30 days after injection) images from mice injected with gold nanorods (GNR).

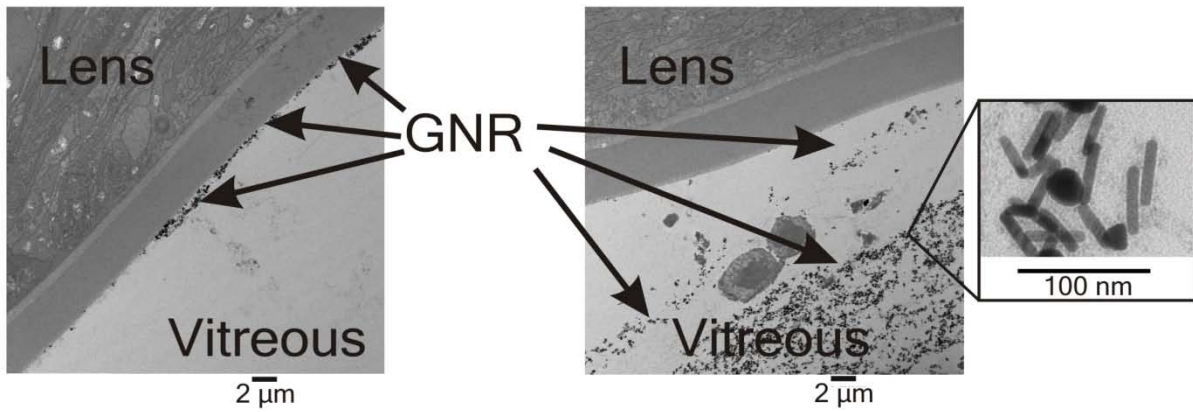


Figure 23. Transmission electron micrograph showing GNR in vitreous and lining the lens capsule after injection.

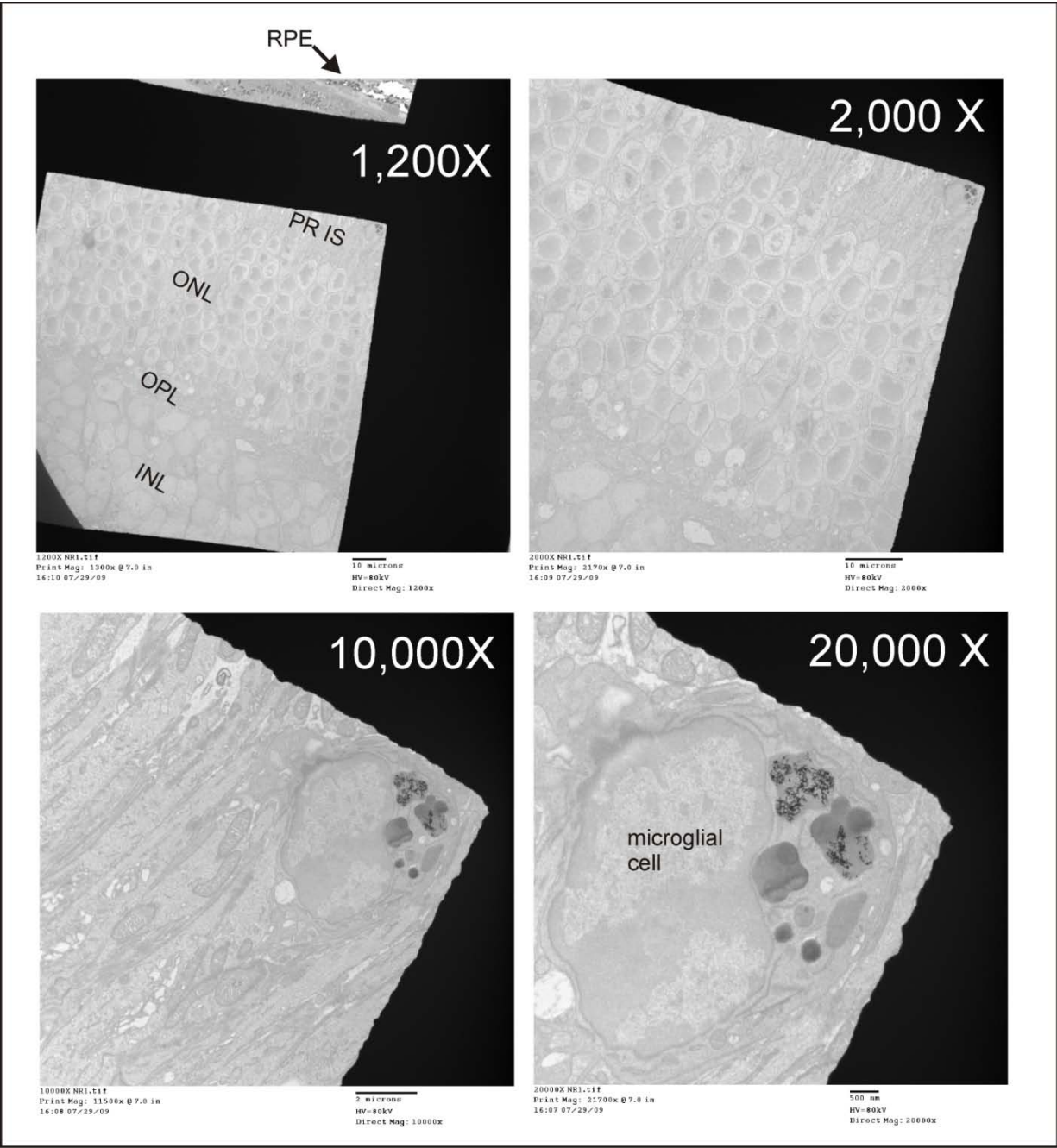


Figure 24. Transmission electron micrographs showing GNRs in microglia in the retina after injection. RPE – retinal pigment epithelium, PR IS – photoreceptor inner segment, ONL – outer nuclear layer, OPL – outer plexiform layer, INL – inner nuclear layer

4.1.3 Injection Summary and Discussion

In this study, we used GNRs developed in Section 3.1 and observed that, when injected into mouse eyes, the GNRs caused a substantial increase in OCT signal in the vitreous for up to 30 days after injection. While previous studies have suggested that gold nanoparticles can enhance backscattering *in-vitro*,^{56, 57, 59, 61, 63} and demonstrated *in-vivo* contrast-enhancing capabilities of nanoshells^{65, 138} and gold nanoparticles⁶⁴ in the skin and mouth, respectively, to our knowledge this is the first study showing the contrast-enhancing ability of GNRs in the eye *in-vivo*.

This experiment qualitatively compared cross-sectional scans from GNR and PBS injected eyes. We did not compare cross-sectional scans or individual axial scans because SD-OCT exhibits a nonlinear intensity drop-off with depth.⁴ The ocular structures we imaged (lens, vitreous and retina) were not aligned in the axial direction pre- and post-injection since the volume of the vitreous change, and thus quantitative intra-scan comparisons of backscattered intensity values would not be appropriate. In addition, returning precisely to one scanning location before and after GNR injection is difficult since landmarks such as blood vessels may be obscured by GNRs in the vitreous and the position of the mouse may be slightly different from scan to scan due to the angle of rotation of the eye with respect to the OCT beam.

As shown in the TEM image of Figure 13b, our method of GNR synthesis produced a distribution of sizes. While the majority of the solution consisted of GNRs, some spherical artifacts were present in the injected solution. Although we observed a substantial increase in signal in the vitreous of mice in this experiment, it may be possible to use a lower-dose injection of more uniformly-shaped GNRs to cause a similar increase in signal.

While the presence of GNRs in the vitreous was confirmed using TEM, it is also possible that inflammatory cells contributed to some of the increase in vitreous reflectance as we

observed what appeared to be a small inflammatory reaction with the sham injection that caused a mild signal increase. Although the whole eye remained structurally intact after the injection of GNRs, and all animals survived the injection, future studies are necessary to determine whether there is cytotoxicity or if any functional deficits develop related to the GNRs. The increased number of mice with retinal edema with the GNR injection as compared to sham injection may indicate inflammation or toxicity or may be the result of complications from the injection. An investigation into whether an inflammatory response is present after injection is reported in Section 4.2. In summary, we present a novel *in-vivo* signal-enhancing method using GNRs to highlight vitreous structures in OCT images.

4.2 BIOCOMPATIBILITY EXPERIMENTS

Nanoparticles are receiving increased attention in ophthalmology for their potential as molecular contrast and therapeutic agents for optical imaging and vehicles for drug delivery.¹³⁹ Metallic nanoparticles, such as gold nanoparticles and gold nanorods (GNRs) may be particularly useful for optical imaging given their localized surface plasmon response (SPR), which facilitates strong scattering and absorption of light.^{20, 21}

Very little is known about the behavior of gold nanoparticles in the eye. One group injected gold nanoparticles intravenously into mice and showed that 20 nm diameter colloidal gold nanoparticles could pass through the blood retina barrier and enter the retina while 100 nm particles could not.¹³⁵ They found that the presence of the 20 nm particles did not cause apoptosis in retinal neurons, endothelial cells or glial cells. A second group investigated the use of antibody-conjugated gold nanoparticles injected subretinally and showed they were still

present in the retina and retinal pigment epithelium at 3 months post-injection.¹³⁷ A third study used gold nanoparticles injected into the vitreous of Dutch-belted rabbits and looked by light microscopy.¹³⁶ They observed cellular atrophy within the retina but did not observe inflammation 15 and 29 days after the injection. However, since they did not look for inflammation at earlier time points it is unclear whether the nanoparticles caused atrophy.

One critical step in establishing the utility of gold nanoparticles in general and GNRs in particular is the assessment of biocompatibility after introduction into the eye. Studies involving gold nanoparticles are inconsistent with respect to establishing a clear understanding of their biocompatibility. Some gold nanoparticles have been shown to be nontoxic,^{71, 140} while others have been shown to be toxic depending on size, shape or surface chemical characteristics.¹⁴¹⁻¹⁴⁴

There is evidence that the presence of gold nanoparticles can elicit an undesired immune response.⁵¹ GNRs may be taken up by macrophages with higher efficiency than spherical gold nanoparticles depending on their surface chemistry.¹⁴⁵ This may be due to a similarity in shape to rod-like bacteria, which can be internalized in nonphagocytic cells.¹⁴⁶ While many reported toxicology studies have been performed *in-vitro*, there is preliminary *in-vivo* evidence showing gold nanoparticles can cause inflammation.¹⁴⁷

To our knowledge, there have not been any reports on the biocompatibility of GNRs introduced into the eye. As a first step to determining whether GNRs may be able to be used in the eye, it is important to characterize the immunogenic response. The goal of this study, therefore, was to determine whether GNRs elicit an inflammatory response after injection into the vitreous of mice.

4.2.1 Methodology

Healthy adult male C57Bl/6 mice (Jackson Laboratory, Bar Harbor, ME) were used in this study. Mice were maintained in the University of Pittsburgh Animal Facility with a 12-hour light/dark cycle and free access to water and standard laboratory feed.

Gold Nanorods

The nanoparticles used in this experiment were obtained from Nanorods, Inc (Germantown, MD), and were either coated with antibodies (α -CD90.2) or polystyrene sulfate (PSS) using a well-established method for antibody conjugation published by Huang et al¹²⁸ and described in detail in Section 3.3.1. CD90 is a molecule expressed on the surface of retinal ganglion cells and T-cells, and PSS is a detergent used to detoxify the GNRs by displacing cetyl trimethylammonium bromide (CTAB). CTAB is a cytotoxic surfactant that is present during the seed-mediated, surfactant directed synthesis of the GNRs.¹²² PSS also serves to prevent clumping of nanorods in solution. Both the Ab-GNR and PSS-GNR solutions had an optical density (OD) of 50.

Sterility Monitoring

Prior to injection of the GNRs, we ruled out the possibility of bacterial contamination of the GNR solutions by culturing a sample on standard Chocolate II Agar Medium with Hemoglobin and Isovitalex (BD Diagnostic Systems, Sparks, MD) by streaking 1 μ l using a calibrated loop. The agar plates were incubated at 36 °C under 6 % CO₂ at atmospheric conditions and monitored for 3 days for bacterial growth.

Injections

Animals were anesthetized with an intraperitoneal injection of ketamine (Ketaject, Phoenix Pharmaceuticals, St. Joseph, MI; 80 mg/kg) and xylazine (Xyla-ject, Phoenix Pharmaceuticals, St. Joseph, MI; 5 mg/kg) prior to the injection. The eye was proptosed using forceps and an incision was made at the limbus by the insertion of a 30-gauge needle. A 33-gauge hypodermic needle fitted on a Hamilton 700 series microsyringe (Hamilton Co, Reno, NV) was then inserted into the incision site to administer a 2 μ l intravitreal injection. The procedure was performed under a surgical microscope in both eyes per animal. There were four experimental groups included in this study, as summarized in Table 2.

Table 2. Experimental groups; OD – optical density, λ_{spr} – surface plasmon resonant wavelength

Group	Description of Injection
1	No injection
2	Phosphate buffered saline; Sham injection
3	Polystyrene sulfate conjugated gold nanorods; OD = 50, λ_{spr} = 850 nm
4	Antibody conjugated gold nanorods (α -CD90.1 antibodies); OD = 50, λ_{spr} = 857 nm

Transmission electron microscopy

A subset of mice was euthanized by inhalation of CO₂ at 24 hours post-injection. These mice received an injection in one eye, and only the test eye was processed for TEM. Eyes were enucleated and immersion fixed in 2.5% glutaraldehyde overnight at 4°C for TEM. Following fixation, the posterior lens and vitreous were dissected out and this tissue was washed and then post-fixed in aqueous 1% OsO₄, 1% K₃Fe(CN)₆. The tissue was dehydrated and then infiltrated in 1:1 mixture of propylene oxide:Polybed 812 epoxy resin (Polysciences, Warrington, PA). The pellet was embedded in molds and hardened and ultrathin (60 nm) sections of the vitreous and lens were collected on copper grids and stained. Sections were imaged using a JEOL JEM 1210

transmission electron microscope (Peabody, MA) at 80 kV fitted with a side-mount AMT 2k digital camera (Advanced Microscopy Techniques, Danvers, MA).

Collagenase digestion of eyes for flow cytometry

The remaining mice were euthanized by inhalation of CO₂ and their eyes enucleated and processed for flow cytometry. Each eye was immediately washed in PBS to remove any excess blood resulting from the enucleation, then transferred into a 2 ml collagenase IV digest solution consisting of 1 mg/ml collagenase IV (Sigma, St. Louis, MO) 0.25 mg/ml Deoxyribonuclease I (Sigma) and 1% fetal bovine serum (FBS; Atlanta Biologicals, Lawrenceville, GA) in RPMI 1640 media (Mediatech, Inc, Manassas, VA). Eyes were gently chopped with scissors to increase surface area for digestion, and placed in the collagenase IV digest solution for 1.5 hours, with the solution resuspended after 45 min to ensure a thorough digestion.

After digestion, each eye solution was filtered through a nylon screen (70 μm), washed with PBS and then resuspended in 400 μl FACS buffer (PBS + 1% FBS). One-quarter of each eye solution (100 μl) was added to an individual well of a 96 well plate and then samples were incubated with unconjugated anti-CD16/CD32 antibodies (BD Pharmingen, San Diego, CA) for 10 minutes on ice in the dark to block Fc receptors. Wells were then washed with FACS buffer, and stained with a mix of antibodies (Table 3) for 20 min on ice in the dark. Pooled eye samples spiked with Thy1.2+ E.G7-OVA tumor cells were stained individually with Thy1.2 FITC, Thy1.2 PE, CD45 PerCP, Thy1.2 APC, or CD11b Pac Blue as single color controls to set flow cytometry compensation.

Isotype controls were also set using this pooled sample by staining with CD45 PerCP, Rat IgG2_{ak} PE, CD11b Pacific Blue, Rat IgG2_{bk} FITC, Rat IgG2_{bk} APC. A pacific orange

viability probe was added along with CountBright Absolute Counting Beads (Invitrogen, Camarillo, CA) to determine the absolute number of cells of respective immune cell populations and analysis was performed using FlowJo software (Tree Star, Inc, Ashland, OR).

Table 3. Fluorescent antibodies used for flow cytometric staining

Antibody (Fluorescent Marker)	Target
α CD45 (PerCP)	Leukocytes
α Thy1.2 (PE)	T-cells, Neurons
α CD11b (Pacific Blue)	Myeloid cells
α GR-1 (FITC)	Neutrophils
α F4-80 (APC)	Macrophages
Aqua Viability (Pacific Orange)	Live/dead cell discrimination

Statistical Analysis

Generalized estimation equations were fitted to model the logarithm of cell counts for CD45+ leukocytes, Thy1.2+ T-cells, CD11b+ myeloid cells, CD11b+ F4/80+ GR-1- macrophages, and CD11b+ F4/80- GR-1+ neutrophils, taking into account clustering that occurred between eyes. This allowed us to compare control and GNR-injected eyes (Groups 1, 2, 3 and 4) to evaluate differences in inflammatory cell numbers between groups. An α -level of 0.05 was used as a cutoff for statistical significance.

4.2.2 Results

A total of 26 eyes (14 mice, age 127 days) were included in this experiment. Two mice (2 eyes) received an Ab-GNR injection and were processed for TEM. Of the remaining 12 mice, three (6 eyes) did not receive an injection, three (6 eyes) received PBS injections, three (6 eyes) PSS-GNR injections and three (6 eyes) Ab-GNR injections. One PSS-GNR injection had a technical failure (inability to locate the incision site for injection), and this eye was excluded from the

study. In total, 23 eyes were processed for flow cytometry to obtain cell counts 24 hours post-injection.

Representative TEM images from 24 hours post Ab-GNR injection are shown in Figure 25. After 24 hours, GNRs appear to be clustered extracellularly within strands of the vitreous, with many inflammatory cells in close proximity or surrounding and engulfing the nanoparticles. Some GNRs have been phagocytosed by these inflammatory cells.

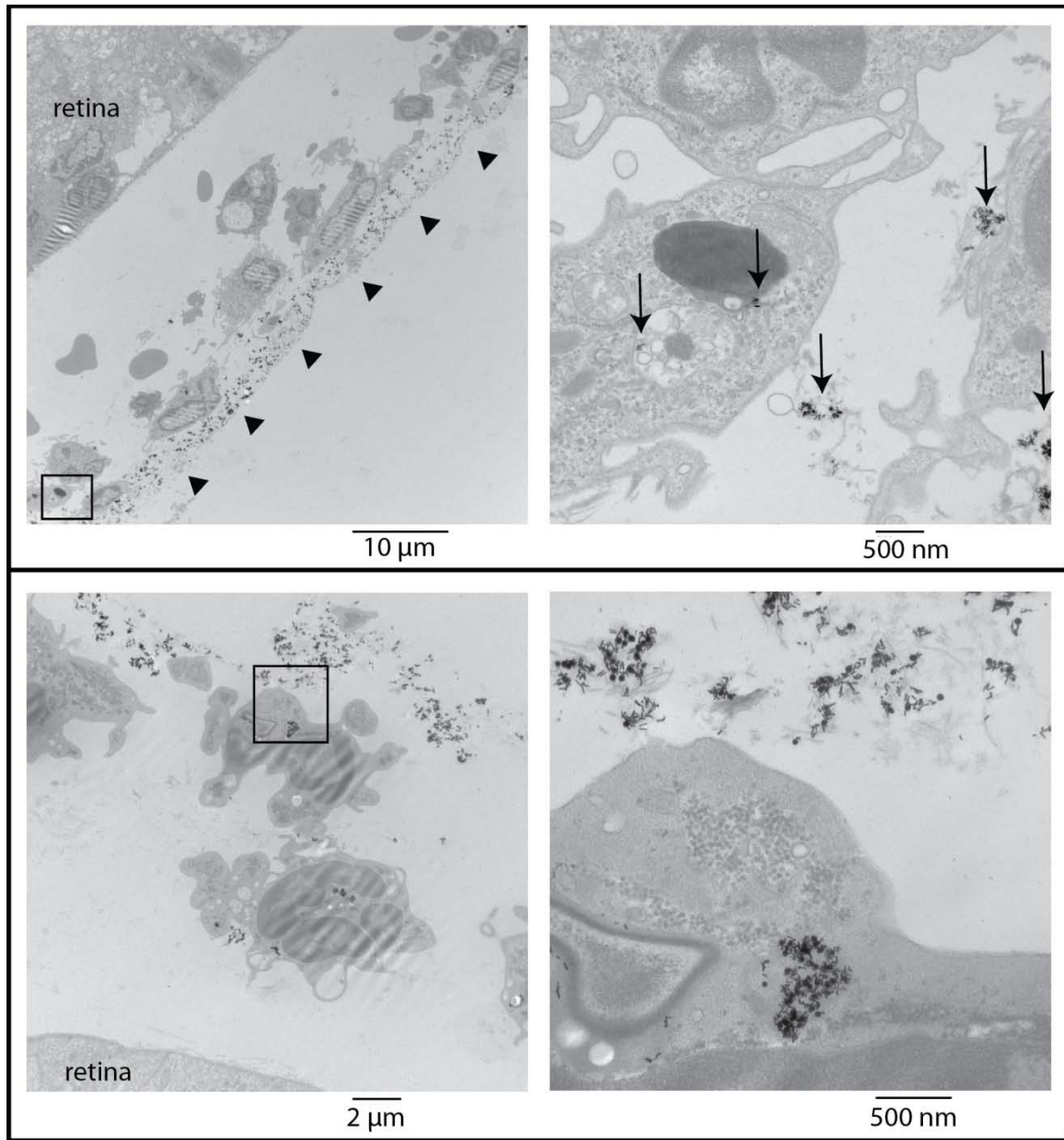


Figure 25. TEM images from two mice (top and bottom panels) 24 hours post GNR injection. (Top left) Arrowheads show a line of extracellular particles near inflammatory cells and (Top right) arrows show some free particles as well as some that have been internalized. (Bottom left) Extracellular and intracellular GNRs are evident when looking at magnified section (Bottom right). The rectangles indicate the location of higher magnification images.

Mean cell counts are shown in Figure 26 and Table 4. In eyes that received no injection or a PBS injection (Groups 1 and 2), there were no statistically significant differences for any cell count except for F4-80-/GR-1+ neutrophil cells. Group 4 was statistically significantly different from Group 1 for all cell types, and Group 3 was statistically significantly different from Group 1 for all cell types except Thy1.2+ T-cells. The groups receiving GNR injections (Groups 3 and 4) were not statistically significantly different from each other for any cell count, but were statistically significantly different from the PBS-injection group (Group 2) for all counts except Thy1.2+ T-cells, where Groups 2 and 3 were not statistically significantly different.

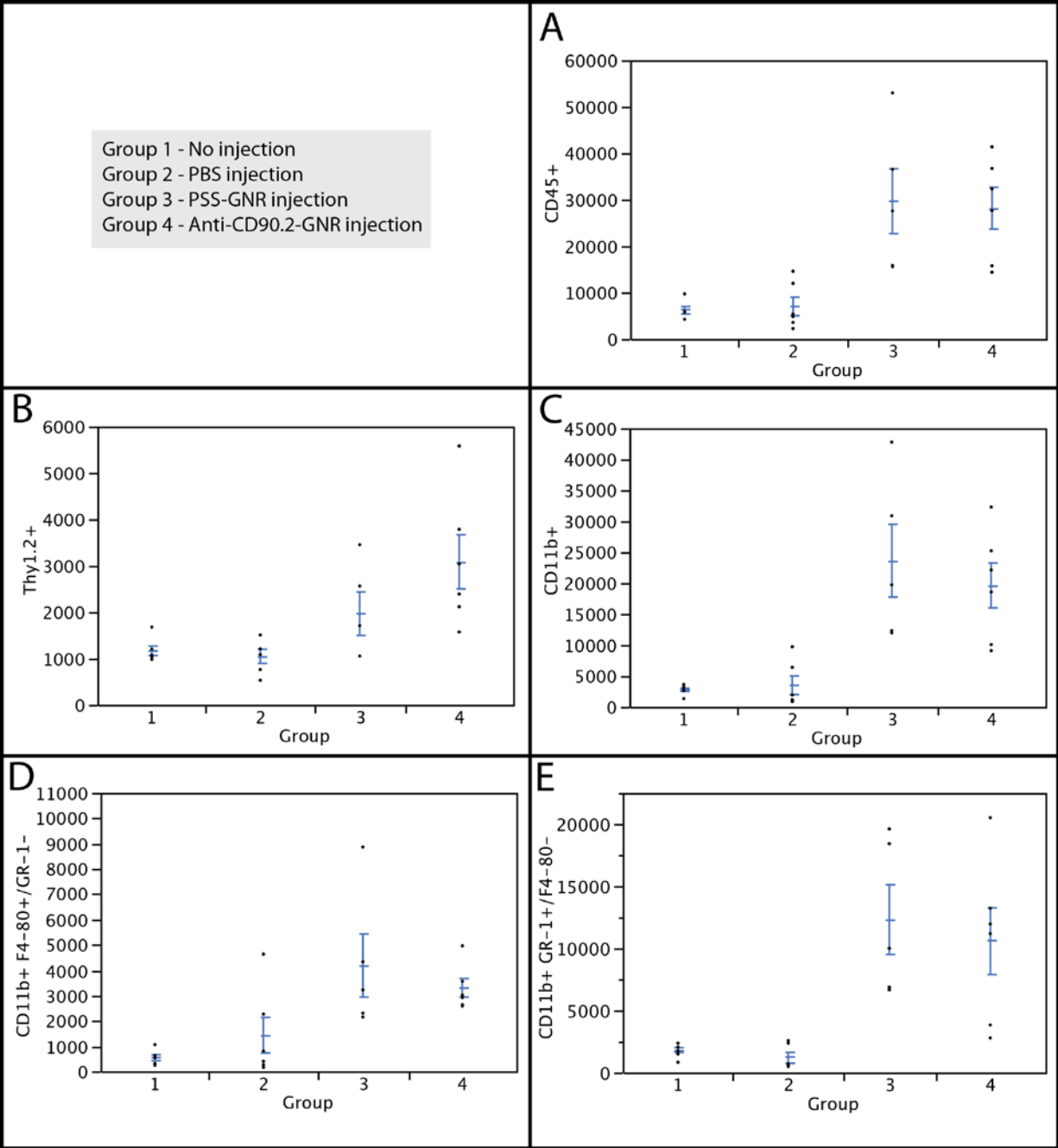


Figure 26. Flow cytometric analysis of collagenase-digested eyes after indicated treatments to determine the number of infiltrating CD45+ leukocytes (A.) that expressed Thy1.2 (B.), T cells, or CD11b (C.) myeloid cells. CD11b+ cells were further characterized for expression of F4/80 (D.) and GR-1 (E.) to identify F4/80+ GR-1- macrophages and F4/80- GR-1+ neutrophils.

Table 4. Expected cell counts and 95% confidence intervals from generalized estimation equation models of cell counts for (A) CD45+ leukocytes that expressed Thy1.2 (B), or CD11b (C), and CD11b+ cells that expressed F4/80 (D) and GR-1 (E). P-values for pairwise comparison of groups for a given cell type are indicated at right, with statistically significant differences indicated by *

(A) CD45					
Group	Expected Cell Count [95% CI]		Group 1	Group 2	Group 3
1	5983.2 [5654.6-6330.9]	Group 2	0.894		
2	5754.3 [3257.0-10166.6]	Group 3	<0.001*	<0.001*	
3	26545.4 [18469.1-38153.3]	Group 4	<0.001*	<0.001*	0.930
4	25986.6 [18934.3-35665.6]				

(B) Thy1.2					
Group	Expected Cell Count [95% CI]		Group 1	Group 2	Group 3
1	1149.4 [1021.8-1292.9]	Group 2	0.450		
2	993.9 [695.8-1419.7]	Group 3	0.110	0.071	
3	1758.2 [1060.7-2914.4]	Group 4	<0.001*	<0.001*	0.150
4	2828.7 [1877.7-4261.3]				

(C) CD11b					
Group	Expected Cell Count [95% CI]		Group 1	Group 2	Group 3
1	2620.9 [2249.9 - 3053.1]	Group 2	0.660		
2	2232.6 [1109.1 - 4494.4]	Group 3	<0.001*	<0.001*	
3	20749.6 [14782.0 - 29126.3]	Group 4	<0.001*	<0.001*	0.510
4	17698.23 [12666.8 - 24728.2]				

(D) F4-80+ /GR-1-					
Group	Expected Cell Count [95% CI]		Group 1	Group 2	Group 3
1	498.1 [384.2 - 645.8]	Group 2	0.470		
2	729.6 [270.0 - 1971.9]	Group 3	<0.001*	0.003*	
3	3612.3 [2476.1 - 5269.9]	Group 4	<0.001*	0.004*	0.571
4	3194.2 [2628.6 - 3881.6]				

(E) F4-80- /GR-1+					
Group	Expected Cell Count [95% CI]		Group 1	Group 2	Group 3
1	1710.6 [1294.6 - 2260.4]	Group 2	0.015*		
2	915.4 [602.0 - 1392.1]	Group 3	<0.001*	<0.001*	
3	11055.7 [8421.6 - 14513.6]	Group 4	<0.001*	<0.001*	0.470
4	8539.1 [4461.6 - 16343.3]				

4.2.3 Summary and Discussion

We observed an increase in the number of inflammatory cells 24 hours after intravitreal injection of both PSS-coated and antibody-coated GNRs as compared to sham or no intravitreal injection. Our TEM images demonstrate that free GNRs stay in the vitreous after 24 hours and there is an inflammatory infiltrate. There are several studies suggesting that interactions between gold nanoparticles and inflammatory cells cause recruitment and internalization of particles, and this is in line with what we observed.^{71, 148, 149}

The mechanism by which nanoparticles enter cells has been investigated. Some reports categorize the internalization of nanoparticles as receptor-mediated endocytosis¹⁵⁰ via scavenger receptors.⁷¹ However, the exact mechanism is unclear given the limited techniques available for visualizing nanoparticles intracellularly.⁵¹

While we did not observe a statistically significant difference in inflammation between eyes injected with GNR, either PSS-conjugated or Ab-conjugated, some studies have shown that surface modification can delay uptake of nanoparticles, which may account for the slight differences between those groups.¹⁴⁵ The surface charge of nanoparticles can affect the extent of the inflammatory reaction, with cationic particles being more likely to induce inflammatory responses than anionic.⁵¹ Interestingly, the GNRs used in this experiment have a slightly negative charge. In addition, surface carboxy groups can induce mRNA expression of pro-inflammatory genes. Conversely, amino groups appear to induce expression of anti-inflammatory proteins.¹⁴⁵ In addition, small impurities within particles may make them unstable in physiologic conditions, thereby eliciting an immune response.⁵¹

We have provided evidence that GNRs modified with PSS and conjugated with antibodies can elicit an immune response. PSS has been used as a detergent to detoxify

commercial products and is considered safe for *in-vivo* applications.¹⁵¹ One study, however, found that this is not the case and that PSS caused cytotoxicity *in-vitro*.¹⁵² Future studies investigating different surface coatings, such as polyethylene glycol (PEG) and polyethylene oxide (PEO), are required. Nanoparticles whose surfaces are not modified to prevent adsorption of blood serum proteins (opsonins), which signal cells to ingest the particles, have been reported to be readily removed from the bloodstream by macrophages.¹⁵³ Modifying the surface using a polymer like PEG causes fewer proteins to bind,¹⁵⁴ which may therefore reduce the extent of the immune response.

The aspect ratio of the GNRs in this study was chosen to align with current commercial OCT devices, which have light sources with near-infrared wavelengths. However, it is also necessary to consider the surface characteristics and shape of nanoparticles when optimizing them for *in-vivo* applications. Diameter,¹⁵⁵ shape¹⁵⁶ and aspect ratio¹⁵⁷ appear to affect the extent to which nanoparticles are phagocytosed. In addition, we administered a highly light-scattering dose of GNRs (OD=50), so it may be possible that a lower dose would elicit less of a response and therefore less internalization of particles.

Based on their location within TEM images, the phagocytic cells we observed may be hyalocytes, which reside in the peripheral or cortical region of the vitreous body abutting the inner surface of the retina.¹⁵⁸ These cells belong to the monocyte/macrophage lineage.

Recently, a method for phagocytosis-independent extracellular removal of bacteria, neutrophil extracellular traps,¹⁵⁹ was discovered and shown to occur in the clearance of nanoparticles.¹⁶⁰ Granulocytes, monocytes and macrophages have form networks of traps that are comprised of DNA and protein.¹⁵⁹ The bottom right image within Figure 25 shows a network of fibers in the vitreous, which resemble these extracellular traps. Future studies are necessary to

determine whether the components of these structures match those of the extracellular traps or are collagen fibers in the vitreous.

In summary, our findings suggest that GNRs may elicit an immune response after intravitreal injection of GNRs in the mouse. This inflammatory response may present an obstacle in getting GNRs into the retina for use as contrast or therapeutic agents with optical imaging. Additional studies are required to determine whether GNR design modifications can minimize this inflammatory response.

4.3 SUMMARY AND DISCUSSION: PRE-CLINICAL EXPERIMENTS

In these experiments, we were able to image GNRs *in-vivo* in the eye for the first time and observed that many tend to remain present in the vitreous, altering backscattered intensity within SD-OCT images, after intravitreal administration. A higher frequency of edema associated with GNR injections indicated an inflammatory response might be occurring in parallel with the *in-vivo* administration of GNRs. The presence of an inflammatory infiltrate was confirmed using collagenase digestion of whole eyes, and was present regardless of whether the GNRs were conjugated with antibodies.

5.0 DISSERTATION SYNOPSIS

These experiments established the mouse eye as a practical platform for posterior segment contrast imaging studies with SD-OCT, as we were able to provide a reproducible method for automatically obtaining retinal thickness measurements in healthy mice. After successfully acquiring retinal thickness measurements in a cross-sectional study, we applied this technique to a longitudinal study monitoring a population of mice with experimental glaucoma. In quantifying retinal thickness changes from repetitive scanning, we were able to observe structural changes in a given eye over time. Retinal thickness initially increased rapidly and gradually decreased over the course of three weeks. This gradual thinning out to three weeks is in line with the literature on nerve crush injury, but we were the first to report an initial transient thickening. Our SD-OCT approach is a substantial improvement over conventional histology methods, which require sacrificing several mice at different time points in an attempt to extract a trend using multiple cross-sectional data. Not only does SD-OCT imaging enable true longitudinal analyses, it also substantially reduces the number of animals to be used in experiments.

In parallel to developing a technique for imaging the mouse eye, we also designed a gold nanorod contrast agent that caused an enhancement in intensity of light backscattered from the solution as detected by SD-OCT. We then developed an assay that allowed us to characterize the bioconjugation of GNRs with fluorescently labeled antibodies, tumor cells and flow cytometry, and found that the presence of excess antibodies in Ab-GNR solutions is common. This suggests

that well-established antibody conjugation protocols will need to be adjusted before *in-vivo* applications, as excess antibodies in solution may compete for binding sites with Ab-GNRs.

The results of our *in-vivo* injection experiments suggest that a considerable amount GNRs stay in the vitreous, line the posterior surface of the lens and stick to the hyaloid membrane of the mouse eye for several days following injection. We found that, while their presence increases the backscattered signal intensity in the vitreous – an otherwise clear media – the lingering of these highly reflective GNRs in the vitreous obscures the underlying retinal signal. TEM sections confirmed that GNRs stay in the vitreous and that very few particles enter the retina, with those that are in the retina consistently localized in microglial cells.

TEM, together with our whole-eye collagenase digestion/flow cytometry assay, established that there is a significant inflammatory infiltrate 24 hours after injection of PSS-GNRs and Ab-GNRs, and that there is not a significant difference in the inflammatory response between the two types of particles. The inflammatory cells may be presenting an obstacle, neutrophil extracellular traps, blocking GNRs from getting into the retina. In addition, they may not be able to easily pass through the ILM given their dimensions, surface coatings, or charge.

5.1 LIMITATIONS

While we have shown that GNRs resonant at 840-860 nm can cause backscatter changes detectable by SD-OCT *in-vivo*, there are some limitations associated with our experimental design. One problem we encountered when imaging the mouse eye is that mice develop a reversible cataract, which may be due to dehydration in response to systemic anesthesia and a corresponding decreased body temperature.⁹⁷ While this can be somewhat alleviated by imaging

as close to administration of the anesthetics as possible, it limits the length of imaging sessions to ~20 min. In an attempt to lengthen this window, we tried exposing the mice to different topical drops and heat, but were not able to prevent or delay the onset of cataract. Imaging an awake mouse may offer a solution. In these experiments, however, the time required to align and locate structures of interest, such as the ONH, prevented this.

A limitation to imaging with mice on a movable stage is that the orientation of the mouse changes from scan to scan. We presented a way to manually register images, but a fully automated approach would be preferred, as it would minimize subjectivity and decrease processing time. Detection and alignment techniques based on blood vessel segmentation within OCT fundus images may improve this,¹⁰⁰ but this registration method is not yet optimized for mouse images. In addition, rotating and translating mice means that exact sectoral boundaries are unknown. Thus, when measuring thicknesses, we were limited to only large sectors (quadrants). In order to analyze smaller segments, such as clock hours, it would be necessary to know the exact position of every mouse eye with respect to the stage and SD-OCT system, which was not available in our set up.

In our nerve crush experiment, we observed a consistently higher rate of corneal scarring in eyes that were undergoing the procedure versus control eyes. This resulted in the exclusion of several images due to shadowing from the scar. We hypothesize that was caused by longer recovery time after surgery, or from mechanical damage during the surgical procedure. We tried to alleviate this by applying a topical ointment to eyes after surgery, and by taking care not to damage the cornea during the procedure, but scarring still occurred.

Ideally, in our nerve crush experiments, we would have been able to directly measure RNFL thinning, as the RNFL is directly affected by the surgical injury. However, we were not

able to segment the RNFL since mice have a very thin layer and measurements are unreliable with our current algorithm. Additional A-scan averaging may improve RNFL algorithm performance, or segmentation of retinal regions that are more specific than TRT (eg, from the ILM to the inner plexiform/outer nuclear layer boundary) may be possible.

Very few GNRs entered the retina after intravitreal injection and many were retained in the vitreous, causing an inflammatory reaction and blocking a substantial portion of the signal returning from the retina. Thus, we were not able to isolate RGCs within OCT cross-sections since they cannot reach and pass through the ILM. Other studies suggest that only smaller nanoparticles can enter the retina through the blood retina barrier,¹³⁵ so it is unlikely that GNRs could be directed to RGCs using an intravenous injection. In addition, if Ab-GNRs were able to bind to target cells, we do not know the downstream signaling effects, or consequences of binding with respect to RGC function. Previous studies have shown that anti-Thy-1 binding can cause neurite outgrowth in dorsal root ganglion cells *in-vitro*,¹⁶¹ but the effect on RGCs *in-vivo* is unclear.

We observed that GNRs elicit an inflammatory response after being introduced into the vitreous, which currently limits their use *in-vivo*. It is possible that a manufacturing detail, such as endotoxins evading detection in our sterility monitoring technique, the use of PSS, trace amounts of CTAB, or the charge of the particles is causing this response. Future work is necessary to reveal the cause of inflammation.

While the scattering response attributed to GNRs observed in our SD-OCT systems was easy to discern compared to a low-scattering media, it may be difficult to isolate scattering nanoparticles within scattering tissue. However, since it is possible to access the spectral content of a backscattered interferometric OCT signal using SD-OCT detection, the depth-resolved

spectral characteristics of tissue components can be extracted in a technique referred to as spectroscopic OCT.² GNR spectral signatures have been resolved using this technique.¹⁶² The potential utility of GNRs in spectroscopic OCT is described in the next section.

5.2 FUTURE WORK

While we developed a reproducible method for imaging mice, effort is required to determine how to image mice without damaging the cornea. In order to focus on the mouse retina, it is necessary to compensate for the steep curvature of the mouse cornea. This can be done using a flat coverslip or a contact lens with a flat surface. Initially, we used a coverslip and hypothesized that uneven pressure distribution was causing corneal defects. However, when we tried a custom-made mouse contact lens in an attempt to distribute pressure evenly across the cornea, we still observed corneal scarring. Modifying the lenses used in the SD-OCT system sample path may eliminate this problem.

Our nerve crush experiment provided a model for measuring thickness changes after injury, but may also be a model for an inflammatory reaction causing neuronal degeneration. Future investigation is required to characterize what is causing the early edema and whether this is causing neuronal degeneration. If an inflammatory infiltrate is the source, it may be possible to use anti-inflammatory agents early in the process to prevent or reduce cellular damage after nerve crush injury, thus providing a novel platform for testing pharmaceutical agents and interventions. We also observed that the contralateral eye of nerve-crushed mice appeared to be affected by the procedure (data not shown). If this is the case, experiments where the

contralateral eye is used as a control need to be reconsidered. Further studies are required to assess the extent of damage to the contralateral eye.

We observed that GNRs did not readily enter the retina and that an inflammatory infiltrate is present after the introduction of GNRs into the eye. Surface modification of GNRs, with biocompatible polymers such as PEG, may improve biocompatibility and distribution in the eye, allowing for diffusion into the retina. It may be possible to use proportionally smaller gold nanorods, with the same aspect ratio – and therefore SPR wavelengths – to cause a considerable change in scattering while simultaneously allowing for better diffusion into tissue given the smaller size. Currently, however, the transverse dimension of the GNRs is governed by the seed particle size, which is fixed in the current wet chemical synthesis protocols.

GNRs were highly scattering with respect to the vitreous body in SD-OCT images. However, although GNRs can be designed to have high backscattering cross-sections, many tissue structures, such as the RNFL, are inherently highly scattering. A large dose of nanoparticles may therefore be required to present enough contrast for distinguishing between structures of interest. Detecting changes in OCT signal based on absorption of light,¹⁶³ as opposed to backscattering, or assessing spectroscopic characteristics attributed to GNRs¹⁶² may offer an alternative. Since gold nanorods have a well-established signature spectral response and will be present at different depths in tissues, it follows that it should also be possible to detect the presence of nanorods at different depths by assessing the spectral content of backscattered interferometric signals using spectroscopic OCT.

One promising application of GNRs is in photoacoustic tomography (PAT) imaging.¹²⁷ In PAT, images are formed by detecting ultrasonic waves that have been generated by irradiation with an optical source. PAT is highly sensitive to absorption, and Ab-GNRs have been used for

absorption-based targeted contrast enhancement in PAT.¹⁶⁴ While PAT has only recently been applied to ophthalmology,^{165, 166} it is an emerging technique that may eventually be relevant to the diagnosis of ophthalmic diseases.

5.3 CONCLUSIONS

This dissertation developed the fundamental materials and provided the preliminary imaging data necessary to determine the utility of a targeted contrast agent for ophthalmic OCT imaging. We observed an increase in SD-OCT signal intensity in the vitreous after injection of GNRs, but very few GNRs were able to diffuse into the retina and an inflammatory response ensued. Our results indicate that the utility of GNR contrast agents administered intravitreally is limited.

APPENDIX A

NANOROD DESIGN OPTIMIZATION

The protocol presented by El-Sayed et al results in gold nanorods with a longitudinal resonance wavelength in the 700-750 nm range. Thus, to grow nanorods resonant in the 800-900 nm range, which corresponds to the wavelengths used in our OCT system, the following modifications were applied (Figure 27).

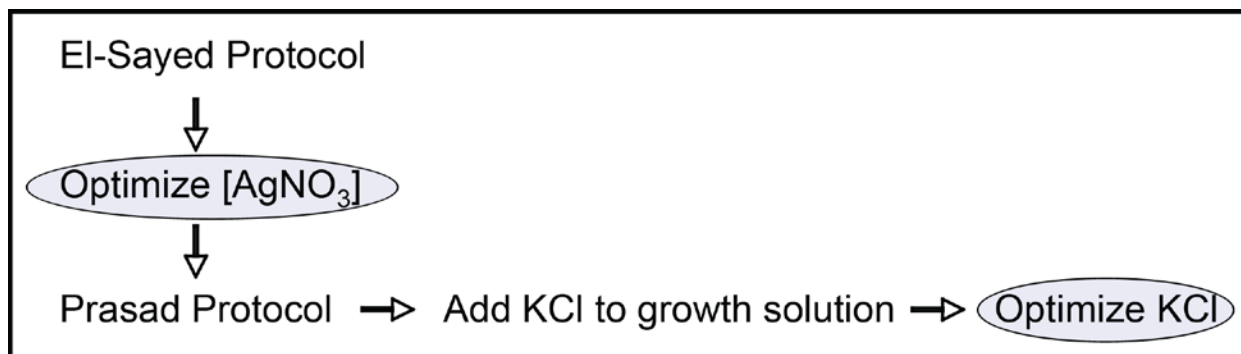


Figure 27. Summary of steps taken to optimize GNR longitudinal resonant wavelength. A protocol by Nikoobakht and El-Sayed¹²² was modified by altering the $[\text{AgNO}_3]$ in the growth solution and adding acid according to the protocol by Prasad.¹⁶⁷

First, we optimized the $[\text{AgNO}_3]$ added to the growth solution. However, this modification allowed for growth of GNRs with a longitudinal resonance wavelength that was less than 800 nm (Figure 28).

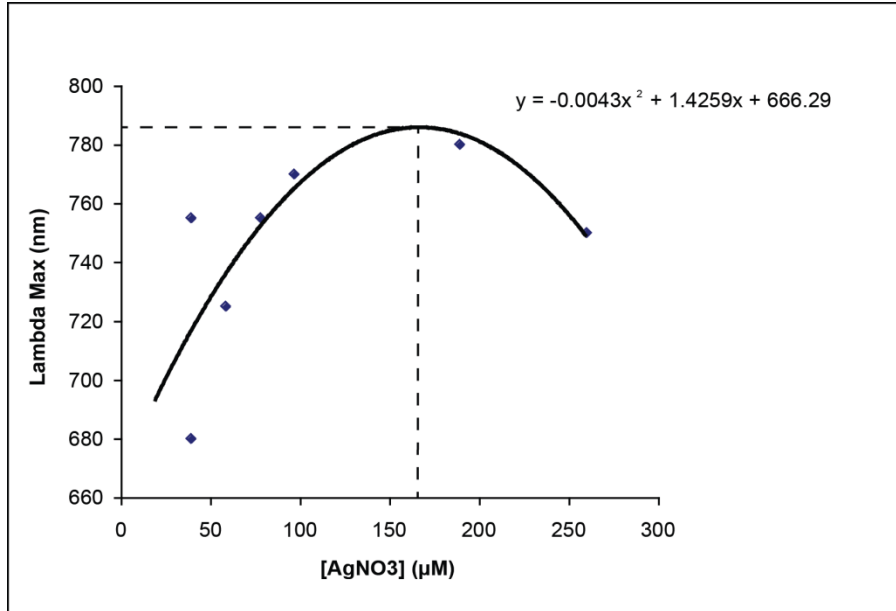


Figure 28. Changing the molar concentration of AgNO₃ that was added to the growth solution only allowed for a maximum longitudinal resonance wavelength of ~785 nm.

Next, we added acid to the growth solution and allowed the solution to sit for 45 min at room temperature (Figure 29). This allowed for the growth of GNRs in the 800-900 nm range, and an example UV-Vis-NIR spectrum from a solution of particles can be seen in Figure 30.

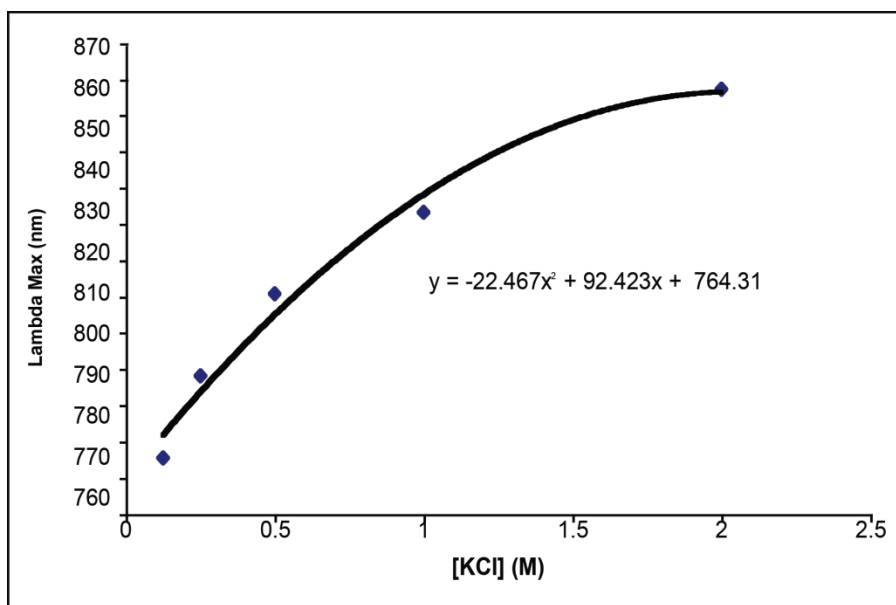


Figure 29. The addition of acid to the growth solution allows for growth of GNRs resonant at ~850 nm

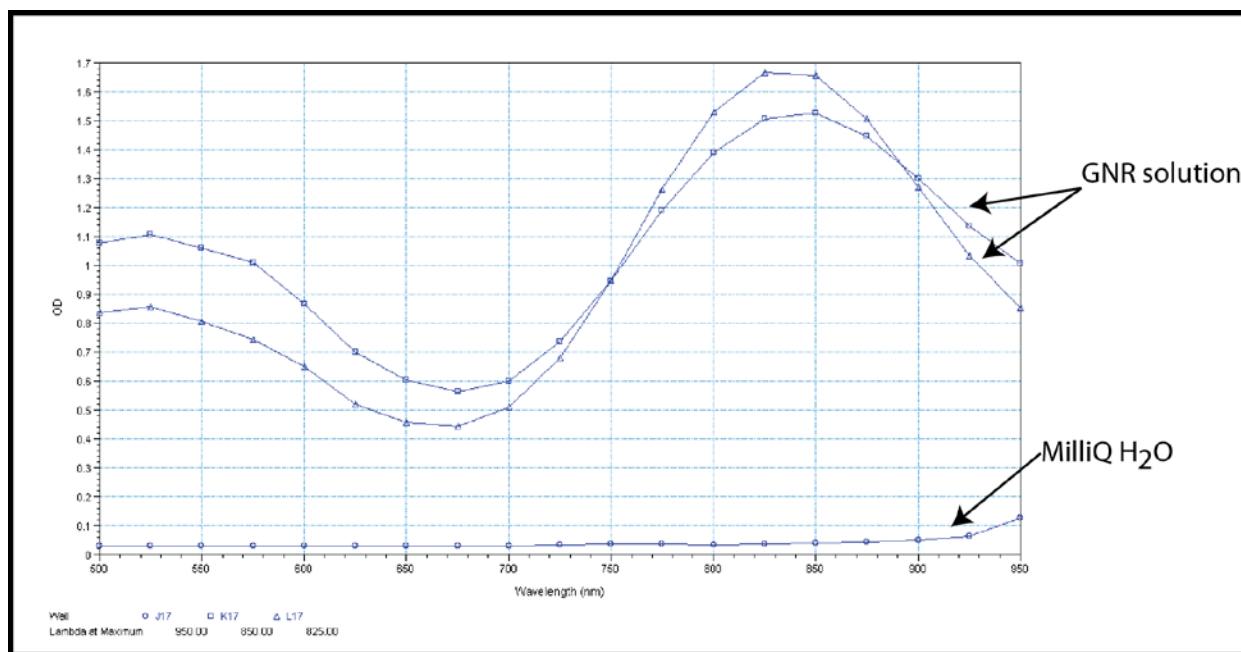


Figure 30. UV-VIS-NIR spectrum of GNRs with longitudinal resonant wavelengths 820-850 nm, with ultrapurified MilliQ water shown for reference. OD – optical density.

Our final protocol, listed in Section 3.1.1, took into account these optimization steps, with the exception that HCl was used in place of KCl to lower the pH of the solution.

APPENDIX B

FIRST AUTHOR PEER-REVIEWED PUBLICATIONS

Gabriele ML, Ishikawa H, Schuman JS, Lin Y, Bilonick RS, Kim JS, Kagemann L, Wollstein G. Optic Nerve Crushed Mice Followed Longitudinally with Spectral Domain Optical Coherence Tomography. *Investigative Ophthalmology and Visual Science*. *Accepted for publication*.

Gabriele ML, Wollstein G, Ishikawa H, Kagemann L, Xu J, Folio L, Schuman JS. History, current status and laboratory work for OCT. (Review) *Investigative Ophthalmology and Visual Science*. *Accepted for publication*.

Gabriele ML, Ishikawa H, Schuman JS, Bilonick RA, Kim JS, Kagemann L, Wollstein G. Reproducibility of Spectral-Domain Optical Coherence Tomography Total Retinal Thickness Measurements in Mice. *Investigative Ophthalmology and Visual Science*. 2010 Jun 23. [Epub ahead of print]

Gabriele ML, Wollstein G, Ishikawa H, Xu J, Kim J, Kagemann L, Folio LS, Schuman JS. Three dimensional optical coherence tomography imaging: Advantages and advances. (Review) *Progress in Retinal and Eye Res*. 2010 Jun 11. [Epub ahead of print]

Gabriele ML, Ishikawa H, Wollstein G, Bilonick RA, Townsend KA, Kagemann LE, Wojtkowski M, Srinivasan VJ, Fujimoto JG, Duker JS, Schuman JS. Optical Coherence Tomography Scan Circle Location and Mean Retinal Nerve Fiber Layer Measurement Variability. *Investigative Ophthalmology and Visual Science*. 2008; 49(6):2315-21. 16.

Gabriele ML, Wollstein G, Bilonick RA, Burgansky-Eliash Z, Ishikawa H, Kagemann LE, Schuman JS. Comparison of parameters from Heidelberg Retina Tomograph 2 and 3. *Ophthalmology*. 2008;115(4):673-7. 19.

Gabriele ML, Ishikawa H, Wollstein G, Bilonick RA, Kagemann L, Wojtkowski M, Duker JS, Fujimoto JG, Schuman JS. Peripapillary Nerve Fiber Layer Thickness Profile Determined With High Speed, Ultrahigh Resolution Optical Coherence Tomography High-Density Scanning. *Investigative Ophthalmology and Visual Science*. 2007;48(7):3154-60. 21.

Gabriele ML, Ishikawa H, Wollstein G, Ferguson RD, Hammer DX, Paunescu LA, Beaton S.A, Schuman JS. Retinal Nerve Fiber Layer Assessment Using Optical Coherence Tomography (OCT) with Active Optic Nerve Head Tracking. *Investigative Ophthalmology and Visual Science*. 2006; 47(3) 964-67.

BIBLIOGRAPHY

1. Drexler W, Morgner U, Kartner FX, et al. In vivo ultrahigh-resolution optical coherence tomography. *Opt Lett* 1999;24:1221-1223.
2. Leitgeb R, Wojtkowski M, Kowalczyk A, Hitzenberger CK, Sticker M, Fercher AF. Spectral measurement of absorption by spectroscopic frequency-domain optical coherence tomography. *Opt Lett* 2000;25:820-822.
3. Nassif N, Cense B, Park BH, et al. In vivo human retinal imaging by ultrahigh-speed spectral domain optical coherence tomography. *Opt Lett* 2004;29:480-482.
4. Wojtkowski M, Leitgeb R, Kowalczyk A, Bajraszewski T, Fercher AF. In vivo human retinal imaging by Fourier domain optical coherence tomography. *J Biomed Opt* 2002;7:457-463.
5. Budenz DL, Chang RT, Huang X, Knighton RW, Tielsch JM. Reproducibility of retinal nerve fiber thickness measurements using the stratus OCT in normal and glaucomatous eyes. *Invest Ophthalmol Vis Sci* 2005;46:2440-2443.
6. Budenz DL, Fredette MJ, Feuer WJ, Anderson DR. Reproducibility of peripapillary retinal nerve fiber thickness measurements with stratus OCT in glaucomatous eyes. *Ophthalmology* 2008;115:661-666 e664.
7. Paunescu LA, Schuman JS, Price LL, et al. Reproducibility of nerve fiber thickness, macular thickness, and optic nerve head measurements using StratusOCT. *Invest Ophthalmol Vis Sci* 2004;45:1716-1724.
8. Gonzalez-Garcia AO, Vizzeri G, Bowd C, Medeiros FA, Zangwill LM, Weinreb RN. Reproducibility of RTVue retinal nerve fiber layer thickness and optic disc measurements and

agreement with Stratus optical coherence tomography measurements. *Am J Ophthalmol* 2009;147:1067-1074, 1074 e1061.

9. Schuman JS. Spectral domain optical coherence tomography for glaucoma (an AOS thesis). *Trans Am Ophthalmol Soc* 2008;106:426-458.

10. Menke MN, Knecht P, Sturm V, Dabov S, Funk J. Reproducibility of nerve fiber layer thickness measurements using 3D fourier-domain OCT. *Invest Ophthalmol Vis Sci* 2008;49:5386-5391.

11. Kim JS, Ishikawa H, Sung KR, et al. Retinal nerve fibre layer thickness measurement reproducibility improved with spectral domain optical coherence tomography. *Br J Ophthalmol* 2009;93:1057-1063.

12. Bowd C, Weinreb RN, Williams JM, Zangwill LM. The retinal nerve fiber layer thickness in ocular hypertensive, normal, and glaucomatous eyes with optical coherence tomography. *Arch Ophthalmol* 2000;118:22-26.

13. Bowd C, Zangwill LM, Berry CC, et al. Detecting early glaucoma by assessment of retinal nerve fiber layer thickness and visual function. *Invest Ophthalmol Vis Sci* 2001;42:1993-2003.

14. Guedes V, Schuman JS, Hertzmark E, et al. Optical coherence tomography measurement of macular and nerve fiber layer thickness in normal and glaucomatous human eyes. *Ophthalmology* 2003;110:177-189.

15. Schuman JS, Hee MR, Puliafito CA, et al. Quantification of nerve fiber layer thickness in normal and glaucomatous eyes using optical coherence tomography. *Arch Ophthalmol* 1995;113:586-596.

16. Pieroth L, Schuman JS, Hertzmark E, et al. Evaluation of focal defects of the nerve fiber layer using optical coherence tomography. *Ophthalmology* 1999;106:570-579.

17. Zangwill LM, Williams J, Berry CC, Knauer S, Weinreb RN. A comparison of optical coherence tomography and retinal nerve fiber layer photography for detection of nerve fiber layer damage in glaucoma. *Ophthalmology* 2000;107:1309-1315.

18. Grainger RG, Thomsen HS, Morcos SK, Koh D, Roditi G. Grainger & Allison's Diagnostic Radiology: A Textbook of Medical Imaging. In: Adam A, Dixon A, Grainger RG,

Allison DJ (eds), *Intravascular Contrast Media for Radiology, CT and MRI*. Philadelphia: Elsevier Churchill Livingstone; 2008.

19. Aronson JK, ††Editor:†† JKA. Ultrasound contrast agents. *Meyler's Side Effects of Drugs: The International Encyclopedia of Adverse Drug Reactions and Interactions*. Amsterdam: Elsevier; 2006:3543-3546.

20. Link S, El-Sayed MA. Optical properties and ultrafast dynamics of metallic nanocrystals. *Annu Rev Phys Chem* 2003;54:331-366.

21. Oldenburg SJ, Averitt RD, Westcott SL, Halas NJ. Nanoengineering of optical resonances. *Chem Phys Lett* 1998;288:243-247.

22. El-Sayed IH, Huang X, El-Sayed MA. Surface plasmon resonance scattering and absorption of anti-EGFR antibody conjugated gold nanoparticles in cancer diagnostics: applications in oral cancer. *Nano Lett* 2005;5:829-834.

23. Sokolov K, Follen M, Aaron J, et al. Real-time vital optical imaging of precancer using anti-epidermal growth factor receptor antibodies conjugated to gold nanoparticles. *Cancer Res* 2003;63:1999-2004.

24. Wojtkowski M. High-speed optical coherence tomography: basics and applications. *Appl Opt* 2010;49:D30-61.

25. de Bruin DM, Burnes DL, Loewenstein J, et al. In vivo three-dimensional imaging of neovascular age-related macular degeneration using optical frequency domain imaging at 1050 nm. *Invest Ophthalmol Vis Sci* 2008;49:4545-4552.

26. Huber R, Adler DC, Srinivasan VJ, Fujimoto JG. Fourier domain mode locking at 1050 nm for ultra-high-speed optical coherence tomography of the human retina at 236,000 axial scans per second. *Opt Lett* 2007;32:2049-2051.

27. Povazay B, Hermann B, Unterhuber A, et al. Three-dimensional optical coherence tomography at 1050 nm versus 800 nm in retinal pathologies: enhanced performance and choroidal penetration in cataract patients. *J Biomed Opt* 2007;12:041211.

28. Puvanathan P, Forbes P, Ren Z, Malchow D, Boyd S, Bizheva K. High-speed, high-resolution Fourier-domain optical coherence tomography system for retinal imaging in the 1060 nm wavelength region. *Opt Lett* 2008;33:2479-2481.

29. Srinivasan VJ, Adler DC, Chen Y, et al. Ultrahigh-speed optical coherence tomography for three-dimensional and en face imaging of the retina and optic nerve head. *Invest Ophthalmol Vis Sci* 2008;49:5103-5110.
30. Lim H, Jiang Y, Wang Y, Huang YC, Chen Z, Wise FW. Ultrahigh-resolution optical coherence tomography with a fiber laser source at 1 microm. *Opt Lett* 2005;30:1171-1173.
31. Unterhuber A, Povazay B, Bizheva K, et al. Advances in broad bandwidth light sources for ultrahigh resolution optical coherence tomography. *Phys Med Biol* 2004;49:1235-1246.
32. Choma MA, Hsu K, Izatt JA. Swept source optical coherence tomography using an all-fiber 1300-nm ring laser source. *J Biomed Opt* 2005;10:44009.
33. de Boer JF, Cense B, Park BH, Pierce MC, Tearney GJ, Bouma BE. Improved signal-to-noise ratio in spectral-domain compared with time-domain optical coherence tomography. *Opt Lett* 2003;28:2067-2069.
34. Wojtkowski M, Srinivasan V, Fujimoto JG, et al. Three-dimensional retinal imaging with high-speed ultrahigh-resolution optical coherence tomography. *Ophthalmology* 2005;112:1734-1746.
35. Zhang J, Rao B, Chen Z. Swept source based fourier domain functional optical coherence tomography. *Conf Proc IEEE Eng Med Biol Soc* 2005;7:7230-7233.
36. Potsaid B, Gorczynska I, Srinivasan VJ, et al. Ultrahigh speed spectral / Fourier domain OCT ophthalmic imaging at 70,000 to 312,500 axial scans per second. *Opt Express* 2008;16:15149-15169.
37. Friedman DS, Wolfs RC, O'Colmain BJ, et al. Prevalence of open-angle glaucoma among adults in the United States. *Arch Ophthalmol* 2004;122:532-538.
38. Quigley HA, Broman AT. The number of people with glaucoma worldwide in 2010 and 2020. *Br J Ophthalmol* 2006;90:262-267.
39. Harwerth RS, Carter-Dawson L, Shen F, Smith EL, 3rd, Crawford ML. Ganglion cell losses underlying visual field defects from experimental glaucoma. *Invest Ophthalmol Vis Sci* 1999;40:2242-2250.

40. Harwerth RS, Carter-Dawson L, Smith EL, 3rd, Barnes G, Holt WF, Crawford ML. Neural losses correlated with visual losses in clinical perimetry. *Invest Ophthalmol Vis Sci* 2004;45:3152-3160.
41. Kerrigan-Baumrind LA, Quigley HA, Pease ME, Kerrigan DF, Mitchell RS. Number of ganglion cells in glaucoma eyes compared with threshold visual field tests in the same persons. *Invest Ophthalmol Vis Sci* 2000;41:741-748.
42. Hoh ST, Greenfield DS, Mistlberger A, Liebmann JM, Ishikawa H, Ritch R. Optical coherence tomography and scanning laser polarimetry in normal, ocular hypertensive, and glaucomatous eyes. *Am J Ophthalmol* 2000;129:129-135.
43. Mistlberger A, Liebmann JM, Greenfield DS, et al. Heidelberg retina tomography and optical coherence tomography in normal, ocular-hypertensive, and glaucomatous eyes. *Ophthalmology* 1999;106:2027-2032.
44. Wollstein G, Ishikawa H, Wang J, Beaton SA, Schuman JS. Comparison of three optical coherence tomography scanning areas for detection of glaucomatous damage. *Am J Ophthalmol* 2005;139:39-43.
45. Gabriele ML, Ishikawa H, Wollstein G, et al. Peripapillary nerve fiber layer thickness profile determined with high speed, ultrahigh resolution optical coherence tomography high-density scanning. *Invest Ophthalmol Vis Sci* 2007;48:3154-3160.
46. Keiper A. The Nanotechnology Revolution. *The New Atlantis* 2003;2:17-34.
47. Couvreur P. Polyalkylcyanoacrylates as colloidal drug carriers. *Crit Rev Ther Drug Carrier Syst* 1988;5:1-20.
48. Pouliquen D, Perdrisot R, Ermias A, Akoka S, Jallet P, Le Jeune JJ. Superparamagnetic iron oxide nanoparticles as a liver MRI contrast agent: contribution of microencapsulation to improved biodistribution. *Magn Reson Imaging* 1989;7:619-627.
49. Clark HA, Kopelman R, Tjalkens R, Philbert MA. Optical nanosensors for chemical analysis inside single living cells. 2. Sensors for pH and calcium and the intracellular application of PEBBLE sensors. *Anal Chem* 1999;71:4837-4843.
50. Loo C, Lin A, Hirsch L, et al. Nanoshell-enabled photonics-based imaging and therapy of cancer. *Technol Cancer Res Treat* 2004;3:33-40.

51. Dobrovolskaia MA, McNeil SE. Immunological properties of engineered nanomaterials. *Nat Nanotechnol* 2007;2:469-478.
52. Aillon KL, Xie Y, El-Gendy N, Berkland CJ, Forrest ML. Effects of nanomaterial physicochemical properties on in vivo toxicity. *Adv Drug Deliv Rev* 2009;61:457-466.
53. Fraser TN. Gold Treatment in Rheumatoid Arthritis. *Ann Rheum Dis* 1945;4:71-75.
54. Kean TA. Rheumatoid Arthritis and Gold Salts Therapy. *Ulster Med J* 1934;3:284-289.
55. Vernon-Roberts B. Action of gold salts on the inflammatory response and inflammatory cell function. *J Rheumatol Suppl* 1979;5:120-129.
56. Lee TM, Oldenburg AL, Sitafalwalla S, et al. Engineered microsphere contrast agents for optical coherence tomography. *Opt Lett* 2003;28:1546-1548.
57. Cang H, Sun T, Li ZY, et al. Gold nanocages as contrast agents for spectroscopic optical coherence tomography. *Opt Lett* 2005;30:3048-3050.
58. Lin AW, Lewinski NA, West JL, Halas NJ, Drezek RA. Optically tunable nanoparticle contrast agents for early cancer detection: model-based analysis of gold nanoshells. *J Biomed Opt* 2005;10:064035.
59. Agrawal A, Huang S, Wei Haw Lin A, et al. Quantitative evaluation of optical coherence tomography signal enhancement with gold nanoshells. *J Biomed Opt* 2006;11:041121.
60. Lee KS, El-Sayed MA. Gold and silver nanoparticles in sensing and imaging: sensitivity of plasmon response to size, shape, and metal composition. *J Phys Chem B* 2006;110:19220-19225.
61. Troutman TS, Barton JK, Romanowski M. Optical coherence tomography with plasmon resonant nanorods of gold. *Opt Lett* 2007;32:1438-1440.
62. Oldenburg AL, Hansen MN, Zweifel DA, Wei A, Boppart SA. Plasmon-resonant gold nanorods as low backscattering albedo contrast agents for optical coherence tomography. *Opt Express* 2006;14:6724-6738.

63. Gobin AM, Lee MH, Halas NJ, James WD, Drezek RA, West JL. Near-infrared resonant nanoshells for combined optical imaging and photothermal cancer therapy. *Nano Lett* 2007;7:1929-1934.
64. Kim CS, Wilder-Smith P, Ahn YC, Liaw LH, Chen Z, Kwon YJ. Enhanced detection of early-stage oral cancer in vivo by optical coherence tomography using multimodal delivery of gold nanoparticles. *J Biomed Opt* 2009;14:034008.
65. Kirillin M, Shirmanova M, Sirotkina M, Bugrova M, Khlebtsov B, Zagaynova E. Contrasting properties of gold nanoshells and titanium dioxide nanoparticles for optical coherence tomography imaging of skin: Monte Carlo simulations and in vivo study. *J Biomed Opt* 2009;14:021017.
66. Huang X, El-Sayed IH, El-Sayed MA. Applications of gold nanorods for cancer imaging and photothermal therapy. *Methods Mol Biol* 2010;624:343-357.
67. Boppart SA, Oldenburg AL, Xu C, Marks DL. Optical probes and techniques for molecular contrast enhancement in coherence imaging. *J Biomed Opt* 2005;10:41208.
68. Yang C, McGuckin LE, Simon JD, Choma MA, Applegate BE, Izatt JA. Spectral triangulation molecular contrast optical coherence tomography with indocyanine green as the contrast agent. *Opt Lett* 2004;29:2016-2018.
69. Oldenburg AL, Gunther JR, Boppart SA. Imaging magnetically labeled cells with magnetomotive optical coherence tomography. *Opt Lett* 2005;30:747-749.
70. Oldenburg A, Toublan F, Suslick K, Wei A, Boppart S. Magnetomotive contrast for in vivo optical coherence tomography. *Opt Express* 2005;13:6597-6614.
71. Shukla R, Bansal V, Chaudhary M, Basu A, Bhonde RR, Sastry M. Biocompatibility of gold nanoparticles and their endocytotic fate inside the cellular compartment: a microscopic overview. *Langmuir* 2005;21:10644-10654.
72. Zhou X, Xie J, Shen M, et al. Biometric measurement of the mouse eye using optical coherence tomography with focal plane advancement. *Vision Res* 2008;48:1137-1143.
73. Zhou X, Shen M, Xie J, et al. The development of the refractive status and ocular growth in C57BL/6 mice. *Invest Ophthalmol Vis Sci* 2008;49:5208-5214.

74. Zhou X, Huang Q, An J, et al. Genetic Deletion of the Adenosine A2A Receptor Confers Postnatal Development of Relative Myopia in Mice. *Invest Ophthalmol Vis Sci* 2010.
75. Horio N, Kachi S, Hori K, et al. Progressive change of optical coherence tomography scans in retinal degeneration slow mice. *Arch Ophthalmol* 2001;119:1329-1332.
76. Li Q, Timmers AM, Hunter K, et al. Noninvasive imaging by optical coherence tomography to monitor retinal degeneration in the mouse. *Invest Ophthalmol Vis Sci* 2001;42:2981-2989.
77. Srinivasan VJ, Ko TH, Wojtkowski M, et al. Noninvasive volumetric imaging and morphometry of the rodent retina with high-speed, ultrahigh-resolution optical coherence tomography. *Invest Ophthalmol Vis Sci* 2006;47:5522-5528.
78. Kocaoglu OP, Uhlhorn SR, Hernandez E, et al. Simultaneous fundus imaging and optical coherence tomography of the mouse retina. *Invest Ophthalmol Vis Sci* 2007;48:1283-1289.
79. Kim KH, Puoris'haag M, Maguluri GN, et al. Monitoring mouse retinal degeneration with high-resolution spectral-domain optical coherence tomography. *J Vis* 2008;8:17 11-11.
80. Fingler J, Readhead C, Schwartz DM, Fraser SE. Phase-contrast OCT imaging of transverse flows in the mouse retina and choroid. *Invest Ophthalmol Vis Sci* 2008;49:5055-5059.
81. Huber G, Beck SC, Grimm C, et al. Spectral domain optical coherence tomography in mouse models of retinal degeneration. *Invest Ophthalmol Vis Sci* 2009;50:5888-5895.
82. Xu J, Molday LL, Molday RS, Sarunic MV. In vivo imaging of the mouse model of X-linked juvenile retinoschisis with fourier domain optical coherence tomography. *Invest Ophthalmol Vis Sci* 2009;50:2989-2993.
83. Maeda A, Golczak M, Maeda T, Palczewski K. Limited roles of Rdh8, Rdh12, and Abca4 in all-trans-retinal clearance in mouse retina. *Invest Ophthalmol Vis Sci* 2009;50:5435-5443.
84. Fischer MD, Huber G, Beck SC, et al. Noninvasive, in vivo assessment of mouse retinal structure using optical coherence tomography. *PLoS One* 2009;4:e7507.

85. Baumann M, Gentile RC, Liebmann JM, Ritch R. Reproducibility of retinal thickness measurements in normal eyes using optical coherence tomography. *Ophthalmic Surg Lasers* 1998;29:280-285.
86. Blumenthal EZ, Williams JM, Weinreb RN, Girkin CA, Berry CC, Zangwill LM. Reproducibility of nerve fiber layer thickness measurements by use of optical coherence tomography. *Ophthalmology* 2000;107:2278-2282.
87. Massin P, Vicaud E, Haouchine B, Erginay A, Paques M, Gaudric A. Reproducibility of retinal mapping using optical coherence tomography. *Arch Ophthalmol* 2001;119:1135-1142.
88. Gurses-Ozden R, Teng C, Vessani R, Zafar S, Liebmann JM, Ritch R. Macular and retinal nerve fiber layer thickness measurement reproducibility using optical coherence tomography (OCT-3). *J Glaucoma* 2004;13:238-244.
89. Kiernan DF, Hariprasad SM, Chin EK, Kiernan CL, Rago J, Mieler WF. Prospective comparison of cirrus and stratus optical coherence tomography for quantifying retinal thickness. *Am J Ophthalmol* 2009;147:267-275 e262.
90. Kiernan DF, Mieler WF, Hariprasad SM. Spectral-domain optical coherence tomography: a comparison of modern high-resolution retinal imaging systems. *Am J Ophthalmol* 2010;149:18-31.
91. Wollstein G, Schuman JS, Price LL, et al. Optical coherence tomography longitudinal evaluation of retinal nerve fiber layer thickness in glaucoma. *Arch Ophthalmol* 2005;123:464-470.
92. Leung CK, Cheung CY, Lin D, Pang CP, Lam DS, Weinreb RN. Longitudinal variability of optic disc and retinal nerve fiber layer measurements. *Invest Ophthalmol Vis Sci* 2008;49:4886-4892.
93. Lalezary M, Medeiros FA, Weinreb RN, et al. Baseline optical coherence tomography predicts the development of glaucomatous change in glaucoma suspects. *Am J Ophthalmol* 2006;142:576-582.
94. Ruggeri M, Wehbe H, Jiao S, et al. In vivo three-dimensional high-resolution imaging of rodent retina with spectral-domain optical coherence tomography. *Invest Ophthalmol Vis Sci* 2007;48:1808-1814.

95. Ruggeri M, Tsechpenakis G, Jiao S, et al. Retinal tumor imaging and volume quantification in mouse model using spectral-domain optical coherence tomography. *Opt Express* 2009;17:4074-4083.
96. Cebulla CM, Ruggeri M, Murray TG, Feuer WJ, Hernandez E. Spectral domain optical coherence tomography in a murine retinal detachment model. *Exp Eye Res* 2010;90:521-527.
97. Calderone L, Grimes P, Shalev M. Acute reversible cataract induced by xylazine and by ketamine-xylazine anesthesia in rats and mice. *Exp Eye Res* 1986;42:331-337.
98. Carpineto P, Ciancaglini M, Zuppari E, Falconio G, Doronzo E, Mastropasqua L. Reliability of nerve fiber layer thickness measurements using optical coherence tomography in normal and glaucomatous eyes. *Ophthalmology* 2003;110:190-195.
99. Kagemann L, Mumcuoglu T, Wollstein G, et al. Sources of longitudinal variability in optical coherence tomography nerve-fibre layer measurements. *Br J Ophthalmol* 2008;92:806-809.
100. Xu J, Ishikawa H, Wollstein G, et al. Automated assessment of the optic nerve head on stereo disc photographs. *Invest Ophthalmol Vis Sci* 2008;49:2512-2517.
101. Allcutt D, Berry M, Sievers J. A quantitative comparison of the reactions of retinal ganglion cells to optic nerve crush in neonatal and adult mice. *Brain Res* 1984;318:219-230.
102. Allcutt D, Berry M, Sievers J. A qualitative comparison of the reactions of retinal ganglion cell axons to optic nerve crush in neonatal and adult mice. *Brain Res* 1984;318:231-240.
103. Castano A, Bell MD, Perry VH. Unusual aspects of inflammation in the nervous system: Wallerian degeneration. *Neurobiol Aging* 1996;17:745-751.
104. Li Y, Schlamp CL, Nickells RW. Experimental induction of retinal ganglion cell death in adult mice. *Invest Ophthalmol Vis Sci* 1999;40:1004-1008.
105. Thanos S, Indorf L, Naskar R. In vivo FM: using conventional fluorescence microscopy to monitor retinal neuronal death in vivo. *Trends Neurosci* 2002;25:441-444.

106. Higashide T, Kawaguchi I, Ohkubo S, Takeda H, Sugiyama K. In vivo imaging and counting of rat retinal ganglion cells using a scanning laser ophthalmoscope. *Invest Ophthalmol Vis Sci* 2006;47:2943-2950.
107. Cordeiro MF, Guo L, Luong V, et al. Real-time imaging of single nerve cell apoptosis in retinal neurodegeneration. *Proc Natl Acad Sci U S A* 2004;101:13352-13356.
108. Leung CK, Lindsey JD, Crowston JG, Lijia C, Chiang S, Weinreb RN. Longitudinal profile of retinal ganglion cell damage after optic nerve crush with blue-light confocal scanning laser ophthalmoscopy. *Invest Ophthalmol Vis Sci* 2008;49:4898-4902.
109. Fischer MD, Tanimoto N, Beck SC, et al. Structural and Functional Phenotyping in the Cone-Specific Photoreceptor Function Loss 1 (cpfl1) Mouse Mutant - A Model of Cone Dystrophies. *Adv Exp Med Biol* 2010;664:593-599.
110. Bai Y, Xu J, Brahimi F, Zhuo Y, Sarunic MV, Saragovi HU. An agonistic anti-TrkB mAb, but not BDNF, causes sustained TrkB activation, delays RGC death, and protects the retinal structure in optic nerve axotomy and in glaucoma. *Invest Ophthalmol Vis Sci* 2010.
111. Gabriele ML, Ishikawa H, Schuman JS, et al. Reproducibility of Spectral-Domain Optical Coherence Tomography Total Retinal Thickness Measurements in Mice. *Invest Ophthalmol Vis Sci* 2010.
112. Stein DM, Ishikawa H, Hariprasad R, et al. A new quality assessment parameter for optical coherence tomography. *Br J Ophthalmol* 2006;90:186-190.
113. Puk O, Dalke C, Favor J, de Angelis MH, Graw J. Variations of eye size parameters among different strains of mice. *Mamm Genome* 2006;17:851-857.
114. Zhou G, Williams RW. Mouse models for the analysis of myopia: an analysis of variation in eye size of adult mice. *Optom Vis Sci* 1999;76:408-418.
115. Schmucker C, Schaeffel F. A paraxial schematic eye model for the growing C57BL/6 mouse. *Vision Res* 2004;44:1857-1867.
116. Stein DM, Wollstein G, Ishikawa H, Hertzmark E, Noecker RJ, Schuman JS. Effect of corneal drying on optical coherence tomography. *Ophthalmology* 2006;113:985-991.

117. van Velthoven ME, van der Linden MH, de Smet MD, Faber DJ, Verbraak FD. Influence of cataract on optical coherence tomography image quality and retinal thickness. *Br J Ophthalmol* 2006;90:1259-1262.
118. Wu Z, Huang J, Dustin L, Sadda SR. Signal strength is an important determinant of accuracy of nerve fiber layer thickness measurement by optical coherence tomography. *J Glaucoma* 2009;18:213-216.
119. Bodeutsch N, Siebert H, Dermon C, Thanos S. Unilateral injury to the adult rat optic nerve causes multiple cellular responses in the contralateral site. *J Neurobiol* 1999;38:116-128.
120. Panagis L, Thanos S, Fischer D, Dermon CR. Unilateral optic nerve crush induces bilateral retinal glial cell proliferation. *Eur J Neurosci* 2005;21:2305-2309.
121. Macharadze T, Goldschmidt J, Marunde M, et al. Interretinal transduction of injury signals after unilateral optic nerve crush. *Neuroreport* 2009;20:301-305.
122. Nikoobakht B, El-Sayed MA. Preparation and growth mechanism of gold nanorods (NRs) using seed-mediated growth method. *Chem Mater* 2003;15:1957-1962.
123. Yu YY, Chang SS, Lee CL, Wang CR. Gold Nanorods: Electrochemical Synthesis and Optical Properties. *J Phys Chem* 1997;101:6661-6664.
124. Esumi K, Matsuhisa K, Torigoe K. Preparation of Rodlike Gold Particles by UV Irradiation Using Cationic Micelles as a Template. *Langmuir* 1995;11:3285-3287.
125. Lee KS, El-Sayed MA. Dependence of the enhanced optical scattering efficiency relative to that of absorption for gold metal nanorods on aspect ratio, size, end-cap shape, and medium refractive index. *J Phys Chem B* 2005;109:20331-20338.
126. Eustis S, El-Sayed MA. Why gold nanoparticles are more precious than pretty gold: noble metal surface plasmon resonance and its enhancement of the radiative and nonradiative properties of nanocrystals of different shapes. *Chem Soc Rev* 2006;35:209-217.
127. Kim K, Agarwal A, Huang SW, et al. Photoacoustic imaging of early inflammatory response using gold nanorods. *Applied Physics Letters* 2007;90:223901.

128. Huang X, El-Sayed IH, Qian W, El-Sayed MA. Cancer cell imaging and photothermal therapy in the near-infrared region by using gold nanorods. *J Am Chem Soc* 2006;128:2115-2120.
129. Wang L, Li YF, Zhou L, et al. Characterization of gold nanorods in vivo by integrated analytical techniques: their uptake, retention, and chemical forms. *Anal Bioanal Chem* 2010;396:1105-1114.
130. Lowery AR, Gobin AM, Day ES, Halas NJ, West JL. ImmunonanosHELLS for targeted photothermal ablation of tumor cells. *Int J Nanomedicine* 2006;1:149-154.
131. Faulk WP, Taylor GM. An immunocolloid method for the electron microscope. *Immunochemistry* 1971;8:1081-1083.
132. Olivier JC, Huertas R, Lee HJ, Calon F, Pardridge WM. Synthesis of pegylated immunonanoparticles. *Pharm Res* 2002;19:1137-1143.
133. Zhang J, Wu SM, Gross RL. Effects of beta-adrenergic blockers on glutamate-induced calcium signals in adult mouse retinal ganglion cells. *Brain Res* 2003;959:111-119.
134. Zheng B, Han S, Kelsoe G. T helper cells in murine germinal centers are antigen-specific emigrants that downregulate Thy-1. *J Exp Med* 1996;184:1083-1091.
135. Kim JH, Kim KW, Kim MH, Yu YS. Intravenously administered gold nanoparticles pass through the blood-retinal barrier depending on the particle size, and induce no retinal toxicity. *Nanotechnology* 2009;20:505101.
136. Kim JH, Kim C, Lee BJ, Yu YS, Park KH, Kim KW. Absence of intravitreal bevacizumab-induced neuronal toxicity in the retina. *Neurotoxicology* 2008;29:1131-1135.
137. Hayashi A, Naseri A, Pennesi ME, de Juan E, Jr. Subretinal delivery of immunoglobulin G with gold nanoparticles in the rabbit eye. *Jpn J Ophthalmol* 2009;53:249-256.
138. Zagaynova EV, Shirmanova MV, Kirillin MY, et al. Contrasting properties of gold nanoparticles for optical coherence tomography: phantom, in vivo studies and Monte Carlo simulation. *Phys Med Biol* 2008;53:4995-5009.

139. Diebold Y, Calonge M. Applications of nanoparticles in ophthalmology. *Prog Retin Eye Res* 2010.
140. Connor EE, Mwamuka J, Gole A, Murphy CJ, Wyatt MD. Gold nanoparticles are taken up by human cells but do not cause acute cytotoxicity. *Small* 2005;1:325-327.
141. Pernodet N, Fang X, Sun Y, et al. Adverse effects of citrate/gold nanoparticles on human dermal fibroblasts. *Small* 2006;2:766-773.
142. Goodman CM, McCusker CD, Yilmaz T, Rotello VM. Toxicity of gold nanoparticles functionalized with cationic and anionic side chains. *Bioconjug Chem* 2004;15:897-900.
143. Chithrani BD, Chan WC. Elucidating the mechanism of cellular uptake and removal of protein-coated gold nanoparticles of different sizes and shapes. *Nano Lett* 2007;7:1542-1550.
144. Pan Y, Neuss S, Leifert A, et al. Size-dependent cytotoxicity of gold nanoparticles. *Small* 2007;3:1941-1949.
145. Bartneck M, Keul HA, Singh S, et al. Rapid uptake of gold nanorods by primary human blood phagocytes and immunomodulatory effects of surface chemistry. *ACS Nano* 2010;4:3073-3086.
146. Gratton SE, Ropp PA, Pohlhaus PD, et al. The effect of particle design on cellular internalization pathways. *Proc Natl Acad Sci U S A* 2008;105:11613-11618.
147. Cho WS, Cho M, Jeong J, et al. Acute toxicity and pharmacokinetics of 13 nm-sized PEG-coated gold nanoparticles. *Toxicol Appl Pharmacol* 2009;236:16-24.
148. Zhang Q, Hitchins VM, Schrand AM, Hussain SM, Goering PL. Uptake of gold nanoparticles in murine macrophage cells without cytotoxicity or production of pro-inflammatory mediators. *Nanotoxicology* 2010.
149. Krpetic Z, Porta F, Caneva E, Dal Santo V, Scari G. Phagocytosis of biocompatible gold nanoparticles. *Langmuir* 2010;26:14799-14805.
150. Xiang SD, Scholzen A, Minigo G, et al. Pathogen recognition and development of particulate vaccines: does size matter? *Methods* 2006;40:1-9.

151. Shepherd G, Klein-Schwartz W, Burstein AH. Efficacy of the cation exchange resin, sodium polystyrene sulfonate, to decrease iron absorption. *J Toxicol Clin Toxicol* 2000;38:389-394.
152. Leonov AP, Zheng J, Clogston JD, Stern ST, Patri AK, Wei A. Detoxification of gold nanorods by treatment with polystyrenesulfonate. *ACS Nano* 2008;2:2481-2488.
153. Gref R, Minamitake Y, Peracchia MT, Trubetskoy V, Torchilin V, Langer R. Biodegradable long-circulating polymeric nanospheres. *Science* 1994;263:1600-1603.
154. Peracchia MT, Harnisch S, Pinto-Alphandary H, et al. Visualization of in vitro protein-rejecting properties of PEGylated stealth polycyanoacrylate nanoparticles. *Biomaterials* 1999;20:1269-1275.
155. Albanese A, Sykes EA, Chan WC. Rough around the edges: the inflammatory response of microglial cells to spiky nanoparticles. *ACS Nano* 2010;4:2490-2493.
156. Champion JA, Mitragotri S. Role of target geometry in phagocytosis. *Proc Natl Acad Sci U S A* 2006;103:4930-4934.
157. Champion JA, Mitragotri S. Shape induced inhibition of phagocytosis of polymer particles. *Pharm Res* 2009;26:244-249.
158. Qiao H, Hisatomi T, Sonoda KH, et al. The characterisation of hyalocytes: the origin, phenotype, and turnover. *Br J Ophthalmol* 2005;89:513-517.
159. Brinkmann V, Reichard U, Goosmann C, et al. Neutrophil extracellular traps kill bacteria. *Science* 2004;303:1532-1535.
160. Bartneck M, Keul HA, Zwadlo-Klarwasser G, Groll J. Phagocytosis independent extracellular nanoparticle clearance by human immune cells. *Nano Lett* 2010;10:59-63.
161. Yang SH, Chen YJ, Tung PY, et al. Anti-Thy-1 antibody-induced neurite outgrowth in cultured dorsal root ganglionic neurons is mediated by the c-Src-MEK signaling pathway. *J Cell Biochem* 2008;103:67-77.

162. Oldenburg AL, Hansen MN, Ralston TS, Wei A, Boppart SA. Imaging gold nanorods in excised human breast carcinoma by spectroscopic optical coherence tomography. *J Mater Chem* 2009;19:6407-6411.
163. Wei M, Qian J, Zhan Q, Cai F, Gharibi A, He S. Differential absorption optical coherence tomography with strong absorption contrast agents of gold nanorods. *Front Optoelectron China* 2009;2:141-145.
164. Agarawal A, Huang SW, O'Donnell M, et al. Targeted gold nanorod contrast agent for prostate cancer detection by photoacoustic imaging. *J Appl Phys* 2007;201:064701.
165. Jiao S, Jiang M, Hu J, et al. Photoacoustic ophthalmoscopy for in vivo retinal imaging. *Opt Express* 2010;18:3967-3972.
166. Silverman RH, Kong F, Chen YC, et al. High-resolution photoacoustic imaging of ocular tissues. *Ultrasound Med Biol* 2010;36:733-742.
167. Yong K, Sahoo Y, Swihart MT, Schneeberger PM, Prasad PN. Templated Synthesis of Gold Nanorods (NRs): The Effects of Cosurfactants and Electrolytes on the Shape and Optical Properties. *Topics in Catalysis* 2008;47:49-60.